

# The High Temperature Superconductivity in Cuprates: Physics of the Pseudogap Region

Paolo Cea <sup>1</sup>

*Dipartimento di Fisica, Università di Bari, Bari, Italy*

*INFN - Sezione di Bari, Bari, Italy*

## ABSTRACT

We discuss the physics of the high temperature superconductivity in hole doped copper oxide ceramics in the pseudogap region. Starting from an effective reduced Hamiltonian relevant to the dynamics of holes injected into the copper oxide layers proposed in a previous paper, we determine the superconductive condensate wavefunction. We show that the low-lying elementary condensate excitations are analogous to the rotons in superfluid  $^4\text{He}$ . We argue that the rotons-like excitations account for the specific heat anomaly at the critical temperature. We discuss and compare with experimental observations the London penetration length, the Abrikosov vortices, the upper and lower critical magnetic fields, and the critical current density. We give arguments to explain the origin of the Fermi arcs and Fermi pockets. We investigate the nodal gap in the cuprate superconductors and discuss both the doping and temperature dependence of the nodal gap. We suggest that the nodal gap is responsible for the doping dependence of the so-called nodal Fermi velocity detected in angle resolved photoemission spectroscopy studies. We discuss the thermodynamics of the nodal quasielectron liquid and their role in the low temperature specific heat. We propose that the ubiquitous presence of charge density wave in hole doped cuprate superconductors in the pseudogap region originates from instabilities of the nodal quasielectrons driven by the interaction with the planar  $\text{CuO}_2$  lattice. We investigate the doping dependence of the charge density wave gap and the competition between charge order and superconductivity. We discuss the effects of external magnetic fields on the charge density wave gap and elucidate the interplay between charge density wave and Abrikosov vortices. Finally, we examine the physics underlying quantum oscillations in the pseudogap region.

**PACS numbers:** 74.20.-z, 74.72.-h, 74.72.Gh.

**Key words:** *High Temperature Superconductivity, Cuprates, Pseudogap, Nodal Gap, Charge Density Wave, Quantum Oscillations*

---

<sup>1</sup>Electronic address: Paolo.Cea@ba.infn.it

# Contents

<b>1</b>	<b>Introduction</b>	<b>2</b>
<b>2</b>	<b>The High Temperature Superconductivity in Cuprates</b>	<b>4</b>
<b>3</b>	<b>Physics of the Superconductive Condensate</b>	<b>9</b>
3.1	Low-lying excitations of the condensate . . . . .	13
3.2	Condensate in external magnetic fields . . . . .	16
3.3	The roton gas and the specific heat anomaly . . . . .	18
3.4	The London penetration length . . . . .	22
3.5	Vortex structure and critical magnetic fields . . . . .	26
3.6	Temperature dependence of the critical magnetic fields . . . . .	33
3.7	Temperature dependence of the critical current . . . . .	36
<b>4</b>	<b>The Nodal Quasielectron Liquid</b>	<b>40</b>
4.1	The nodal gap . . . . .	43
4.2	Thermodynamics of the nodal quasielectron liquid . . . . .	50
4.3	Low temperature specific heat . . . . .	53
<b>5</b>	<b>Charge Density Wave Instability</b>	<b>59</b>
5.1	Charge-ordering wavenumber vectors . . . . .	63
5.2	Critical temperature and gap . . . . .	67
5.3	Competition between charge density wave and superconductivity . . . . .	74
5.4	Effects of the magnetic field . . . . .	77
5.5	Quantum Oscillations . . . . .	81
<b>6</b>	<b>Summary and Conclusions</b>	<b>89</b>
<b>A</b>	<b>D-Wave BCS Gap and Penetration Depth</b>	<b>92</b>

# 1 Introduction

One of the most exciting development in modern physics has been the discovery of high temperature superconductivity in copper oxides (cuprates) by J. G. Bednorz and K. A. Müller [1]. Indeed, the origin of high temperature superconductivity in cuprates continues to be one of the most debated problem in condensed matter physics<sup>2</sup>. Nevertheless, a large amount of informations about superconductivity in cuprates has been obtained. In fact, the phase diagram of the hole doped cuprates is by now quite well established. In Fig. 1 we illustrate schematically the widely accepted phase diagram for hole doped cuprate superconductors [9, 10, 11]. The crystal structure of the cuprate high temperature superconductors consists of  $CuO_2$  sheets separated by insulating layers. The main driver of superconductivity in the cuprates is the copper-oxide plane and, to a good approximation, Cooper pairs form independently on each layer. It is remarkably that superconductivity in cuprates arises in the two-dimensional  $CuO_2$  planes as a common behavior to all cuprate families.

Parent compounds in these materials are antiferromagnetic Mott insulators. As in semiconductors, the carrier concentration in the cuprate superconductors can be changed by doping, namely by increasing the number of holes in the  $CuO_2$  planes. With hole doping to the system with small values of the doping  $\delta$ , it remains antiferromagnetic but the critical Néel temperature decreases rapidly. Then, for hole doping  $\delta \gtrsim \delta_{min} \simeq 0.05$ , the long range antiferromagnetic order is quickly suppressed and the system comes into the superconducting phase. The superconducting state can be observed as a dome that appears roughly between  $\delta_{min} \lesssim \delta \lesssim \delta_{max} \simeq 0.30$ . The superconductive critical temperature attains a maximum at around  $\delta = \delta_{opt} \simeq 0.16$ . This doping level is referred to as the optimally doped region. The lower doping region is called underdoped region, while the higher doping region is referred to as the overdoped region. The overdoped region (especially highly overdoped region) is close to the Fermi liquid state. Indeed, in the overdoped regime the material has a large Fermi surface in the normal state and a simple BCS d-wave superconducting gap opens below the superconductive critical temperature  $T_c$ . On the other hand, the underdoped region of the phase diagram is rather unconventional and it is characterized by the presence of the so-called pseudogap. The pseudogap was first detected in the temperature dependence of the spin-lattice relaxation and Knight shift in nuclear magnetic resonance and magnetic susceptibility studies (for up-to-date reviews, see Refs. [12, 13, 14, 15, 16, 17]). In fact, a gradual depletion of the density of states at the Fermi energy was observed below a crossover temperature  $T^*$ , revealing the opening of the pseudogap well above the superconductive critical temperature  $T_c$  (see Fig. 1). The existence of the pseudogap phase in the underdoped region of the phase diagram is, in fact, one of the most puzzling feature of the high temperature cuprate superconductors. It turns out that the underdoped cuprates in the pseudogap region  $\delta < \delta^*$  display a host of anomalous properties. Indeed, in the underdoped regime the normal state Fermi surface is no longer complete since only Fermi arcs remain. Moreover, the pseudogap gap increases as the doping gets smaller, while the superconductive critical temperature increases almost linearly with the doping. In addition, along the Fermi arcs there is another gap, the nodal gap [15], which does not change much with doping or, if any, decreases in deeply underdoped samples.

The above qualitative description together with the persistent evidence of several forms of

---

<sup>2</sup>For recent overviews, see Refs. [2, 3, 4, 5, 6, 7, 8].

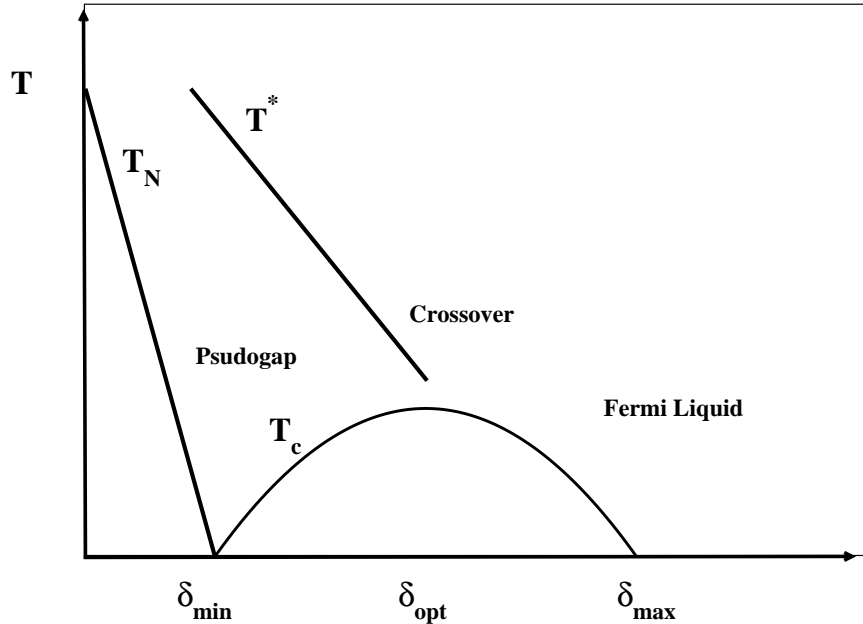


Figure 1: Schematic diagram of the temperature versus hole doping level for the copper oxides, indicating where various phases occur.  $T_N$  is the Néel transition temperature. The region below  $T_N$  is where fully developed antiferromagnetic order set in.  $T^*$  indicates the temperature where the transition to the pseudogap regime occurs.  $T_c$  is the superconducting transition temperature. The dome-shaped superconducting region extends from  $\delta_{min}$  up to  $\delta_{max}$ .

electronic order, including charge density wave which are ubiquitous in this class of superconductors, point to an inextricable complexity of high temperature cuprate superconductors [18]. Nevertheless, soon after the discover of the high temperature superconductors, it was realized [19, 20] that superconductivity were intimately related to the square planar  $CuO_2$  lattice whose physics were well described by the nearly half-filled Hubbard model with moderately on-site Coulomb repulsion. Actually, the microscopic model for the description of electrons in the  $CuO_2$  layers can be assumed to be the effective single-band Hubbard model [19, 20]:

$$\hat{H} = -t \sum_{\langle i,j \rangle, \sigma} \left[ \hat{c}_{i,\sigma}^\dagger \hat{c}_{j,\sigma} + \hat{c}_{j,\sigma}^\dagger \hat{c}_{i,\sigma} \right] + U \sum_i \hat{n}_{i,\uparrow} \hat{n}_{i,\downarrow} \ , \ \hat{n}_{i,\sigma} = \hat{c}_{i,\sigma}^\dagger \hat{c}_{i,\sigma} \ . \quad (1.1)$$

In Eq. (1.1)  $\hat{c}_{i,\sigma}^\dagger$  and  $\hat{c}_{i,\sigma}$  are creation and annihilation operators for electrons with spin  $\sigma$ ,  $U$  is the onsite Coulomb repulsion for electrons of opposite spin at the same atomic orbital, and  $t$  is the hopping parameter. As is well known [21] the superexchange mechanism yields a Heisenberg antiferromagnetic exchange interaction with  $J = \frac{4t^2}{U}$  between spins on the  $Cu$  atoms. Since  $U \gg t$ , at half-filling the onsite Coulomb repulsion gives an insulator where the electron spins are antiferromagnetically ordered. By doping the system an increasing number of holes is created in the  $CuO_2$  planes. The dynamics of the injected holes in the antiferromagnetic background is still poorly understood. Indeed, the interaction responsible for high temperature superconductivity in the cuprates has remained elusive. Therefore, it is desirable to construct the simplest model that is able to capture the basic experimental facts of the physics of the universal properties of the

cuprate superconductors. To this end, to make things as simple as possible and based on plausible physical assumptions, in a previous paper [22], to be referred to hereafter as I, we proposed an effective Hamiltonian to account for the low-lying excitations of the dynamics of holes immersed in an antiferromagnetic background in the  $CuO_2$  planes. In fact, we found that our approach allowed us to reach at least a qualitative understanding of the unusual behavior seen in the various regions of the phase diagram of the cuprate high temperature superconductors.

The aim of the present paper is to better elucidate the physics of the pseudogap region. In fact, as we said, despite intensive studies the origin of the pseudogap, which dominates the underdoped region of the phase diagram, as well as its relation with the superconductivity is still under debate. We will focus here specifically on the occurrence of the pseudogap phase in the phase diagram of the cuprate superconductors and discuss in detail the physics of the cuprates in this region.

The plan of the paper is as follows. In Sect. 2, for reader convenience, we briefly review the phase diagram within our phenomenological microscopic theory. The physics of the superconductive condensate in the pseudogap region is discussed in Sect. 3, where we also discuss the ground state and the condensate wavefunctions. Sect. 3.1 is devoted to the low-lying excitations of the superconductive condensate. In Sect. 3.2 we determine the condensate wavefunction in an external magnetic field. In Sect. 3.3 we discuss the roton gas at finite temperature and the specific heat anomaly at the critical temperature. The penetration length in the London limit is discussed in Sect. 3.4, while the structure of vortices and the critical magnetic fields are presented in Sect. 3.5. Sections 3.6 and 3.7 are dedicated to the comparison of the temperature dependence of the critical magnetic fields and critical current with selected experimental observations. The physics of the nodal quasielectron liquid is introduced in Sect. 4. In Sect. 4.1 we analyze the origin and the temperature dependence of the so-called nodal gap. Sect. 4.2 is reserved to the thermodynamics of the nodal quasielectron liquid. In Sect. 4.3 we critically discuss the specific heat at low temperatures. The charge density wave instabilities are presented in Sect. 5. In Sect. 5.1 we estimate the wavenumber vectors responsible for the instability. In Sect. 5.2 we discuss the charge density wave critical temperature and energy gap. In Sect. 5.3 we analyze the competition between charge density wave instability and superconductivity. The effects of an applied magnetic field on the charge density wave instability and the phenomenology of the charge density wave instabilities in the vortex region are discussed in Sect. 5.4. Sect. 5.5 is devoted to the physics of quantum oscillation. Finally, Sect. 6 provides the summary and the main conclusions of the paper. Some technical details are relegated in Appendix A where we present the calculations of the temperature dependence of the energy gap and London penetration length within the weak coupling d-wave BCS theory.

## 2 The High Temperature Superconductivity in Cuprates

In this Section we briefly illustrate the effective Hamiltonian proposed in I and the resulting phase diagram for hole doped cuprate superconductors. Our approach relies on some gross oversimplifications which, nevertheless, should capture the relevant physics of hole doped cuprates. Firstly, we assumed that the physics of the high temperature cuprates is deeply rooted in the copper-oxide planes. This allowed us to completely neglect the

motion along the direction perpendicular to the  $CuO_2$  planes. Moreover, we assumed that the single-band effective Hubbard model is sufficient to account for all the essential physics of the copper-oxide planes. Within these simplifying approximations, the effective Hamiltonian for the propagation of the holes in the antiferromagnetic background can be written as [23, 24]:

$$\hat{H}_0 = -\frac{t^2}{U} \sum_{\vec{r}} \sum_{i,j} \hat{\psi}_h^\dagger(\vec{r} + \vec{i}a_0 + \vec{j}a_0) \hat{\psi}_h(\vec{r}) , \quad (2.1)$$

where  $\hat{\psi}_h^\dagger(\vec{r})$ ,  $\hat{\psi}_h(\vec{r})$  are creation and annihilation operators for holes at the lattice site  $\vec{r}$ ,  $a_0$  is the copper-oxide planar lattice constant, and the sum over the direction vectors  $\vec{i}$  and  $\vec{j}$  is restricted to next-nearest neighbor lattice sites. Note that in Eq. (2.1) the antiferromagnetic background forces the holes to have antiparallel spins. This ensures that the motion of a hole does not disturb the antiferromagnetic background. With this antiferromagnetic background approximation, it turns out that there is an effective attractive two-body potential between nearest-neighbor holes [23]. More precisely, two holes with distance  $r$ ,  $a_0 \ll r \ll \xi_{AF}$ , where  $\xi_{AF}$  is the antiferromagnetic local order length scale, are subject to an effective attractive two-body potential. In fact, our proposal is quite similar to the spin-bag theory [25] where the pairing is due to a local reduction of the antiferromagnetic order (bag) shared by two holes. This led us to consider the following reduced interaction Hamiltonian:

$$\hat{H}_{int} = \frac{1}{2} \int d\vec{r}_1 d\vec{r}_2 \hat{\psi}_{h,\uparrow}^\dagger(\vec{r}_1) \hat{\psi}_{h,\downarrow}^\dagger(\vec{r}_2) V(\vec{r}_1 - \vec{r}_2) \hat{\psi}_{h,\downarrow}(\vec{r}_2) \hat{\psi}_{h,\uparrow}(\vec{r}_1) , \quad (2.2)$$

where the two-body potential  $V(\vec{r}_1 - \vec{r}_2)$  is given by:

$$V(\vec{r}_1 - \vec{r}_2) = \begin{cases} \infty & \vec{r}_1 = \vec{r}_2 \\ -V_0 & |\vec{r}_1 - \vec{r}_2| \leq r_0(\delta) \\ 0 & otherwise \end{cases} \quad (2.3)$$

The range of the potential  $r_0(\delta)$  is expected to be of the order of the observed size of pairs which turns out to be rather small  $\xi_0 \lesssim 6a_0$ :

$$r_0(\delta) = 6 a_0 \left( 1 - \frac{\delta}{\delta_c} \right)^{\frac{1}{2}} . \quad (2.4)$$

The dependence of  $r_0(\delta)$  on the doping fraction  $\delta$  in Eq. (2.4) takes care of the fact that the area of the antiferromagnetic islands decreases with increasing  $\delta$  since the injected holes tend to destruct the local antiferromagnetic order, which eventually vanishes for  $\delta \gtrsim \delta_c$ . Actually the value  $\delta_c \simeq 0.35$  assures that the superconducting instability disappears at the maximal doping  $\delta_{max} \simeq 0.30$ . Regarding the parameter  $V_0$  in Eq. (2.3), in I we fixed this parameter such that there is at least one real space d-wave bound state:

$$V_0 \simeq 2 J \simeq \frac{8t^2}{U} . \quad (2.5)$$

Since we are interested in the limit of low-lying excitations, we observe that, by writing

$$\hat{\psi}_h(\vec{k}) = \frac{1}{\sqrt{N}} \sum_{\vec{r}} \exp(-i\vec{k} \cdot \vec{r}) \hat{\psi}_h(\vec{r}) . \quad (2.6)$$

where  $\mathcal{N}$  is the number of sites of the copper lattice, we get:

$$\hat{H}_0 = \sum_{\vec{k}} \varepsilon_{\vec{k}} \hat{\psi}_h^\dagger(\vec{k}) \hat{\psi}_h(\vec{k}) , \quad (2.7)$$

where:

$$\varepsilon_{\vec{k}} = - \frac{2t^2}{U} \left[ \cos(2k_x a_0) + \cos(2k_y a_0) \right] \simeq \frac{\hbar^2 \vec{k}^2}{2 m_h^*} , \quad (2.8)$$

and

$$m_h^* = \frac{\hbar^2}{8 \frac{t^2}{U} a_0^2} . \quad (2.9)$$

So that we may write for the effective Hamiltonian:

$$\hat{H}_0 = \sum_{\sigma=\uparrow,\downarrow} \int d\vec{r} \hat{\psi}_{h,\sigma}^\dagger(\vec{r}) \left( \frac{-\hbar^2 \nabla^2}{2 m_h^*} \right) \hat{\psi}_{h,\sigma}(\vec{r}) . \quad (2.10)$$

Therefore, our effective Hamiltonian for low-lying excitations is given by:

$$\hat{H} = \hat{H}_0 + \hat{H}_{int} , \quad (2.11)$$

where  $\hat{H}_0$  and  $\hat{H}_{int}$  are given by Eqs. (2.10) and (2.2) respectively. We will consider a highly idealized crystal with unit cell  $a \simeq b \simeq a_0$ ,  $c \simeq c_0$ , and use the following numerical values for the microscopic parameters:

$$\begin{aligned} a_0 &\simeq 4.0 \cdot 10^{-8} \text{ cm} , \quad c_0 \simeq 13.0 \cdot 10^{-8} \text{ cm} , \\ t &\simeq 0.11 \text{ eV} , \quad \frac{U}{t} \simeq 10 \end{aligned} \quad (2.12)$$

that, indeed, are appropriate for a typical cuprate [26]. Note that, using these numerical values we get:

$$m_h^* \simeq 5.41 m_e , \quad (2.13)$$

where  $m_e$  is the electronic mass, in fair good agreements with several observations in hole doped cuprate superconductors.

It is worthwhile to stress that our previous arguments cannot be considered as a truly microscopic derivation of the effective Hamiltonian. Our approximations were a drastic simplification of the complete many-body Hamiltonian, nevertheless we used it to understand the physics from the simplest point of view without a large number of parameters. Indeed, in I we showed that the effective Hamiltonian offered a consistent picture of the complex phase diagram of high transition temperature cuprate superconductors.

Due to the reduced dimensionality the two-body attractive potential admits real-space d-wave bound states. The binding energy of these bound states  $\Delta_2(\delta)$ , which plays the role of the pseudogap, decreases with increasing doping until it vanishes at a certain critical doping  $\delta^*$ . To a very good approximation, we have [22]:

$$\Delta_2(\delta) \simeq \Delta_2(0) \left[ 1 - \left( \frac{\delta}{\delta^*} \right)^{1.5} \right] , \quad \delta \lesssim \delta^* \simeq 0.207 . \quad (2.14)$$

Using the values of the parameters in Eq. (2.12), we found  $\Delta_2(0) \simeq 41.91 \text{ meV}$ . The pseudogap temperature is simply related to the binding energy:

$$k_B T^*(\delta) = \frac{1}{2} \Delta_2(\delta) . \quad (2.15)$$

In fact, in I we showed that Eq. (2.15) is consistent with observations (see Fig. 8 in Ref. [22]). We see, then, that the actual significance of the pseudogap is the signature of preformed pairs. If the binding energy of each hole pair were so strong that the size of the pair were small compared with the inter-particle spacing, then the ground state would consist of paired holes that, behaving like bosons, would condense into the same state. In this case the ground state wavefunction reduces to the ground state of a Bose-Einstein gas of paired holes [27, 28, 29]. However, although the formation of pairs is essential in forming the superconducting state, its remarkable properties require phase coherence among the pairs. In general, the required phase coherence is established by the condensation of pairs. However, in two spatial dimensions it is well known that there is no truly Bose-Einstein condensation since the Mermin-Wagner-Hohenberg theorem [30, 31] prevents a broken continuous symmetry at finite temperature. Nevertheless, as discussed in I, for  $\delta \gtrsim \delta_{min} \simeq 0.05$  the pairs begin to overlap ensuring that the phases of the pairs are locked to a constant value. The onset of phase coherence gives rise to the superconductivity of the hole pair condensate <sup>3</sup>. Numerous spectroscopic data support the scenario of preformed pairs gaining coherence at low temperatures [33, 34, 35, 36, 37]. However, as is well known [38, 39], the phase coherence of the condensate survives for temperatures not exceeding the Berezinskii-Kosterlitz-Thouless (B-K-T) critical temperature:

$$k_B T_{B-K-T} \simeq \frac{\pi}{2} K_s(T_{B-K-T}) , \quad (2.16)$$

where  $K_s$  is the so-called phase stiffness:

$$K_s \simeq \frac{\hbar^2}{2m_h^*} n_s , \quad (2.17)$$

and the superfluid density is given by:

$$n_s \simeq \frac{\delta}{2a_0^2} . \quad (2.18)$$

For temperatures above  $T_{B-K-T}$  the phase coherence and the superconductivity are lost due to the thermal activation of vortex excitations. If we neglect the temperature dependence of the phase stiffness, we obtain:

$$k_B T_{B-K-T} \simeq \frac{\pi}{8} \frac{\hbar^2}{m_h^*} \frac{\delta}{a_0^2} \simeq \pi \frac{t^2}{U} \delta . \quad (2.19)$$

Using our numerical values for  $t$  and  $U$  in Eq. (2.12) we get:

$$T_{B-K-T} \simeq 401 \text{ K } \delta . \quad (2.20)$$

In Fig. 2, we summarize the phase diagram of the hole doped cuprate superconduc-

---

<sup>3</sup>Interestingly enough, recently the authors of Ref. [32] suggested, in a different context, that the superconductivity in underdoped cuprates can be understood as a superfluid of real-space hole pairs.



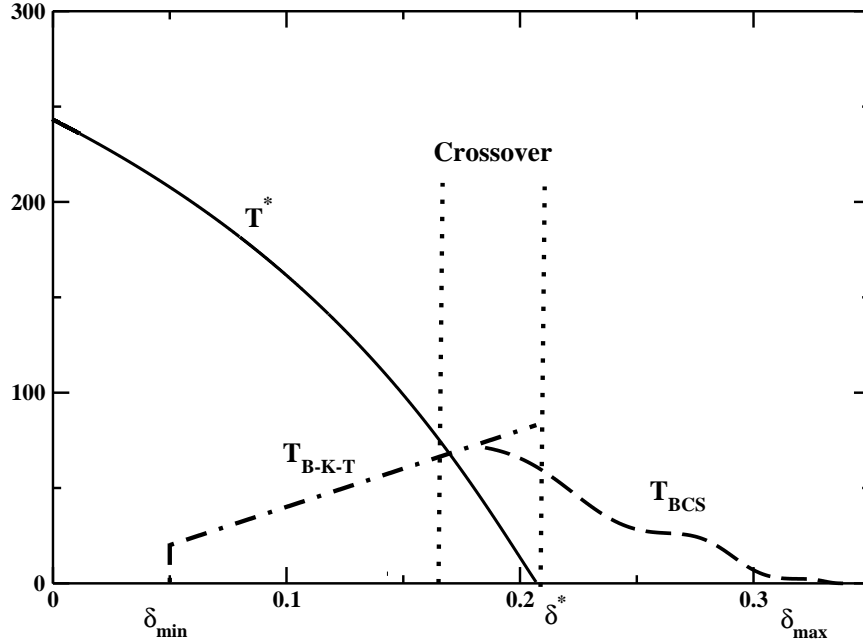


Figure 2: The pseudogap, Berezinskii-Kosterlitz-Thouless, and BCS critical temperatures (in Kelvin) versus the hole doping fraction  $\delta$ . The pseudogap temperature  $T^*$  vanishes at  $\delta = \delta^*$ . The region enclosed by the vertical dotted lines where the three temperatures are comparable corresponds to the crossover region. Note that the crossover region coincides with the optimal doped region.

tors according to our model, we display both the pseudogap and Berezinskii-Kosterlitz-Thouless critical temperatures. Within our approach the pseudogap region is the region where  $T_{B-K-T}$  lies below the pseudogap temperature  $T^*$ . In fact, there is general agreement on the experimental evidence that in the pseudogap region the critical temperature is set by the onset of phase coherence at temperatures lower than the pseudogap temperature [33, 34, 35, 36, 37, 40]. Moreover, there is convincing experimental evidences [41] that the superconducting transition in this region is driven by the order-disorder Berezinskii-Kosterlitz-Thouless (B-K-T) transition [38, 39].

Within our approach the overdoped region is realized for hole doping in excess of the critical doping  $\delta^*$  where the pseudogap vanishes. In this region the conventional superconductivity theory of Bardeen, Cooper, and Schrieffer (BCS) [42, 43, 44] applies since the attractive two-body potential Eq. (2.3) is short-range and can be considered as a small perturbation. In fact, the superconductive instability is driven by the short-range attractive interaction between the quasiparticles and the pairing is in momentum space, so that the relevant superconducting ground state is the BCS variational ground state. For reader convenience, the relevant calculations are presented in Appendix A, and the d-wave BCS critical temperature is displayed in Fig. 2. It turns out that in the overdoped region  $\delta > \delta^*$  the d-wave BCS theory is able to account many of the low-energy and low-temperature properties of the copper oxides, in agreement with several observations, as discussed in I, Sect. 5. Moreover, in this region the normal state is described by an ordinary Fermi liquid metals that is characterized by hole quasiparticles with effective

mass given by Eq. (2.13) and density:

$$n_h \simeq \frac{1 + \delta}{a_0^2} . \quad (2.21)$$

Looking at Fig. 2 we see that in our approach the superconducting dome-shaped region of the hole doped oxide cuprates is determined by the region enclosed by the critical temperatures  $T_{B-K-T}$  and  $T_{BCS}$ . Note that  $T_{B-K-T}$  increases with doping, while the BCS critical temperature decreases with increasing hole doping becoming comparable for  $\delta \sim \delta_{opt} \simeq 0.17$ . We infer, thus, that the superconducting critical temperature reaches its maximum in the optimal doped region where there is a crossover from a Bose-Einstein condensate of tightly bound hole pairs to Cooper pairing of weakly attracting holes <sup>4</sup>. Finally, it is important to point out that in this region the competition between the pseudogap and the d-wave BCS gap together with the enhanced role of the phase fluctuations makes questionable the usually adopted mean-field approximation.

### 3 Physics of the Superconductive Condensate

To reach a reasonable description of the physics of superconductivity in hole doped copper oxide ceramics it is necessary, preliminarily, to construct at least a good approximation of the ground state wavefunction. To do this, it is convenient to adopt the Schrödinger picture. In this representation our reduced Hamiltonian Eq. (2.11) for  $N$  holes in the  $CuO_2$  plane becomes:

$$\hat{H} = \hat{H}_0 + \hat{H}_{int} , \quad (3.1)$$

where

$$\hat{H}_0 = \sum_{i=1}^N -\frac{\hbar^2}{2m_h^*} \nabla_{\vec{r}_i}^2 , \quad (3.2)$$

and

$$\hat{H}_{int} = \frac{1}{2} \sum_{i \neq j}^N V(\vec{r}_i - \vec{r}_j) . \quad (3.3)$$

Note that in Eq. (3.3) the potential  $V(\vec{r}_i - \vec{r}_j)$ , given by Eq. (2.3), is different from zero only for holes with antiparallel spins. The ground state wavefunction is the solution of the Schrödinger eigenvalue equation:

$$\hat{H} \Omega(\vec{r}_1, \dots, \vec{r}_N) = E_0 \Omega(\vec{r}_1, \dots, \vec{r}_N) , \quad (3.4)$$

with the smallest eigenvalue  $E_0$ . In the pseudogap region we said the two isolated holes in interaction with the attractive potential Eq. (2.3) admit a bound state solution. In fact, let consider the Schrödinger equation for two holes (omitting the spin indices):

$$\left[ -\frac{\hbar^2}{2m_h^*} (\nabla_{\vec{r}}^2 + \nabla_{\vec{r}'}^2) + V(\vec{r} - \vec{r}') \right] \Phi(\vec{r}, \vec{r}') = \varepsilon \Phi(\vec{r}, \vec{r}') . \quad (3.5)$$

Writing:

$$\vec{\rho} = \vec{r} - \vec{r}' \quad , \quad \vec{R} = \frac{\vec{r} + \vec{r}'}{2} , \quad (3.6)$$

---

<sup>4</sup>For a through discussion of the crossover from Bose-Einstein condensation to BCS pairing see Ref. [45].

we obtain:

$$\left[ -\frac{\hbar^2}{2m_h^*} \left( 2 \nabla_{\vec{\rho}}^2 + \frac{1}{2} \nabla_{\vec{R}}^2 \right) + V(\rho) \right] \Phi(\vec{R}, \vec{\rho}) = \varepsilon \Phi(\vec{R}, \vec{\rho}) , \quad (3.7)$$

This allows to write:

$$\Phi(\vec{R}, \vec{\rho}) = \exp(i\vec{K} \cdot \vec{R}) \varphi(\vec{\rho}) \quad (3.8)$$

and

$$\varepsilon = \frac{\hbar^2 \vec{K}^2}{4m_h^*} - \Delta . \quad (3.9)$$

It is, now, easy to find:

$$\left[ -\frac{\hbar^2}{m_h^*} \nabla_{\vec{\rho}}^2 + V(\rho) \right] \varphi(\vec{\rho}) = -\Delta \varphi(\vec{\rho}) . \quad (3.10)$$

As discussed in I, Sect. (3.1), Eq. (3.10) admits a d-wave bound state solution with  $\Delta = \Delta_2(\delta) > 0$ . The hole ground-state wavefunction can be, now, obtained as in the BCS approximation. Group the  $N$  conduction holes into  $M = N/2$  pairs and let each pair be described by a bound-state wave function  $\Phi(\vec{r}, \vec{r}')$ . Then consider the  $N$ -hole wavefunction that is just the antisymmetrized product of  $M$  identical such two-hole wavefunctions:

$$\Omega(\vec{r}_1, \dots, \vec{r}_N) = \frac{1}{\sqrt{N!}} \sum_P (-1)^P P \left\{ \Phi(\vec{r}_1 - \vec{r}_2) \cdots \Phi(\vec{r}_{N-1} - \vec{r}_N) \right\} , \quad (3.11)$$

in which the sum is over all permutations  $P$  of the  $N$  holes. Since we are interested in the ground-state wavefunction in the underdoped region, we may simplify considerably the BCS-like wavefunction Eq. (3.11). In fact, we already known [22] that the spatial range of the pair wave function is  $\xi_0 \simeq 2a_0$  (see I, Fig. 4). So that, in the underdoped region  $\xi_0$  is smaller than the average distance between pairs:

$$d_0 \simeq \frac{1}{\sqrt{n_s}} \simeq \frac{\sqrt{2}a_0}{\sqrt{\delta}} . \quad (3.12)$$

Therefore, in this case wavefunctions in the sum in Eq. (3.11) differing by the exchange of single members of two or more pairs do not overlap very much. This means that we may keep in Eq. (3.11) only terms where there are exchanges of two or more pairs. Thus, to a good approximation we can rewrite the ground state wavefunction as:

$$\Omega(\vec{R}_1, \dots, \vec{R}_M, \vec{\rho}_1, \dots, \vec{\rho}_M) \simeq \frac{1}{\sqrt{M!}} \sum_P P \left\{ e^{i[\theta(\vec{R}_1) + \dots + \theta(\vec{R}_M)]} \varphi(\vec{\rho}_1) \cdots \varphi(\vec{\rho}_M) \right\} , \quad (3.13)$$

where  $\theta(\vec{R}_i) = \vec{K} \cdot \vec{R}_i$ . With these approximations, it is quite easy to check that the wavefunction Eq. (3.13) satisfy the time-independent Schrödinger equation Eq. (3.4) with eigenvalue:

$$E \simeq M \left( \frac{\hbar^2 \vec{K}^2}{4m_h^*} - \Delta_2(\delta) \right) . \quad (3.14)$$

Of course, the ground state wavefunction is obtained when the center of mass of the pairs is at rest,  $\vec{P} = \hbar \vec{K} = 0$ :

$$E_0 = E_c , \quad E_c \simeq -M \Delta_2(\delta) , \quad (3.15)$$

where  $E_c$  is the condensation energy.

For later convenience, let us rewrite Eq. (3.13) in the following form:

$$\Omega(\vec{R}_1, \dots, \vec{R}_M, \vec{\rho}_1, \dots, \vec{\rho}_M) \simeq \frac{1}{\sqrt{M!}} \sum_P P \left\{ \Theta(\vec{R}_1) \cdots \Theta(\vec{R}_M) \varphi(\vec{\rho}_1) \cdots \varphi(\vec{\rho}_M) \right\}. \quad (3.16)$$

If we normalize the wavefunctions as:

$$\int d\vec{R}_i |\Theta(\vec{R}_i)|^2 = 1, \quad (3.17)$$

$$\int d\vec{\rho}_i |\varphi(\vec{\rho}_i)|^2 = 1, \quad (3.18)$$

then, it easy to find:

$$\int \prod_i d\vec{R}_i d\vec{\rho}_i \left| \Omega(\vec{R}_1, \dots, \vec{R}_M, \vec{\rho}_1, \dots, \vec{\rho}_M) \right|^2 = 1. \quad (3.19)$$

It is worthwhile to note that:

$$\Theta(\vec{R}) = \frac{1}{\sqrt{V}} \exp(i\vec{K} \cdot \vec{R}), \quad (3.20)$$

so that for the ground state:

$$\Theta(\vec{R}) = \Theta_0(\vec{R}) = \frac{1}{\sqrt{V}}. \quad (3.21)$$

Following Ref. [46] we introduce the reduced wavefunction  $\Psi(\vec{R}_1, \dots, \vec{R}_M)$  defined by:

$$\begin{aligned} \Psi^*(\vec{R}_1', \dots, \vec{R}_M') \Psi(\vec{R}_1, \dots, \vec{R}_M) = \\ \int \prod_i d\vec{\rho}_i \Omega^*(\vec{R}_1', \dots, \vec{R}_M', \vec{\rho}_1, \dots, \vec{\rho}_M) \Omega(\vec{R}_1, \dots, \vec{R}_M, \vec{\rho}_1, \dots, \vec{\rho}_M). \end{aligned} \quad (3.22)$$

Using Eq. (3.16), a straightforward calculation gives:

$$\Psi(\vec{R}_1, \dots, \vec{R}_M) \simeq \frac{1}{\sqrt{M!}} \sum_P P \left\{ \Theta(\vec{R}_1) \cdots \Theta(\vec{R}_M) \right\}. \quad (3.23)$$

We introduce, now, the single-particle density matrix [46]:

$$\rho(\vec{R}, \vec{R}') = M \int \prod_{i=2}^M d\vec{R}_i \Psi^*(\vec{R}, \vec{R}_2, \dots, \vec{R}_M) \Psi(\vec{R}', \vec{R}_2, \dots, \vec{R}_M). \quad (3.24)$$

The physical meaning of  $\rho(\vec{R}, \vec{R}')$  is that the density matrix gives the probability amplitude to find a particular hole pair at  $\vec{R}$  times the amplitude to find it at  $\vec{R}'$  taking into account the correlations due to the remaining  $M - 1$  hole pairs. The factor  $M$  in the definition of the density matrix is due to the fact that we have  $M$  identical pairs. Equivalently, in terms of the second quantization formalism one may introduce the creation operator of a pair with center of mass coordinate  $\vec{R}$ :

$$\hat{b}^\dagger(\vec{R}) = \int d\vec{\rho} \Phi^*(\vec{R}, \vec{\rho}) \hat{\psi}_{h,\uparrow}^\dagger(\vec{R} - \frac{\vec{\rho}}{2}) \hat{\psi}_{h,\downarrow}^\dagger(\vec{R} + \frac{\vec{\rho}}{2}). \quad (3.25)$$

Then, we have:

$$\rho(\vec{R}, \vec{R}') = \langle \Omega | \hat{b}^\dagger(\vec{R}) \hat{b}(\vec{R}') | \Omega \rangle . \quad (3.26)$$

From Eq. (3.24), after taking into account Eq. (3.23), we get easily:

$$\rho(\vec{R}, \vec{R}') \simeq M \Theta^*(\vec{R}) \Theta(\vec{R}') . \quad (3.27)$$

We may, now, introduce the condensate wavefunction  $\chi(\vec{R})$  which plays the role of the order parameter:

$$\rho(\vec{R}, \vec{R}') \equiv \chi^*(\vec{R}) \chi(\vec{R}') . \quad (3.28)$$

This last equation, combined with previous equations, leads to:

$$\chi(\vec{R}) \simeq \sqrt{M} \Theta(\vec{R}) = \sqrt{\frac{M}{V}} e^{i\theta(\vec{R})} = \sqrt{n_s} e^{i\theta(\vec{R})} , \quad (3.29)$$

where  $n_s$  is given by Eq. (2.18). In particular, the ground-state condensate wavefunction is simply:

$$\chi_0(\vec{R}) \simeq \sqrt{n_s} . \quad (3.30)$$

From our discussion it follows that the low-lying condensate excitations can be obtained by solving the Schrödinger-like eigenvalue equation:

$$- \frac{\hbar^2}{4m_h^*} \nabla_{\vec{R}}^2 \chi(\vec{R}) = \varepsilon \chi(\vec{R}) , \quad (3.31)$$

where  $\varepsilon$  is the energy per particle in excess to the condensation energy. Eq. (3.31) shows that the condensate wavefunction satisfies the Schrödinger equation of a free particle with mass  $2m_h^*$ . In fact, this is due to our approximations which neglect the Coulomb interactions, always present in metal, between hole pairs. Since the hole pairs have charge  $+2e$ , then the pairs must avoid to be too close due to the Coulomb repulsion. As a consequence, in the ground state the pairs fill the system with a density almost uniform over distance  $R \gg d_0$ . If one takes care of the Coulomb interactions, then, in general, one finds that the condensate wavefunction satisfies a non-linear Schrödinger equation, the time-independent Gross-Pitaevskii equation. In that case the energy per particle must be replaced by the chemical potential <sup>5</sup>.

In general, the condensate excitations are characterized by a non-zero planar current density:

$$\vec{j}(\vec{R}) = \frac{-i\hbar}{4m_h^*} \left[ \chi^*(\vec{R}) \nabla \chi(\vec{R}) - \nabla \chi^*(\vec{R}) \chi(\vec{R}) \right] . \quad (3.32)$$

Using Eq. (3.29) we obtain:

$$\begin{aligned} \vec{j}(\vec{R}) &= n_s \frac{\hbar}{2m_h^*} \nabla \theta(\vec{R}) = n_s \vec{v}_s(\vec{R}) , \\ \vec{v}_s(\vec{R}) &= \frac{\hbar}{2m_h^*} \nabla \theta(\vec{R}) . \end{aligned} \quad (3.33)$$

For slow-varying condensate phase  $\theta(\vec{R})$ , i.e.  $|\nabla^2 \theta(\vec{R})| \ll |\nabla \theta(\vec{R})|^2$ , the energy of the condensate excitations can be written as:

$$\varepsilon \simeq \frac{1}{2} 2m_h^* \vec{v}_s^2(\vec{R}) = m_h^* \vec{v}_s^2(\vec{R}) . \quad (3.34)$$

---

<sup>5</sup>A good account can be found, for example, in Ref. [46].

Finally, it is worthwhile to remark once more that the superfluidity of the condensate is assured by phase coherence. We have already remarked that for  $\delta > \delta_{min}$  the exponentially small overlap of the hole pair wavefunctions constrains the pair wavefunctions to have the same phase. Therefore, if a current is established in the condensate, all the hole pairs must move together. Let  $\vec{P} = \hbar \vec{K}$  be the momentum of the center of mass of pairs. It is easy to see that the condensate wavefunction is given by Eq. (3.29) with  $\theta(\vec{R}) = \vec{K} \cdot \vec{R}$ . This corresponds to a condensate with velocity  $\vec{v}_s = \frac{\hbar \vec{K}}{2m_h^*}$  and current density  $\vec{j} = n_s \vec{v}_s$ . One might expect that such a current could be degraded by a single-pair collision in which the center of mass momentum is reduced back to zero. However, all the other pairs are described by identical pair wavefunctions. Thus one cannot change the pair wavefunction individually without destroying the whole condensate, and this cost an enormous amount of energy. We see, therefore, that it is the phase coherence which assures rigidity to the wavefunction implying condensate superfluidity.

### 3.1 Low-lying excitations of the condensate

Our previous discussion summarizes the essential features of the ground state at zero temperature. To describe the thermal or transport properties of the hole pair condensate we need to determine the low-lying excited states. The most obvious possibility is to excite the system by breaking a single pair. This requires an energy  $\varepsilon \simeq \Delta_2$ . This kind of excitations, however, are relevant for temperatures exceeding the pseudogap temperature  $T^*$ . Therefore, in the pseudogap region, where  $T^*$  is greater than the superconductive critical temperature, these excitations cannot contribute to the dynamics of the superfluid condensate. We are led, thus, to inquire if there are excitations with energies  $\varepsilon \lesssim \Delta_2$ . According to our previous discussion, the reduced wavefunctions of these excitations can be written as:

$$\Psi_1(\vec{R}_1, \dots, \vec{R}_M) = e^{i\Theta(\vec{R}_1, \dots, \vec{R}_M)} \Psi_0(\vec{R}_1, \dots, \vec{R}_M), \quad (3.35)$$

where  $\Psi_0(\vec{R}_1, \dots, \vec{R}_M)$  is the ground-state wavefunction, and  $\Theta(\vec{R}_1, \dots, \vec{R}_M)$  is a totally symmetric function of  $\vec{R}_1, \dots, \vec{R}_M$ . To determine the wavefunction  $\Psi_1$  we shall follow quite closely the Feynman's superb discussion on the excited states in liquid  $^4\text{He}$  [47]. The simplest choice for the excited state wavefunction would be:

$$\Psi_1(\vec{R}_1, \dots, \vec{R}_M) = e^{i\vec{K} \cdot \vec{R}_i} \Psi_0(\vec{R}_1, \dots, \vec{R}_M) \quad (3.36)$$

for some fixed  $\vec{R}_i$ . However, since the wavefunction must be symmetric we must write:

$$\Psi_1(\vec{R}_1, \dots, \vec{R}_M) = \sum_{i=1}^M e^{i\vec{K} \cdot \vec{R}_i} \Psi_0(\vec{R}_1, \dots, \vec{R}_M) \quad (3.37)$$

According to the results of the previous Section, the corresponding excitation energy is  $\varepsilon = \frac{\hbar^2}{4m_h^*} \vec{K}^2$ . Then, to have low-energy excitations we are forced to consider very small wavenumber  $|\vec{K}|$ . However, since the wavefunction  $\Psi_1$  must be orthogonal to  $\Psi_0$ , i.e.

$$\int d\vec{R}_1 \dots d\vec{R}_M \Psi_0^*(\vec{R}_1, \dots, \vec{R}_M) \Psi_1(\vec{R}_1, \dots, \vec{R}_M) = 0, \quad (3.38)$$

we need configurations where  $\vec{K} \cdot \vec{R}_i$  is appreciably different from zero. Due to the symmetry for exchanges of pairs, these configurations can be realized only by changing the

density of the condensate. In fact, Feynman argued that in liquid  ${}^4\text{He}$  these configurations are the only available low-energy excitations and they give rise to the phonon spectrum. In fact, these sound-wave modes are present also in traditional BCS superconductors [48, 49]. However, due to the Coulomb interactions the sound-wave mode is pushed up to high energy and becomes the plasma mode. As a result, the putative low-energy excitations are realized by density distributions that oscillate at the plasma frequency  $\omega_{pl}$ . We may estimate the plasma frequency by the well-known expression:

$$\omega_{pl} = \sqrt{\frac{4\pi\rho q^2}{m}}, \quad (3.39)$$

where  $\rho$  is the volumetric density of particles with charge  $q$  and mass  $m$ . Accordingly, taking into account that:

$$m = 2m_h^*, \quad q = 2e, \quad \rho \simeq \frac{n_s}{c_0} \simeq \frac{\delta}{2a_0^2 c_0}, \quad (3.40)$$

we obtain:

$$\omega_{pl} \simeq \sqrt{\frac{4\pi e^2 \delta}{m_h^* a_0^2 c_0}}. \quad (3.41)$$

After taking into account Eq. (2.9) we get:

$$\varepsilon_{pl} \simeq \hbar \omega_{pl} \simeq \sqrt{32\pi \frac{e^2 t^2}{c_0 U}} \delta. \quad (3.42)$$

Using the numerical values of the parameters, Eq. (2.12), we find that in the region of interest  $\varepsilon_{pl} \simeq 1.11 \text{ eV} \sqrt{\delta} \gg \Delta_2$ . Therefore, we are led to conclude that the only low-lying excitations of the pair condensate are analogous the the rotons in  ${}^4\text{He}$ . These kind of excitations are described by the condensate wavefunction  $\chi(\vec{R})$ , Eq. (3.29), where  $\theta(\vec{R})$  is a rapidly varying function over a distance of order  $d_0$ . We may estimate the roton energy by assuming that the phase  $\theta(\vec{R})$  is subject to a variation of  $2\pi$  over distance of  $d_0$ . In fact this allows to localize the condensate disturbance in a region of linear size  $d_0$  around a given  $\vec{R}$ . To see this, we note that  $\theta$  equals 0 or  $2\pi$  for  $\vec{R}'$  such that  $|\vec{R}' - \vec{R}| > d_0$ . So that, since  $e^{i\theta} = 1$ , we have  $\chi(\vec{R}) \simeq \chi_0$  outside the disturbance region. Now, taking into account that:

$$|\nabla \theta_{rot}(\vec{R})| \simeq \frac{2\pi}{d_0}, \quad (3.43)$$

we readily obtain:

$$\varepsilon_{rot} \simeq m_h^* \vec{v}_s^2 \simeq \frac{\hbar^2 \pi^2}{m_h^*} n_s. \quad (3.44)$$

Actually, one could consider rotons corresponding to a phase jump of  $2\pi n$ ,  $n$  integer. However, Eq. (3.44) shows that the energy of these rotons is higher by a factor  $n^2$ . So that, only rotons with  $n = 1$  are of interest. Using the numerical values of the model parameters, we find:

$$\varepsilon_{rot} \simeq 434 \text{ meV } \delta. \quad (3.45)$$

For  $\delta \simeq 0.1$  we have  $\varepsilon_{rot} \simeq 43 \text{ meV} \simeq \Delta_2(0)$ . Therefore, we may conclude that below the critical superconductive temperature the roton-like condensate excitations could play

a role in the dynamics of the system.

We said that the low-lying quasi-particle excitations, described by the condensate wavefunction:

$$\chi_{rot}(\vec{R}) \simeq \sqrt{n_s} e^{i\theta_{rot}(\vec{R})}, \quad (3.46)$$

are analogous to the rotons in liquid  $^4He$ . However, in liquid helium Feynman and Cohen [50, 51] argued that the roton wavefunction could not provide a correct description because it does not offer a proper account of the motion of an excitation through the condensate. In fact the quasiparticle excitations are characterized by a non-zero current given by Eq. (3.33). Such a description cannot be appropriate for stationary excitations since the corresponding current must necessarily vanish. In fact, Feynman and Cohen pointed out that one must take care of the backflow of the condensate as the excitation moves through it. It turns out that the backflow corresponds to a slow drift of the condensate outside the region of the excitation which can be described by a vortex-antivortex distribution of the condensate phase. As a result, the backflow acts to cancel the excitation current and to increase the effective mass of the excitation<sup>6</sup>. Therefore, the roton excitation energy can be written as:

$$\varepsilon_{rot} \simeq \alpha m_h^* \vec{v}_s^2, \quad (3.47)$$

where  $\alpha$  is some constant expected to be greater than 1,  $\alpha > 1$ . Actually, the precise numerical value of this constant is not important for our purposes. Microscopic calculations in liquid  $^4He$  indicated that  $\alpha \sim 1.5$  [52], nevertheless, to be conservative, in the following we shall assume  $\alpha \simeq 1.0$ .

It is worthwhile to stress that these roton-like elementary excitations rely on the phase coherence of the hole pair condensate. According to our model, in the pseudogap region the superconducting transition is described by the Berezinskii-Kosterlitz-Thouless order-disorder transition. It is well known that the Berezinskii-Kosterlitz-Thouless transition is driven by vortex-antivortex unbinding which destroys the phase coherence above the critical temperature,  $T > T_c$ . In other words, for  $T > T_c$  configurations corresponding to an uniform condensate velocity  $v_s$  are unstable to the decay into vortex excitations. Kosterlitz [53] introduced the correlation or screening length:

$$\xi_+(T) = \xi_V e^{\frac{b\pi}{\sqrt{T/T_c-1}}}, \quad T \rightarrow T_c^+, \quad (3.48)$$

where  $\xi_V$  is vortex core linear size and  $b$  is a non-universal constant, such that the number density of free vortices is proportional to  $[\xi_+(T)]^{-2}$  [54, 55]. For temperatures near the critical temperature  $T_c$ , configurations leading to a condensate velocity  $v_s$  are expected to be screened by free vortices. Moreover the screening should depend on the free vortex density. Therefore, we expect that for  $T \rightarrow T_c^+$ :

$$v_s(T) \sim [\xi_+(T)]^{-2} \sim e^{\frac{2\pi b}{\sqrt{T/T_c-1}}}. \quad (3.49)$$

In fact, similar arguments has been adopted to determine the temperature dependence of the conductivity in the resistive transition of superconducting films [56]. On the other hand, we are mainly interested in the temperature dependence of the condensate velocity

---

<sup>6</sup>For a very clear discussion, see Ref. [52].



below the critical temperature,  $T \rightarrow T_c^-$ . To this end, we may employ the Kosterlitz's recursion relation [53]:

$$\xi_+(T) \sim \xi_V \left[ \frac{\xi_-(T)}{\xi_V} \right]^{2\pi}, \quad (3.50)$$

where  $\xi_-(T)$  is the screening length for  $T \rightarrow T_c^-$ . Combining Eqs. (3.48) and (3.50) we get:

$$\xi_-(T) = \xi_V e^{\frac{b}{2\sqrt{1-T/T_c}}}, \quad T \rightarrow T_c^-. \quad (3.51)$$

Therefore, we obtain the remarkable result that superfluid velocities are screened to zero for  $T \rightarrow T_c^-$  according to:

$$v_s(T) \sim \xi_V^{-2} e^{-\frac{b}{\sqrt{1-T/T_c}}}, \quad T \rightarrow T_c^-. \quad (3.52)$$

Eq. (3.52) is valid for temperatures quite close to  $T_c$ . However, due to the exponential dependence on the temperature, we may extrapolate Eq. (3.52) down to very low temperatures according to:

$$v_s(T) \simeq v_s(T=0) e^{-b \left[ \frac{1}{\sqrt{1-T/T_c}} - 1 \right]}, \quad T \leq T_c. \quad (3.53)$$

The previous arguments are valid also for the hole pair condensate fraction  $n_s(T)$  which shares phase coherence. In fact, as discussed in Sect. 3, at  $T = 0$  all the hole pairs are condensed so that  $n_s(T=0) = \frac{\delta}{2a_0^2}$ . However, at finite temperatures the thermal activation of vortex-antivortex pairs tend to disorder the system such that  $n_s(T) < n_s(0)$ . Now, as for  $v_s(T)$  the depletion of the phase-coherent condensate is proportional to the density of vortices. Proceeding as before, we obtain the analogous of Eq. (3.53), namely:

$$n_s(T) \simeq n_s(T=0) e^{-b' \left[ \frac{1}{\sqrt{1-T/T_c}} - 1 \right]}, \quad T \leq T_c \quad (3.54)$$

$$n_s(T=0) \simeq \frac{\delta}{2a_0^2}$$

where  $b'$  is a non-universal constant, in principle different from  $b$ . As we will discuss later, Eqs. (3.53) and Eq. (3.54) allow to track the temperature dependence of various physical quantities. In fact, we will fix the values of the non-universal constants  $b$  and  $b'$  by fitting to the experimental data. Indeed, we anticipate that these constants are seen to assume quite different values,  $b \sim \mathcal{O}(10^{-1})$  and  $b' \sim \mathcal{O}(10^0)$ .

### 3.2 Condensate in external magnetic fields

In this Section we are interested in the dynamics of the hole pair condensate in presence of an external magnetic field perpendicular to the copper-oxide plane:

$$\vec{h}(\vec{r}) = \nabla \times \vec{A}(\vec{r}) \quad , \quad \vec{A}(\vec{r}) = (A_1(\vec{r}), A_2(\vec{r}), 0), \quad (3.55)$$

where  $\vec{h}(\vec{r})$  is the microscopic magnetic field, and we adopt the London gauge  $\nabla \cdot \vec{A} = 0$ . The reduced Hamiltonian in the Schrödinger representation is still given by Eq. (3.1), but now:

$$\hat{H}_0 = \sum_{i=1}^N \frac{1}{2m_h^*} \left[ -i\hbar \nabla_{\vec{r}_i} - \frac{e}{c} \vec{A}(\vec{r}_i) \right]^2. \quad (3.56)$$

In this case the Schrödinger equation for two holes, Eq. (3.5), becomes:

$$\begin{aligned} \frac{1}{2m_h^*} \left( -i\hbar\nabla_{\vec{r}} - \frac{e}{c}\vec{A}(\vec{r}) \right)^2 \Phi(\vec{r}, \vec{r}') + \frac{1}{2m_h^*} \left( -i\hbar\nabla_{\vec{r}'} - \frac{e}{c}\vec{A}(\vec{r}') \right)^2 \Phi(\vec{r}, \vec{r}') \\ + V(\vec{r} - \vec{r}') \Phi(\vec{r}, \vec{r}') = \varepsilon \Phi(\vec{r}, \vec{r}') . \end{aligned} \quad (3.57)$$

Changing variables as in Eq. (3.6), we recast Eq. (3.57) into:

$$\begin{aligned} \frac{1}{4m_h^*} \left( -i\hbar\nabla_{\vec{R}} - \frac{2e}{c}\vec{A}(\vec{R}) \right)^2 \Phi(\vec{R}, \vec{\rho}) + \frac{1}{m_h^*} \left( -i\hbar\nabla_{\vec{\rho}} - \frac{e}{2c}\vec{A}(\vec{\rho}) \right)^2 \Phi(\vec{R}, \vec{\rho}) \\ + V(\vec{\rho}) \Phi(\vec{R}, \vec{\rho}) = \varepsilon \Phi(\vec{R}, \vec{\rho}) . \end{aligned} \quad (3.58)$$

Again, this allows to write:

$$\Phi(\vec{R}, \vec{\rho}) = \Psi(\vec{R}) \varphi(\vec{\rho}) , \quad (3.59)$$

and

$$\varepsilon = \varepsilon_{cm} - \Delta . \quad (3.60)$$

So that:

$$\frac{1}{4m_h^*} \left[ -i\hbar\nabla_{\vec{R}} - \frac{2e}{c}\vec{A}(\vec{R}) \right]^2 \Psi(\vec{R}) = \varepsilon_{cm} \Psi(\vec{R}) , \quad (3.61)$$

$$\left[ \frac{1}{m_h^*} \left( -i\hbar\nabla_{\vec{\rho}} - \frac{e}{2c}\vec{A}(\vec{\rho}) \right)^2 + V(\vec{\rho}) \right] \varphi(\vec{\rho}) = -\Delta \varphi(\vec{\rho}) . \quad (3.62)$$

Eq. (3.62) has been already discussed in I, Sect. 4.1. It turns out that the bound-state wavefunction  $\varphi(\vec{\rho})$  is practically unaffected by the magnetic field for applied magnetic field strengths employed in experiments,  $H \lesssim 100 T$ <sup>7</sup>. Moreover, the external magnetic field lifts the degeneracy with respect to the magnetic quantum number. However, the resulting Zeeman splitting is completely negligible such that  $\Delta \simeq \Delta_2(\delta)$ .

To determine the condensate wavefunction we proceed as in Sect. 3. Obviously, one finds that the wavefunction of the low-lying condensate excitation has the form given by Eq. (3.29) and it satisfies the Schrödinger-like eigenvalue equation:

$$\frac{1}{4m_h^*} \left[ -i\hbar\nabla - \frac{2e}{c}\vec{A}(\vec{R}) \right]^2 \chi(\vec{R}) = \varepsilon \chi(\vec{R}) , \quad (3.63)$$

where  $\varepsilon$  is the excitation energy with respect to the condensation energy. As expected, Eq. (3.63) shows that low-lying excitations of the condensate behave like quasi-particles with mass  $2m_h^*$  and positive charge  $+2e$ . Interestingly enough, we may write down the electromagnetic current for low-lying condensate excitations. In fact, we use the quantum-mechanics expression for the current density when a charged particle moves in a magnetic field<sup>8</sup> to get:

$$\begin{aligned} \vec{j}_{em}(\vec{R}) = 2e \vec{j}(\vec{R}) = \frac{-ie\hbar}{2m_h^*} \left[ \chi^*(\vec{R}) \nabla \chi(\vec{R}) - \nabla \chi^*(\vec{R}) \chi(\vec{R}) \right] \\ - \frac{2e^2}{m_h^* c} \chi^*(\vec{R}) \chi(\vec{R}) \vec{A}(\vec{R}) . \end{aligned} \quad (3.64)$$

<sup>7</sup>Even though we are using CGS units, it is customary in the literature to express the applied magnetic field in Tesla,  $1T = 10^4 G$ .

<sup>8</sup>See, for example, Ref. [57].

Using Eq. (3.29), and introducing the superfluid velocity:

$$\vec{v}_s(\vec{R}, \vec{A}) = \frac{\hbar}{2m_h^*} \nabla \Theta(\vec{R}) - \frac{e}{m_h^* c} \vec{A}(\vec{R}) , \quad (3.65)$$

it is easy to check that:

$$\vec{j}_{em}(\vec{R}) = 2e n_s \vec{v}_s(\vec{R}, \vec{A}) . \quad (3.66)$$

### 3.3 The roton gas and the specific heat anomaly

In this Section we address the problem of the specific heat anomaly close to the transition temperature  $T_c$ . The specific heat is one of the few bulk thermodynamic probe of the superconducting state. In high temperature cuprate superconductors the normal-superconducting transition is substantially broadened relative to that in many conventional superconductors. In classic superconductors there is a specific heat jump at the critical temperature. On the other hand, cuprate high temperature superconductors show both a pronounced peak or only a broad hump in the specific heat at the critical temperature  $T_c$ . In general, the broadened specific heat anomaly has been attributed to superconducting fluctuations (see, for example, the reviews in Refs. [58, 59] and references therein). For sake of definiteness, we will focus on the Yttrium compound  $\text{YBa}_2\text{Cu}_3\text{O}_{6+x}$  (YBCO) with superconducting critical temperatures up to  $T_c \simeq 93K$  [60]. Indeed, the measurements of specific heat on YBCO are more complete than those for any other high temperature superconductor. The specific heat anomaly in the YBCO sample shows a sharp peak structure. Customarily the specific heat anomaly is characterized by  $\Delta c(T_c)$ , the difference of the specific heat between the peak value with respect to the background lattice specific heat. Furthermore, it should be keep in mind that the analysis of the shape of the anomaly is always complicated by uncertainties in the subtraction of the background. It turns out that the specific heat jump is clearly seen at the superconducting transition, even though the specific heat anomaly at the critical temperature is only about a few percent of the total. For YBCO in the optimal doping region with  $T_c \simeq 87.5 K$ , from Fig. 5 of Ref. [58] we infer a specific heat anomaly:

$$\frac{\Delta c(T_c)}{T_c} \simeq 5 \cdot 10^{-3} \frac{J}{K^2 \text{ gat}} , \quad (3.67)$$

where  $\text{gat} = \text{gram} - \text{atom}$  is the volume occupied by  $N_A$  unit cell of the crystal,  $N_A$  being the Avogadro's number. Let  $V_u$  be the volume of the unit cell, then from Eq. (3.67) we may estimate the dimensionless specific heat anomaly:

$$V_u \frac{\Delta c(T_c)}{k_B} \simeq 5.26 \cdot 10^{-2} , \quad (3.68)$$

where  $k_B$  is the Boltzmann constant. The main advantage of the dimensionless specific heat anomaly resides in the fact that it can be directly compared with theoretical calculations within our model. In fact, we now show that in our approach the specific heat anomaly can be accounted for by the specific heat of the roton thermal gas.

The thermodynamics of the superconductive condensate is determined by the low-lying excitations. The previous Section showed that the condensate low-lying excitations are

the rotons which behave like quasi-particle with mass  $2m_h^*$ , charge  $2e$ , and temperature-dependent energy:

$$\varepsilon_{rot}(T) \simeq \alpha m_h^* \vec{v}_s^2(T) , \quad (3.69)$$

where:

$$|\vec{v}_s(T)| = v_s(T) \simeq v_s(0) e^{-b \left[ \frac{1}{\sqrt{1-T/T_c}} - 1 \right]} , \quad T \leq T_c . \quad (3.70)$$

Eqs. (3.69) and (3.70) imply that the roton energy vanishes continuously at the critical temperature. Therefore, near  $T_c$  there is a proliferation of thermally activated rotons which, therefore, dominate the thermodynamic potential. On the other hand, at low temperatures the excitation of rotons is exponentially suppressed since  $\varepsilon_{rot}(0) \sim \Delta_2(\delta)$ . Since rotons are bosons (like the phonons), the thermal distribution function is given by the Bose-Einstein distribution:

$$f(\varepsilon_{rot}) = \frac{1}{e^{\frac{\varepsilon_{rot}}{k_B T}} - 1} . \quad (3.71)$$

Our approximation amounts to deal with the roton gas as an ideal gas. We may, then, easily evaluate the roton energy density:

$$\mathbf{u}_{rot}(T) \simeq \int \frac{d\vec{k}}{(2\pi)^2} \varepsilon_{rot}(T) \frac{1}{e^{\frac{\varepsilon_{rot}(T)}{k_B T}} - 1} \delta\left(\frac{|\vec{k}|}{k_0} - 1\right) . \quad (3.72)$$

In Eq. (3.72) the Dirac  $\delta$ -function takes care of the fact that the roton wavenumber is constrained according to Eq. (3.43):

$$|\vec{k}_{rot}| \simeq k_0 \simeq \frac{2\pi}{d_0} \simeq 2\pi \sqrt{\frac{\delta}{2d_0^2}} . \quad (3.73)$$

A straightforward calculation gives:

$$\mathbf{u}_{rot}(T) \simeq \frac{\pi\delta}{a_0^2} \varepsilon_{rot}(0) f_{KT}(2b, T) \frac{1}{e^{\frac{\varepsilon_{rot}(0)f_{KT}(2b, T)}{k_B T}} - 1} \quad (3.74)$$

where, for convenience, we introduced the function:

$$f_{KT}(b, T) \equiv e^{-b \left[ \frac{1}{\sqrt{1-T/T_c}} - 1 \right]} . \quad (3.75)$$

From the roton internal energy density we may evaluate the specific heat at constant volume:

$$c_{rot}(T) = \frac{\partial \mathbf{u}_{rot}(T)}{\partial T} . \quad (3.76)$$

To compare the roton specific heat with experimental data we must take into account that the rotons are the low-lying excitations of the superfluid condensate. Therefore the rotons contribute to the specific heat only within the condensate fraction which share phase coherence. According to our previous discussion, at zero temperature all the hole pairs are condensed with phase coherence. However, at finite temperatures the phase-coherent condensate fraction is given by:

$$\frac{n_s(T)}{n_s(0)} = f_{KT}(b', T) , \quad (3.77)$$

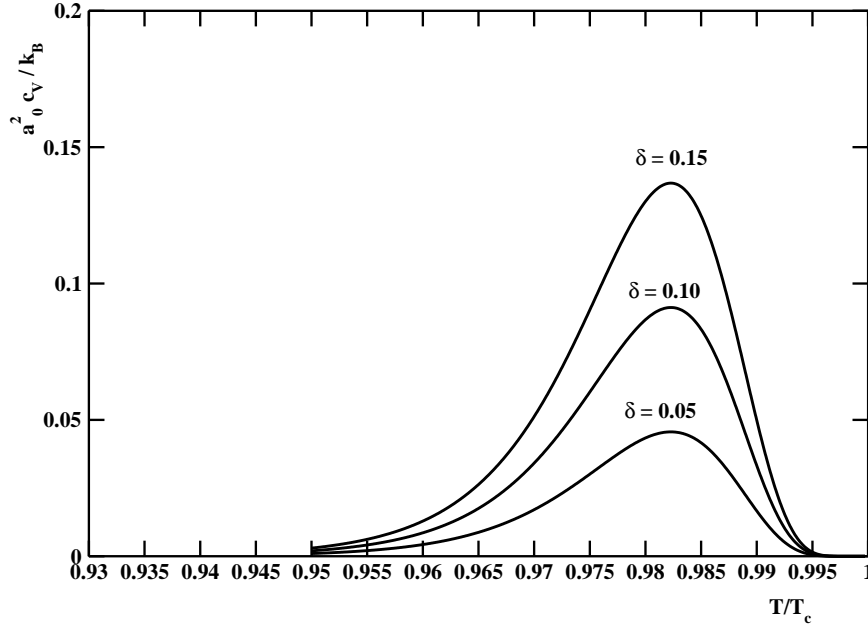


Figure 3: Dimensionless roton specific heat versus the reduced temperature for different hole doping levels.

according to Eqs. (3.54) and (3.75). Thus, the contribution of rotons to the specific heat at constant volume can be written as:

$$c_V(T) \simeq \frac{n_s(T)}{n_s(0)} c_{rot}(T) \simeq \frac{n_s(T)}{n_s(0)} \frac{\partial u_{rot}(T)}{\partial T} . \quad (3.78)$$

In Fig. 3 we display the temperature dependence of the dimensionless specific heat at constant volume for different hole doping levels. For our numerical estimates, we assumed  $b \simeq 0.193$ . As we will discuss later on, this value has been fixed by fitting the temperature dependence of the excitation energy of the nodal quasielectron liquid to the experimental data. As concern the parameter  $b'$ , we choose the value  $b' \simeq 0.80$  that it is relevant for the London penetration length in optimally doped YBCO (see Sect. 3.4). From Fig. 3 we see that, as expected, the roton specific heat is sizable in the critical region only. Moreover,  $c_V(T)$  displays a rather sharp peak at temperatures very near the critical temperature, with a well developed curvature below  $T_c$ . Note that this feature has no equivalent in classic superconductors and it is in fair agreement with observations (see, for instance, Fig. 6 in Ref. [58]). Finally, we see that the roton specific heat scales almost linearly with the hole doping  $\delta$  in agreement with several measurements in the pseudogap region.

From Fig. 3 we estimate the dimensionless specific heat anomaly near the optimal doping:

$$a_0^2 \frac{\Delta c_V(T_c)}{k_B} \sim 10 \cdot 10^{-2} . \quad (3.79)$$

Comparing this estimate with Eq. (3.68), we may safely conclude that the thermal roton gas can account, both qualitatively and quantitatively, for the observed specific heat anomaly in hole doped cuprate superconductors in the pseudogap region.

Let us conclude this Section by briefly discussing the effects of an applied magnetic field on the specific heat anomaly. Experimentally, it results that a magnetic field applied along the normal direction to the  $CuO_2$  planes strongly suppresses the specific heat

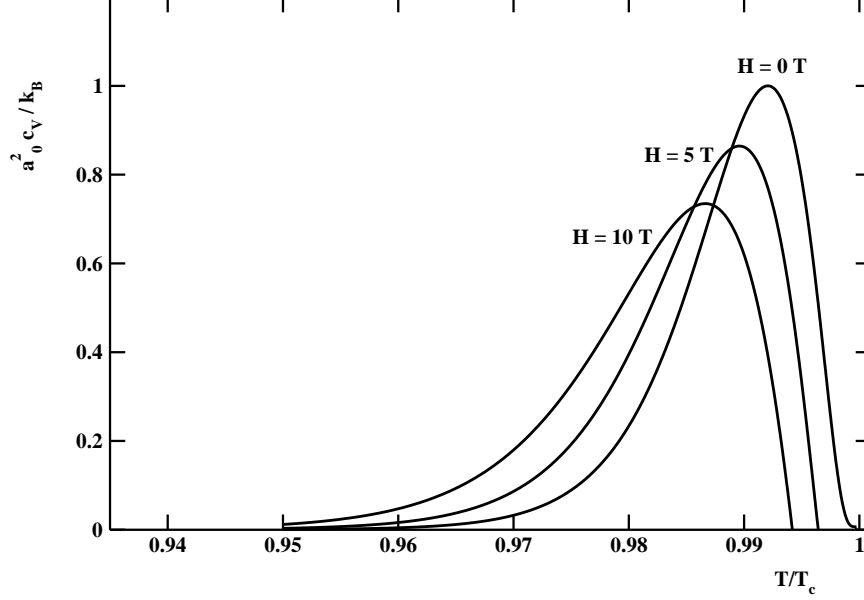


Figure 4: Dimensionless roton specific heat versus the reduced temperature at hole doping  $\delta = 0.10$  for different magnetic field strengths. The curves are normalized such that at  $H = 0$  the maximum of  $a_0^2 \frac{c_V}{k_B}$  is set to 1.0.

anomaly at  $T_c$ , while the effect of magnetic fields applied parallel to the  $CuO_2$  planes is much less pronounced. Moreover, the magnetic field shifts the specific heat anomaly to lower temperatures without strongly affecting the critical temperature  $T_c$ . In Sect. 3.2 we have seen that the electromagnetic current can be written in term of the field-dependent superfluid velocity  $\vec{v}_s(\vec{R}, \vec{A})$ , Eq. (3.65). Evidently, at finite temperatures we have:

$$\vec{v}_s(T, \vec{A}) = \vec{v}_s(T) - \frac{e}{m_h^* c} \vec{A}(\vec{R}), \quad (3.80)$$

with:

$$\vec{v}_s(T) = \vec{v}_s(0) e^{-b \left[ \frac{1}{\sqrt{1-T/T_c}} - 1 \right]}. \quad (3.81)$$

In the mixed state the magnetic field penetrates into the superconductor with an array of Abrikosov vortices (see Sect. 3.5). The roton excitations are present outside the Abrikosov vortices. The effects of the magnetic field on these roton excitations amount to shifting the superfluid velocity  $\vec{v}_s$  according to Eq. (3.80). To estimate the magnetic field at the roton site, we recall that rotons are disturbances of the superfluid condensate of size  $\sim d_0$ . Within the roton core the condensate loses the phase coherence, so that the roton core constitutes a region of normal fluid. Moreover, the screening of the roton velocity  $\vec{v}_s(\vec{R})$  is due to Kosterlitz-Thouless vortex-antivortex pairs. Evidently, the screening of the magnetic field due to a given Kosterlitz-Thouless vortex is compensated by the corresponding antivortex. Then, we may safely assume that the magnetic field in the roton region coincides with the external magnetic field  $H$ . This means that in the vortex core  $\nabla \times \vec{A}(\vec{R}) \simeq \vec{H}(\vec{R})$ . Since the size of the roton is very small, we may consider the magnetic field  $\vec{H}(\vec{R})$  almost constant within the roton core and obtain the roughly estimate:

$$|\vec{A}(\vec{R})| \simeq H d_0 \simeq H \sqrt{\frac{2a_0^2}{\delta}}. \quad (3.82)$$

Accordingly, we find for the roton energy:

$$\varepsilon_{rot}(T, H) \simeq \alpha m_h^* \vec{v}_s^2(T, \vec{A}) \simeq \alpha m_h^* \left[ v_s(T) - \frac{eH}{m_h^* c} d_0 \right]^2. \quad (3.83)$$

Now, we proceed as before and obtain the roton energy density by simply replacing in Eq. (3.72) the roton energy  $\varepsilon_{rot}(T)$  with  $\varepsilon_{rot}(T, H)$  given by Eq. (3.83). After that, the roton specific heat is given by Eq. (3.76).

In Fig. 4 we show the dimensionless roton specific heat at hole doping  $\delta = 0.10$  for different magnetic field strengths, and using the same values of the parameters as before. Qualitatively the effect of the magnetic field is to shift the peak in the roton specific heat and to reduce the peak value. In fact, these features are in qualitative agreement with experimental observations.

### 3.4 The London penetration length

In this Section we discuss the magnetic properties of our ideal planar superconductor. Let us assume that the superconductor is immersed in an external constant magnetic field of strength  $H_0$  perpendicular to the  $CuO_2$  plane. If the magnetic field does not exceed the lower critical field  $H_{c1}$ , then the external field does not penetrate into the superconductor (Meissner effect) so that the magnetic induction  $B$  vanishes,  $B = 0$ . However, it should be mentioned that, in fact, the magnetic field penetrates into the superconductor to a depth given by the London penetration length  $\lambda(T)$  which depends on the temperature. Let  $\vec{h}(\vec{R})$  be the microscopic magnetic field. The macroscopic field is defined as the spatial average of  $\vec{h}(\vec{R})$ :

$$\langle \vec{h}(\vec{R}) \rangle_{\text{vol}} = \vec{B}(\vec{R}). \quad (3.84)$$

Let us consider, now, a homogeneous superconductor in thermodynamic equilibrium. In this case there is no normal current, so that the electromagnetic current is given by Eq. (3.65) that we rewrite as:

$$\vec{j}_{em}(\vec{R}) = \frac{e\hbar}{m_h^*} n_s \nabla \Theta(\vec{R}) - \frac{2e^2}{m_h^* c} n_s \vec{A}(\vec{R}), \quad (3.85)$$

where:

$$\vec{h}(\vec{R}) = \nabla \times \vec{A}(\vec{R}). \quad (3.86)$$

Moreover, within our approximations to obtain gauge invariant results we need to adopt the physical London gauge:

$$\nabla \vec{A}(\vec{R}) = 0. \quad (3.87)$$

In fact our reduced Hamiltonian approximation is similar to the reduced BCS Hamiltonian. It is known since long time that the simple BCS pairing approximation gives an accurate account of the response of the system to transverse electromagnetic fields, but it does not give the correct response to longitudinal fields. Indeed, it was soon realized [61, 62, 63] that this difficulty can be overcome once one realizes that the longitudinal gauge potential couples primarily to the collective density fluctuation mode. The density fluctuation modes correspond to collective plasma oscillations of the charged condensate. Since there are no low-lying collective oscillations due to the Coulomb interaction, the

contributions of the longitudinal vector potential to the electromagnetic current are negligible. In other words, when the gauge is chosen so that  $\nabla \vec{A}(\vec{R}) = 0$  one is guaranteed that gauge invariance is maintained.

From the Maxwell equation:

$$\nabla \times \vec{h}(\vec{R}) = \frac{4\pi}{c} \vec{j}_{em}(\vec{R}) , \quad (3.88)$$

we get:

$$\nabla \times \nabla \times \vec{h}(\vec{R}) = \frac{4\pi}{c} \nabla \times \vec{j}_{em}(\vec{R}) . \quad (3.89)$$

Using Eq. (3.85) we obtain readily:

$$\nabla \times \nabla \times \vec{h}(\vec{R}) = - \frac{1}{\lambda^2(T)} \vec{h}(\vec{R}) , \quad (3.90)$$

where:

$$\frac{1}{\lambda^2(T)} = \frac{8\pi e^2}{m_h^* c} n_s(T) . \quad (3.91)$$

Since  $\nabla \cdot \vec{h}(\vec{R}) = 0$ , Eq. (3.90) leads to:

$$\nabla^2 \vec{h}(\vec{R}) = \frac{1}{\lambda^2(T)} \vec{h}(\vec{R}) , \quad (3.92)$$

which shows that  $\lambda(T)$  is the London penetration length. To obtain Eq. (3.90) we assumed  $\nabla \times \nabla \theta(\vec{R}) = 0$ , which corresponds to irrotational superfluid flow. As discussed in Sect. 3.5, if the external magnetic field exceeds the lower critical field  $H_{cl}$ , then it is thermodynamically favored the formation of Abrikosov vortices where  $\nabla \theta(\vec{R})$  develops a singularity. The temperature dependence of the London penetration length results from the temperature behavior of the superfluid condensate, Eq. (3.54). Accordingly, we can write:

$$\begin{aligned} \frac{1}{\lambda^2(T)} &= \frac{1}{\lambda^2(0)} e^{-b' \left[ \frac{1}{\sqrt{1-T/T_c}} - 1 \right]} , \\ \frac{1}{\lambda^2(0)} &= \frac{8\pi e^2}{m_h^* c} n_s(0) , \quad n_s(0) \simeq \frac{\delta}{2a_0^2} . \end{aligned} \quad (3.93)$$

The peculiar temperature behavior of the London penetration length implied by Eq. (3.93) can be contrasted with experimental observations in cuprate superconductors in the pseudogap region. In fact, we checked that our results are in satisfying agreement with observations. In the remainder of the present Section we present some representative examples in the highly underdoped and optimal doped regions for different compound of copper-oxide superconductors. In Fig. 5 we display the penetration length at finite temperatures for highly underdoped  $YBa_2Cu_3O_{6+x}$  superconductors with critical temperatures  $T_c = 8.4 K, 13.0 K, 17.9 K$  respectively. The corresponding doping level  $\delta$  can be inferred from the phenomenological parabolic relationship [64, 65, 66]:

$$1 - \frac{T_c(\delta)}{T_c^{max}} = 82.6 (\delta - 0.16)^2 , \quad T_c^{max} \approx 98 K . \quad (3.94)$$



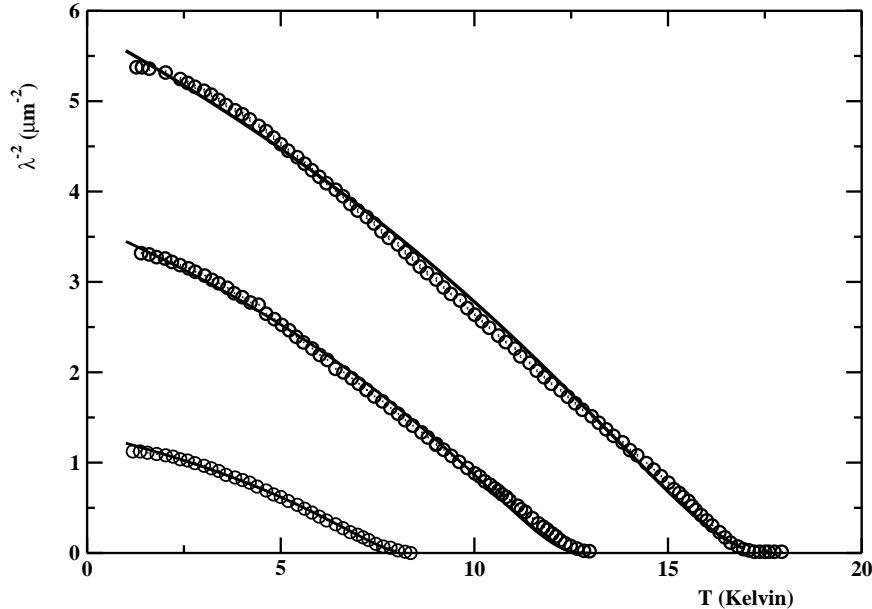


Figure 5: The London penetration length versus the temperature for highly underdoped YBCO superconductor. The data has been taken from Fig. 2 of Ref. [67]. The solid curves are the fits of the data to Eq. (3.93).

The data have been extracted from Fig. 2 of Ref. [67] where it is displayed the London penetration length for YBCO with 20 different doping levels and critical temperatures ranging from  $T_c \simeq 3 K$  up to  $T_c \simeq 17 K$ . We fitted the data to our Eq. (3.90) leaving as free parameters the non-universal constant  $b'$  and  $\frac{1}{\lambda^2(0)}$ . To implement the fits we used the program Minuit [68] which is conceived as a tool to find the minimum value of a multi-parameter function and analyze the shape of the function around the minimum. The principal application is to compute the best-fit parameter values and uncertainties by minimizing the total chi-square  $\chi^2$ . As rule of thumb, a sensible fit results in  $\chi_r^2 \sim 1$ , where  $\chi_r^2$  is the reduced chi-square, namely the total chi-square divided by the number of degree of freedom. Remarkably, we found that Eq. (3.90), with  $b' \simeq 1.40$ , gives a fit with  $\chi_r^2 \sim 1$ , in quite good agreements with the experimental data (see Fig. 5). Moreover, the fits returned values of  $\frac{1}{\lambda^2(0)}$  which were quite consistent with the ones reported in Ref. [67], Fig. 3. Note, however, that to compare our theoretical estimate for  $\lambda(0)$  to measurements, we must slightly modify our result which is relevant for a planar superconductor:

$$\frac{1}{\lambda^2(0)} = \frac{8\pi e^2}{m_h^* c} n_s(0) \simeq \frac{8\pi e^2}{m_h^* c} \frac{\delta}{2a_0^2 c_0}. \quad (3.95)$$

We found that, by using the numerical values of the model parameters, Eq. (3.95) gives the correct order of magnitude for the zero-temperature London penetration length. In addition, the linear dependence of  $\frac{1}{\lambda^2(0)}$  on the doping  $\delta$  is consistent with experimental observations (see Fig. 3. in Ref. [67]).

We have also compared our peculiar temperature dependence of the penetration length with experimental observations for three different class of cuprate superconductors in the optimal doping region. In Fig. 6 we display the observed temperature behavior of the normalized London penetration length for very high quality single crystal optimal

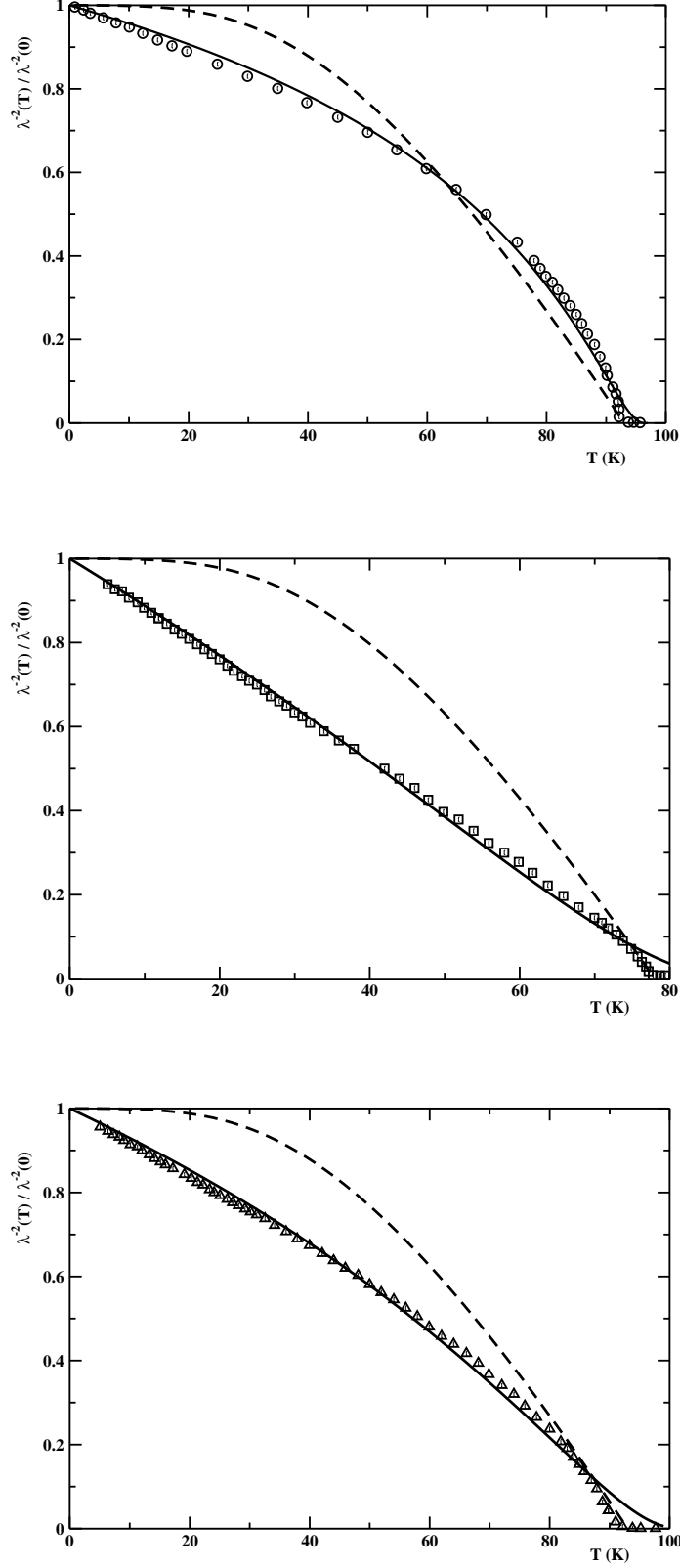


Figure 6: (Top) London penetration length versus the temperature in the optimal doping region for YBCO,  $T_c = 93\text{ K}$ , (Middle) Tl-2201  $T_c = 78\text{ K}$ , (Bottom) BSCCO,  $T_c = 93\text{ K}$ . The solid lines are the fits of the data to Eq. (3.93). The dashed lines are the London penetration length in the weak-coupling d-wave BCS theory, Eq. (A.34).

doped  $YBa_2Cu_3O_{6.95}$ ,  $T_c = 93\text{ K}$ , single crystal  $Tl_2Ba_2CuO_{6+\delta}$  (Tl-2201),  $T_c = 78\text{ K}$ , and high-quality single crystal  $Bi_2Sr_2CaCu_2O_6$  (BSCCO),  $T_c = 93\text{ K}$ . The temperature dependence of the London penetration length in YBCO has been obtained in Ref. [69] by microwave techniques which allow to track the deviations of  $\lambda(T)$  from its zero temperature value. We extracted the data from Fig. 12 in Ref. [70]. For Tl-2201, Ref. [71] reports the measurements of the in-plane microwave conductivity which allowed to extract the variations of the London penetration length with the temperature. The data has been taken from Fig. 3 in Ref. [71]. Finally, for BSCCO the data have been taken from Fig. 3 in Ref. [72] where the temperature dependence of  $\lambda(T)$  has been obtained from the in-plane microwave surface impedance.

We fitted the data to Eq. (3.93) leaving  $b'$  and  $T_c$  as free parameters. The results of our fits are displayed as full lines in Fig. 6. Concerning the fitted values of the parameters, we obtained  $b' \simeq 0.80$ ,  $T_c \simeq 97.0\text{ K}$  (YBCO),  $b' \simeq 2.05$ ,  $T_c \simeq 93.7\text{ K}$  (Tl-2201), and  $b' \simeq 1.41$ ,  $T_c \simeq 103.8\text{ K}$  (BSCCO). Fig. 6 shows that our proposal for the temperature dependence of the London penetration length, Eq. (3.95), seems to be in reasonable agreements with experimental measurements, at least for temperatures not too close to the critical temperature. To appreciate better this point, in Fig. 6 we also compare the data with the weak-coupling d-wave BCS prediction (see Eq. (A.34) in Appendix A). It seems evident that our best fits to Eq. (3.95) compare much better with experimental data. Near the critical temperature  $T_c$  there are deviations of the data with respect to Eq. (3.95). Moreover, the best-fit values for the critical temperatures are systematically slightly higher than the observed  $T_c$ . These features, however, are to be expected. In fact, we already noticed that our mean field approximation could be questionable in the optimal doping region due to the enhanced role of phase fluctuations in the crossover from the pseudogap to the d-wave BCS gap. In fact, it is known that the mean field critical temperature tends to overestimate the actual value of  $T_c$  due to sizable fluctuations in the critical region. As regard the parameter  $b'$ , we already remarked that this parameter is not universal, so that it could, in principle, depends on the crystal structure, on the presence of disorder and defects, and also on the hole doping fraction. In any case, as anticipated, we found that  $b' \sim 1$ .

### 3.5 Vortex structure and critical magnetic fields

We obtained the London equation Eq. (3.90) assuming an irrotational superfluid flow. Let, now, relax this assumption by letting  $\nabla\theta(\vec{R})$  to develop a singularity. Thus, from Eq. (3.88) we have:

$$\nabla \times \vec{h}(\vec{R}) = \frac{4\pi e\hbar}{m_h^*c} n_s(T) \nabla \Theta(\vec{R}) - \frac{8\pi e^2}{m_h^*c^2} n_s(T) \vec{A}(\vec{R}). \quad (3.96)$$

Using Eq. (3.91) we rewrite this last equation as:

$$\nabla \times \vec{h}(\vec{R}) = \frac{1}{\lambda^2(T)} \left[ \frac{\phi_0}{2\pi} \nabla \Theta(\vec{R}) - \vec{A}(\vec{R}) \right], \quad (3.97)$$

where

$$\phi_0 = \frac{2\pi\hbar c}{2e} \simeq 2.07 \cdot 10^{-7} \text{ G cm}^2 \quad (3.98)$$

is the elementary quantum flux. Let us consider the simplest case of an isolated singularity at the origin  $\vec{R} = 0$ . From Eq. (3.97) we obtain:

$$\vec{h}(\vec{R}) + \lambda^2(T) \nabla \times \nabla \times \vec{h}(\vec{R}) = \frac{\phi_0}{2\pi} \nabla \times \nabla \Theta(\vec{R}) . \quad (3.99)$$

Now, we consider the following integral extended over the surface of a small circle centered at the origin:

$$\int \left[ \nabla \times \nabla \Theta(\vec{R}) \right] \cdot d\vec{S} . \quad (3.100)$$

Using the Stokes's theorem we have:

$$\int \left[ \nabla \times \nabla \Theta(\vec{R}) \right] \cdot d\vec{S} = \oint \nabla \Theta(\vec{R}) \cdot d\vec{l} = 2\pi \quad (3.101)$$

since the phase  $\Theta$  changes by  $2\pi$  after a full circle around the singularity. Therefore, we are led to:

$$\nabla \times \nabla \Theta(\vec{R}) = 2\pi \delta(\vec{R}) , \quad (3.102)$$

so that the singularity in  $\nabla \Theta(\vec{R})$  carries one flux quantum showing, thereby, that it coincides with an isolated Abrikosov vortex. In fact, Eq. (3.99) gives:

$$\vec{h}(\vec{R}) + \lambda^2(T) \nabla \times \nabla \times \vec{h}(\vec{R}) = \phi_0 \delta(\vec{R}) , \quad (3.103)$$

or, better:

$$h(\vec{R}) - \lambda^2(T) \nabla^2 h(\vec{R}) = \phi_0 \delta(\vec{R}) . \quad (3.104)$$

The solution of Eq. (3.104) is the well-known Abrikosov vortex field distribution:

$$h(R) = \frac{\phi_0}{2\pi\lambda^2(T)} K_0\left(\frac{R}{\lambda(T)}\right) , \quad (3.105)$$

where  $K_n(x)$  is the modified Bessel function of order  $n$ . Since

$$K_0(x) \stackrel{x \rightarrow 0}{\sim} \ln\left(\frac{1}{x}\right) , \quad K_0(x) \stackrel{x \rightarrow \infty}{\sim} \frac{1}{\sqrt{x}} e^{-x} , \quad (3.106)$$

we see that the magnetic field decreases exponentially at large distance, but it diverges logarithmically at the vortex center. However, Eq. (3.105) is no longer valid in the vortex core, namely in a region of linear size  $\xi_V$  around the vortex center, where the condensate loses the superfluidity. According to our model, since we are considering temperatures  $T \lesssim T^*$ , we still have bound holes which, however, have lost the phase coherence. To determine  $\xi_V$  we use Eq. (3.88) to determine the superconductivity current density outside the vortex core:

$$j(R) \equiv |\vec{j}_{em}(\vec{R})| = \frac{c}{4\pi} |\nabla \times \vec{h}(\vec{R})| \simeq \frac{c\phi_0}{8\pi^2\lambda^2} \frac{1}{R} , \quad r \gtrsim \xi_V . \quad (3.107)$$

Since outside the vortex core we have  $j \simeq 2e n_s v_s$ , we may estimate the vortex core radius as:

$$j(\xi_V) \simeq 2e n_s v_c , \quad (3.108)$$

where  $v_c$  is the critical velocity given by <sup>9</sup>

$$m_h^* v_c^2 \simeq \Delta_2(\delta) . \quad (3.109)$$

As discussed in I, the meaning of the critical velocity is that for velocities greater than  $v_c$  the condensate phase coherence is lost. Combining Eqs. (3.107) and (3.108) we obtain:

$$\frac{1}{\xi_V} \simeq \frac{2m_h^*}{\hbar} v_c \simeq \sqrt{\frac{4m_h^*}{\hbar^2}} \Delta_2(\delta) . \quad (3.110)$$

Within our approximations, it is easy to check that Eq. (3.110) implies that  $\xi_V \lesssim d_0$ . Now, we know that  $d_0$  is the average distance between hole pairs. so that, obviously, the vortex core size cannot be smaller than  $d_0$ , thereby we must argue that:

$$\xi_V \simeq d_0 . \quad (3.111)$$

Having determined the vortex core size, presently we estimate the magnetic field at the center of the vortex by using Eq. (3.105) by setting a cut-off at  $R \simeq \xi_V$ :

$$h(0) \simeq \frac{\phi_0}{2\pi\lambda^2(T)} \ln\left(\frac{\lambda}{\xi_V}\right) \simeq \frac{\phi_0}{2\pi\lambda^2(T)} \ln\left(\frac{\lambda(T)}{d_0}\right) . \quad (3.112)$$

For temperatures not too close to the critical temperature  $T_c$ , where the isolated Abrikosov vortex approximation is usually not tenable, we may neglect in the logarithm the temperature dependence of the London penetration length obtaining :

$$h(0) \simeq \frac{\phi_0}{2\pi\lambda^2(T)} \ln(\kappa) , \quad (3.113)$$

where we introduced the analogous to the Ginzburg-Landau  $\kappa$ -parameter:

$$\kappa \simeq \frac{\lambda(0)}{d_0} . \quad (3.114)$$

It is interesting to estimate the value of the parameter  $\kappa$ . With our approximations, one obtains:

$$\kappa \simeq \sqrt{\frac{m_h^* c^2}{8\pi}} \frac{c_0}{c^2} . \quad (3.115)$$

Using the numerical values of the microscopic parameters we see that  $\kappa \sim 10^2$  confirming that the hole doped cuprates are extreme type-II superconductors [73].

We turn, now, on the determination of the lower critical magnetic field  $H_{c1}$ , namely the lowest magnetic field strength at which formation of Abrikosov vortices are thermodynamically favorable. First, we need to evaluate the free energy density in presence of an isolated Abrikosov vortex. Evidently we have:

$$\mathcal{F}_{sH} = \mathcal{F}_{s0} + \frac{1}{8\pi} \vec{h}^2(\vec{R}) + \varepsilon_{kin} , \quad (3.116)$$

---

<sup>9</sup>See Eq. (4.28) in I.

where  $\varepsilon_{kin}$  is the kinetic energy density of the supercurrent. We have seen that:

$$\begin{aligned} \varepsilon_{kin} &\simeq n_s m_h^* \vec{v}_s^2(\vec{R}, \vec{A}) \quad , \\ \vec{v}_s(\vec{R}, \vec{A}) &= \frac{\hbar}{2m_h^*} \nabla \Theta(\vec{R}) - \frac{e}{m_h^* c} \vec{A}(\vec{R}) \quad . \end{aligned} \quad (3.117)$$

Using Eq. (3.85) we rewrite the kinetic energy as:

$$\varepsilon_{kin} \simeq \frac{m_h^*}{4e^2 n_s} \vec{j}_{em}^2 \quad . \quad (3.118)$$

With the aid of the Maxwell equation Eq. (3.88) we obtain:

$$\varepsilon_{kin} \simeq \frac{1}{8\pi} \lambda^2 [\nabla \times \vec{h}(\vec{R})]^2 \quad . \quad (3.119)$$

Therefore we end with:

$$\mathcal{F}_{sH} = \mathcal{F}_{s0} + \frac{1}{8\pi} \left\{ \vec{h}^2(\vec{R}) + \lambda^2 [\nabla \times \vec{h}(\vec{R})]^2 \right\} \quad . \quad (3.120)$$

Whereupon, the variation of the free energy due to the presence of an isolated Abrikosov vortex is given by:

$$\Delta F_V = \int d\vec{R} \left( \mathcal{F}_{sH} - \mathcal{F}_{s0} \right) \simeq + \frac{1}{8\pi} \int d\vec{R} \left\{ \vec{h}^2(\vec{R}) + \lambda^2 [\nabla \times \vec{h}(\vec{R})]^2 \right\} \quad . \quad (3.121)$$

After some standard manipulations<sup>10</sup>, we get:

$$\Delta F_V \simeq \frac{1}{8\pi} \int d\vec{R} \vec{h}(\vec{R}) \cdot \left\{ \vec{h}(\vec{R}) + \lambda^2 \nabla \times \nabla \times \vec{h}(\vec{R}) \right\} \quad , \quad (3.122)$$

or, using Eq. (3.103)

$$\Delta F_V \simeq \frac{\phi_0}{8\pi} h(0) \simeq \frac{\phi_0^2}{16\pi^2 \lambda^2(T)} \ln(\kappa) \quad . \quad (3.123)$$

However, we need to take care of the energy due to the vortex core. Usually, the core energy can be neglected due to the fact that the vortex core being in the normal non-superconductive phase does not contribute to  $\Delta F_V$ . In our theory the normal phase in the core region corresponds to phase-disordered hole pairs. On the other hand, we have estimate that  $\xi_V \simeq d_0$ . Then, the vortex core energy corresponds to the energy of a region of disordered hole pair condensate of linear size  $d_0$ , implying that the vortex core energy coincides with the excitation energy of rotons. Therefore, we can write for the free energy of an isolated Abrikosov vortex:

$$\varepsilon_{vor}(T) \simeq \varepsilon_{em}(T) + \varepsilon_{core}(T) \quad , \quad (3.124)$$

where

$$\varepsilon_{em}(T) \simeq \frac{\phi_0^2}{16\pi^2 \lambda^2(T)} \ln(\kappa) \quad , \quad (3.125)$$

---

<sup>10</sup>See, for instance, Ref. [74].

is the energy of the magnetic field and the supercurrent associated to the vortex, and

$$\varepsilon_{core}(T) \simeq \frac{1}{c_0} \varepsilon_{rot}(T) \quad (3.126)$$

is the vortex core energy per unit length. Eq. (3.124) shows that the free energy of an isolated Abrikosov vortex is positive, i.e. the vortex cannot exist in the superconductor in absence of an external magnetic field. To determine the minimum value of the external magnetic field strength at which Abrikosov vortex formation becomes favorable, we need to minimize the Gibbs free energy (see, for instance, Ref. [75]):

$$G = \varepsilon_{vor}(T) - \frac{1}{4\pi} \int d\vec{R} \, \vec{H}_0 \cdot \vec{h}(\vec{R}) , \quad (3.127)$$

where  $H_0$  is the applied magnetic field with constant field strength. Since the Abrikosov vortex carries one magnetic flux quantum, from Eq. (3.127) one obtains at once:

$$G = \varepsilon_{vor}(T) - \frac{1}{4\pi} \phi_0 H_0 . \quad (3.128)$$

It is evident from Eq. (3.128) that for weak external field  $G > 0$  and there is no vortex formation. For external fields exceeding the lower critical field:

$$H_{c1} = \frac{4\pi}{\phi_0} \varepsilon_{vor}(T) \quad (3.129)$$

it is energetically favorable to produce Abrikosov vortices. Using Eqs. (3.124) - (3.126) we find:

$$H_{c1}(T) = H_{c1}^{em}(T) + H_{c1}^{core}(T) , \quad (3.130)$$

with:

$$H_{c1}^{em}(T) \simeq \frac{\phi_0}{4\pi\lambda^2(T)} \ln(\kappa) , \quad (3.131)$$

and

$$H_{c1}^{core}(T) \simeq \frac{4\pi}{c_0\phi_0} \varepsilon_{rot}(T) . \quad (3.132)$$

Note that our result is considerably different from conventional BCS superconductors where the vortex core energy is negligible in extreme type-II superconductors. In our model the lower critical magnetic field can be considerable larger than in BCS superconductors. In fact, as we will see in Sect. 3.6,  $H_{c1}^{core}$  turns out to be comparable to  $H_{c1}^{em}$ .

As concern the upper critical field  $H_{c2}$ , we recall that in BCS superconductors  $H_{c2}$  is given by the Cooper pair-breaking critical field. Moreover, the pair-breaking critical field is of the same order of the depairing field and of the Ginzburg-Landau critical field, defined as the magnetic field strength such that the Abrikosov vortices became to overlap. In our model, however, it turns out that both the pair-breaking and Ginzburg-Landau critical fields are much higher than the depairing field (see I, Sect. 4.2). In fact we found [22] that the upper critical magnetic field is given by the depairing field:

$$H_{c2}(T) \simeq \kappa^2 \frac{8\pi e}{c} n_s(T) \sqrt{\frac{\Delta_2(\delta)}{m_h^*}} . \quad (3.133)$$

As the applied magnetic field exceeds  $H_{c1}$ , more and more Abrikosov vortices are found. Increasing the strength of the external magnetic field these vortices become more dense and, eventually, their cores overlap so that the medium becomes normal. In conventional superconductors, the field at which this happens is the upper critical field. Within the Ginzburg-Landau formulation one introduces the Ginzburg-Landau coherence length  $\xi_{GL}$  such that:

$$H_{c2}(T) \simeq \frac{\phi_0}{\pi \xi_{GL}^2(T)} . \quad (3.134)$$

Interestingly enough, if we define the Ginzburg-Landau coherence length  $\xi_{GL}$  using Eq. (3.134) with the upper critical field given by Eq. (3.133), then the usual Ginzburg-Landau  $\kappa$ -parameter is:

$$\kappa_{GL} \simeq \frac{\lambda(T)}{\xi_{GL}(T)} . \quad (3.135)$$

After some manipulations, we find:

$$\kappa_{GL} \simeq \kappa \left[ \Delta_2(\delta) \frac{m_h^* c_0^2}{\hbar^2} \right]^{\frac{1}{4}} . \quad (3.136)$$

Using Eq. (2.14) we readily get:

$$\kappa_{GL} \simeq 1.44 \kappa \left[ 1 - \left( \frac{\delta}{\delta^*} \right)^{1.5} \right]^{\frac{1}{4}} . \quad (3.137)$$

For hole doping not too close to  $\delta^*$ , where our mean field approximation is anyway questionable, we see that  $\kappa_{GL}$  is almost independent on the hole doping and, in addition,  $\kappa_{GL} \sim \kappa$ .

In the subsequent Section we shall compare the temperature dependence of the critical magnetic fields, Eqs. (3.130) and (3.133), with experimental data. In the remainder of the present Section we intend to compare to experimental measurements the peculiar doping dependence implied by Eq. (3.133) for the upper critical magnetic field at zero temperature. In Fig. 7 we report the low-temperature upper critical magnetic field for the hole doped cuprates  $La_{2-x}Sr_xCuO_4$  (LSCO) and YBCO in the pseudogap region  $\delta \lesssim \delta^*$ . For LSCO in lightly doped region the estimate of the critical depairing field has been obtained in Ref. [76] from field suppression of the purely diamagnetic term in the effective magnetization measured by torque magnetometry. It is interesting to point out that the authors of Ref. [76] also reported that torque magnetometry measurements indicated that phase-disordered condensate survived up to  $\delta = 0.03 < \delta_{min}$ , while, in zero magnetic field, quantum phase fluctuations were seen to destroy superconductivity at  $\delta \simeq 0.055$ . These experimental observations give support to our theory where, in the pseudogap region, the superconductive transition is driven by phase fluctuations. In the optimally doped LSCO, the data have been extracted from Fig. 18 in Ref. [77]. The upper critical magnetic field has been estimated from Nernst signal at the lowest available temperature  $T = 4.2K$ . In Fig. 7, top panel, we compare our theoretical result Eq. (3.133) by assuming  $\kappa \simeq 130$ . Indeed, it seems that our model calculations compare quite well with measurements. In the bottom panel we report the upper critical magnetic field for YBCO in the pseudogap region. The data have been taken from Table 1 in Ref. [78]. The upper critical magnetic field was defined as the zero-temperature limit of  $H_{vs}(T)$  within the theory of



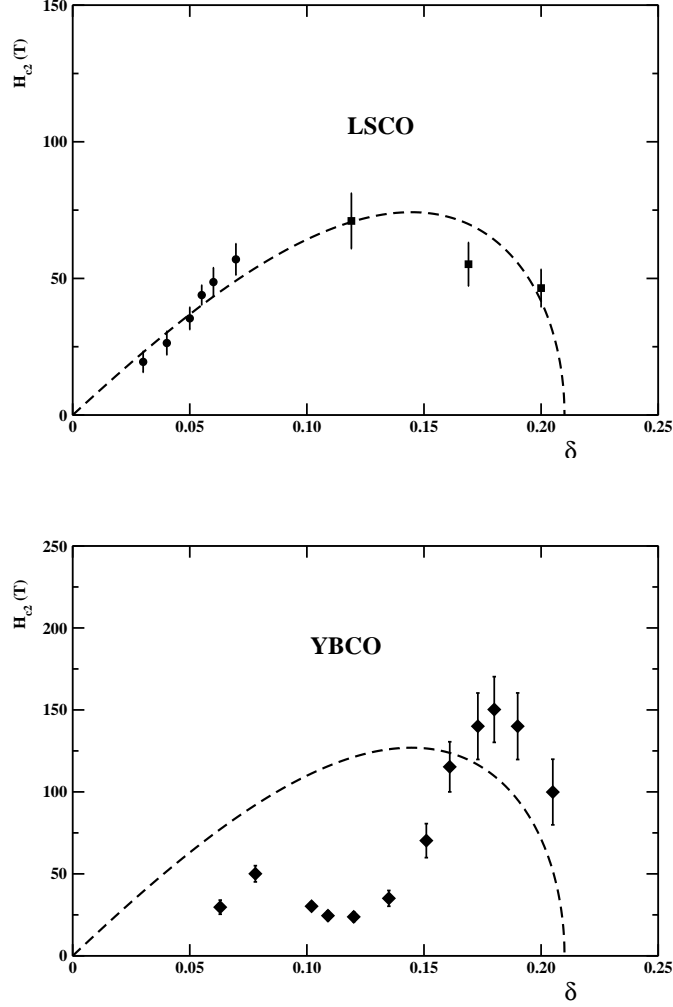


Figure 7: (Top) Upper critical magnetic field at low temperatures for LSCO versus the hole doping fraction. Data have been extracted from Ref. [76] (full circles) and Ref. [77] (full squares). The dashed line is Eq. (3.133) with  $\kappa \simeq 130$ . (Bottom) Upper critical magnetic field at low temperatures for YBCO versus the hole doping fraction. Data have been taken from Table 1 in Ref. [78]. The dashed line is Eq. (3.133) with  $\kappa \simeq 170$ .

vortex-lattice melting. The critical magnetic field  $H_{vs}(T)$  was determined from high-field resistivity data as the critical field below which the resistance is zero. These data are compared to Eq. (3.133) with  $\kappa \simeq 170$ . In this case we see that, for  $\delta \lesssim 0.15$ , the upper critical magnetic field  $H_{c2}$  seems to be suppressed with respect to the theoretical expectations. We believe that this sudden drop in  $H_{c2}$  is revealing the presence of a competing phase which weakens the superconductivity. In fact, it is already known the existence of competing order due to presumably the onset of incommensurate spin modulations detected by neutron scattering and muon spectroscopy [79, 80, 81].

### 3.6 Temperature dependence of the critical magnetic fields

In this Section we would like to check the temperature dependence of the critical magnetic fields by comparing to available experimental data. For reasons of space, we have made a selection of representative examples. According to our previous discussion the dependence of the critical fields, Eq. (3.130) and Eq. (3.133), on the temperature is basically due to  $n_s(T)$  and  $\varepsilon_{rot}(T)$ . Let us consider, firstly, the lower critical magnetic field. We recall that:

$$H_{c1}(T) = H_{c1}^{em}(T) + H_{c1}^{core}(T), \quad (3.138)$$

where, after taking into account Eqs. (3.93), (3.69) and (3.70), we can write:

$$H_{c1}^{em}(T) \simeq H_{c1}^{em}(0) e^{-b' \left[ \frac{1}{\sqrt{1-T/T_c}} - 1 \right]}, \quad (3.139)$$

and

$$H_{c1}^{core}(T) \simeq H_{c1}^{core}(0) e^{-2b \left[ \frac{1}{\sqrt{1-T/T_c}} - 1 \right]}. \quad (3.140)$$

In Ref. [82] the lower critical fields in optimal doped YBCO ( $T_c \simeq 93.1K$ ) have been determined by magnetization measurements using a thin platelet crystal for external magnetic fields perpendicular to the  $CuO_2$  planes. In Fig. 8 we report the relevant experimental data extracted from Fig. 4 in Ref. [82]. As one can see, at temperature well below the critical temperature  $T_c$  the lower critical magnetic field behaves essentially with a linear temperature dependence. This behavior is qualitatively different from the characteristic saturation at low temperatures for conventional BCS superconductors. Moreover, it turned out that the observed  $H_{c1}(0)$  is considerably larger with respect to what one might expect within the Ginzburg-Landau theory. Indeed, the authors of Ref. [82] correctly argued that the core energy of an isolated Abrikosov vortex gives a non-negligible contribution to the lower critical magnetic field. We, now, show that this is indeed the case. To this end, we fitted the experimental data for the temperature dependence of the lower critical magnetic field, displayed in Fig. 8, to our theoretical results Eqs. (3.138) - (3.140). In the fitting procedure we found there is degeneracy in the parameters  $b$  and  $b'$ . So that we fixed  $b \simeq 0.193$ , as we did before, and taken  $b'$ ,  $T_c$ ,  $H_{c1}^{em}(0)$ , and  $H_{c1}^{core}(0)$  as free parameters. We found  $b' \simeq 1.7$ ,  $T_c \simeq 93.3$ ,  $H_{c1}^{em}(0) \simeq 710$  Oe, and  $H_{c1}^{core}(0) \simeq 350$  Oe. These results confirm that the contribution of the vortex core energy to the lower critical magnetic field is, indeed, sizable. The results of our fit are displayed in Fig. 8. Evidently, the agreement between theory and experiment is rather good. For completeness, we also show the different temperature behavior of  $H_{c1}^{em}(T)$  and  $H_{c1}^{core}(T)$ . Note that the almost linear dependence on the temperature in  $H_{c1}(T)$  is due to  $H_{c1}^{em}(T)$ , which dominates at low enough temperatures.

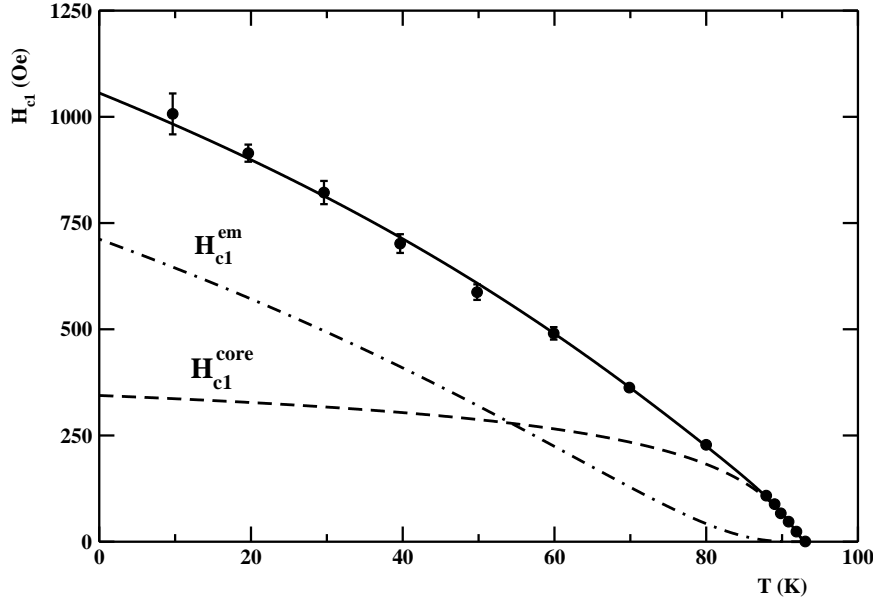


Figure 8: Temperature dependence of the lower critical magnetic field for YBCO. The data have been extracted from Fig. 4 of Ref. [82]. The solid line is the best fit of data to Eq. (3.138). Dashed and dot-dashed lines correspond to  $H_{c1}^{core}(T)$  and  $H_{c1}^{em}(T)$  respectively.

Next, we looked at the data for the lower critical magnetic field in underdoped YBCO. Ref. [83] reports the lower critical magnetic field for underdoped YBCO with critical temperatures varying between  $8.9\text{ K}$  and  $22\text{ K}$ . The critical fields were determined by measurements of magnetization in an applied magnetic field perpendicular to the copper-oxide planes. In Fig. 9, top panel, we display the temperature dependence of the lower critical magnetic field for underdoped YBCO with critical temperatures  $T_c \simeq 8.9\text{ K}$ ,  $13.7\text{ K}$ ,  $15.3\text{ K}$ ,  $17.6\text{ K}$ ,  $22.0\text{ K}$  respectively. The corresponding hole doping  $\delta$  can be inferred from the phenomenological relation Eq. (3.94). The hole doping level ranges from  $\delta \simeq 0.055$  up to  $\delta \simeq 0.064$ . The data have been extracted from Fig. 2 in Ref. [83]. Even in the highly underdoped region the lower critical magnetic field seems to vary linearly with temperature, at least for temperatures below  $\sim 0.6 T_c$ . In fact, the authors of Ref. [83], performing a linear fit in this temperature range, was able to extract  $H_{c1}(0)$ . They found that  $H_{c1}(0)$  was not a linear function of  $T_c$ . From the best fits they found a non-linear relation between the zero-temperature lower critical magnetic field versus the critical temperature,  $H_{c1}(0) = 0.366 T_c^{1.64 \pm 0.004}$  [83]. This last result looks puzzling. Indeed, in conventional BCS superconductors the effect of the vortex core energy is to slightly modify the logarithmic term  $\ln \kappa$  in  $H_{c1}(0)$ . Therefore, one expects that  $H_{c1}(0) \sim \lambda^{-2}(0) \sim n_s(0)$ . Since  $T_c \sim n_s(0)$  is the expected behavior if the critical temperature is governed only by phase fluctuations in two dimensions, then the above results would imply  $T_c \sim n_s(0)^{0.61}$ , that is inconsistent with the observed linear relation between the critical temperature and the superfluid condensate density [84, 85]. However, we already remarked that the vortex core energy contribution to the lower critical magnetic field cannot be neglected. On the other hand, it is evident that only the electromagnetic term  $H_{c1}^{em}(0)$  needs to scale with  $\lambda^{-2}(0)$ , while  $H_{c1}^{core}(0)$  is almost independent on the London penetration length. To determine  $H_{c1}^{em}(0)$  we fitted the available data to our Eqs. (3.138) - (3.140). We fixed the critical

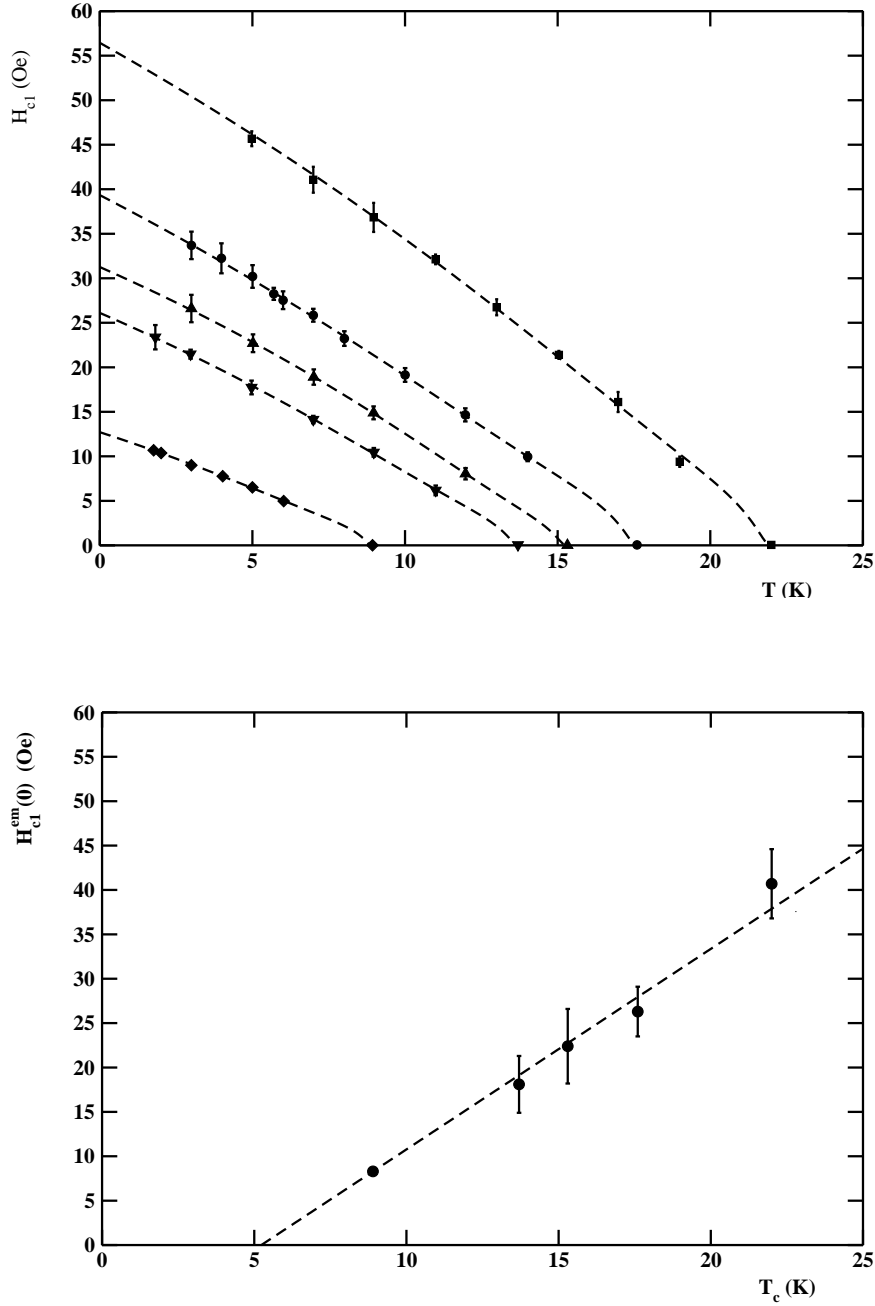


Figure 9: (Top) Lower critical magnetic field versus the temperature for highly underdoped YBCO. The corresponding hole doping fraction are  $\delta \simeq 0.055, 0.058, 0.059, 0.060, 0.064$  respectively. Data have been extracted from Fig. 2 in Ref. [83]. The dashed lines are the best fits of the experimental data to Eqs. (3.138) - (3.140). (Bottom) Fitted values of the zero-temperature lower critical magnetic field  $H_{cl}^{em}(0)$  versus the superconductive critical temperature. The statistical errors correspond to the 68 % confidence level. The dashed line is the best fit to the assumed linear relation between  $H_{cl}^{em}(0)$  versus  $T_c$ .

temperatures to the measured values and let  $H_{c1}^{em}(0)$ ,  $H_{c1}^{core}(0)$ , and  $b'$  be free fitting parameters. Moreover, as in previous analysis, we fixed  $b \simeq 0.193$ . In Fig. 9, bottom panel, the dashed lines are the best-fitted curves. We see that, in fact, the experimental data are in good agreement with our theoretical expectations. We found that the parameter  $b'$  did not showed statistically significant dependence on the hole doping  $\delta$ , at least in the rather narrow explored range of  $\delta$ ,  $b' \simeq 2.0$ . Even in this case, we confirm that the vortex core energy contribution to the lower critical magnetic field is not negligible. In fact, it turns out that  $H_{c1}^{core}(0) \sim 0.5 H_{c1}^{em}(0)$ . In Fig. 9, right panel, we report the best-fitted values for  $H_{c1}^{em}(0)$  as a function of the critical superconductive temperature. Remarkably, we found that, as expected,  $H_{c1}^{em}(0)$  scales linearly with  $T_c$ . The dashed line in Fig. 9, right panel, is the best fit straight line  $H_{c1}^{em}(0) \propto T_c$ . Note that the best-fit straight line does not extrapolate to the origin. This is due to the fact that the superconductive transition set in abruptly for  $\delta \gtrsim \delta_{min} \simeq 0.05$ , so that the critical temperature  $T_c$  is not strictly proportional to  $\delta$  for hole doping too close to  $\delta_{min}$ .

Finally, we turn on the temperature dependence of the upper critical magnetic field. The upper critical magnetic field is essential to identify the factor that limit the strength of superconductivity. However, in hole doped cuprates the direct measurement of the upper critical field is difficult for  $H_{c2}(0)$  can attain values as high as  $\sim 10^2 T$ . In Refs. [78, 86] it is suggested that the thermal conductivity can be used to directly detect the upper critical magnetic field in YBCO,  $YBa_2Cu_4O_8$  (Y124) and Tl-2201. In Fig. 10 we report the temperature dependence of  $H_{c2}$  for Y124 and YBCO in the pseudogap region. In our theory the temperature dependence of the upper critical magnetic field is given by Eq. (3.133), which it is useful to rewrite as:

$$H_{c2}(T) \simeq H_{c2}(0) e^{-b' \left[ \frac{1}{\sqrt{1-T/T_c}} - 1 \right]}. \quad (3.141)$$

Indeed, we have fitted the experimental data to Eq. (3.141). It turned out that our Eq. (3.141) allows to track the temperature dependence of the upper critical magnetic field in a satisfying way. The resulting best-fit curves are shown in Fig. 10 as dashed lines. We found  $T_c \simeq 84.5 K$ ,  $H_{c2}(0) \simeq 45.7 T$ ,  $b' \simeq 0.88$  for Y124 and  $T_c \simeq 62.1 K$ ,  $H_{c2}(0) \simeq 24.8 T$ ,  $b' \simeq 0.80$  for YBCO.

### 3.7 Temperature dependence of the critical current

The critical current density  $j_c$  represents a fundamental quantity for the superconductor applications. Usually, the maximum limit for the critical current is set by the depairing current. In high temperature superconductors the depairing critical current density is considerably higher than in conventional superconductors. For instance, in YBCO films one finds for the critical current density extrapolated to zero temperature the extraordinarily high value  $j_c(0) \sim 10 MA/cm^2$ <sup>11</sup>.

For zero applied field the critical current densities in high temperature superconductors are typically well described by the scaling law;

$$j_c(T) \simeq j_c(0) \left[ 1 - \frac{T}{T_c} \right]^\gamma. \quad (3.142)$$

---

<sup>11</sup>See Table 6.3 in Ref. [8]. Even though we are using cgs units, it is widespread consuetude to measure the current density in  $A/cm^2$ .

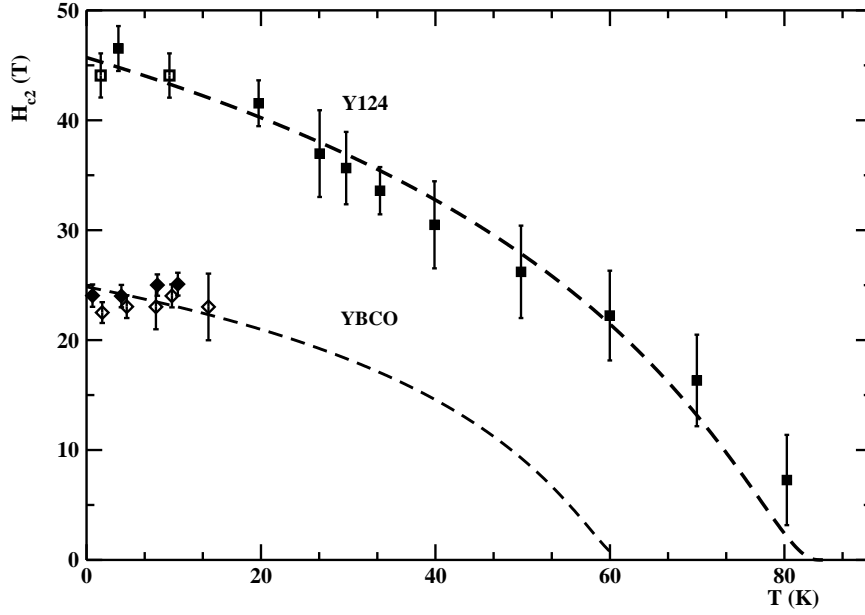


Figure 10: Temperature dependence of the upper critical magnetic field for two different compounds of cuprate superconductors. Full and open squares correspond to  $H_{c2}(T)$  for Y123 ( $\delta \simeq 0.14$ ). The data have been extracted from Fig. 3, panel b, in Ref. [78]. Full squares correspond roughly to the upper boundary of the vortex-liquid phase. Open squares correspond to the rapid drop in the longitudinal thermal conductivity versus the applied magnetic field. Full and open diamonds correspond to  $H_{c2}(T)$  for YBCO ( $\delta \simeq 0.11$ ). The data have been extracted from Fig. 1, panel a, in Ref. [86]. Full and open diamonds corresponds to  $H_{c2}(T)$  detected in the Hall and longitudinal thermal conductivity respectively. The dashed lines are the fits to Eq. (3.141) of the experimental measurements.

The values of the exponent are typically  $\gamma \simeq 1 - 2$ . According to the Ginzburg-Landau theory, the depairing current density depends on the London penetration length  $\lambda(T)$  and the Ginzburg-Landau coherence length  $\xi_{GL}(T)$ . Using the empirical temperature dependence of the two characteristic lengths one finds that near the critical temperature  $j_c(T)$  satisfies Eq. (3.142) with [87]

$$\gamma_{GL} \simeq \frac{3}{2} . \quad (3.143)$$

As we have already discussed, the electrical current density is given by Eq. (3.66):

$$\vec{j}_{em}(\vec{R}, T) = 2e n_s(T) \left[ \vec{v}_s(\vec{R}, T) - \frac{e}{m_h^* c} \vec{A}(\vec{R}) \right] , \quad (3.144)$$

where, we recall that  $\vec{h}(\vec{R}) = \nabla \times \vec{A}(\vec{R})$  and  $\langle \vec{h}(\vec{R}) \rangle_{\text{vol}} = \vec{B}(\vec{R})$ . For zero microscopic magnetic field  $\vec{h}(\vec{R})$  and using Eq. (3.53) and Eq. (3.54), we get:

$$\vec{j}_{em}(\vec{R}, T) \simeq 2e n_s(0) \vec{v}_s(\vec{R}, 0) e^{-b''} \left[ \frac{1}{\sqrt{1-T/T_c}} - 1 \right] , \quad b'' = b + b' . \quad (3.145)$$

The critical depairing current density is attained when  $v_s(0)$  equals the critical velocity  $v_c$  given by Eq. (3.109). Accordingly, we obtain the depairing critical current density:

$$j_c(T) \simeq j_c(0) e^{-b''} \left[ \frac{1}{\sqrt{1-T/T_c}} - 1 \right] , \quad j_c(0) = 2e n_s(0) v_c . \quad (3.146)$$

It is worthwhile to estimate the zero-temperature critical current density in terms of the model parameters. Explicitly, we have:

$$j_c(0) \simeq \frac{e}{c_0 a_0^2} \sqrt{\frac{\Delta_2(0)}{m_h^*}} \delta \left[ 1 - \left( \frac{\delta}{\delta^*} \right)^{1.5} \right]^{\frac{1}{2}} . \quad (3.147)$$

Using the numerical values of the parameters we obtain the estimate:

$$j_c(0) \simeq 2.84 \cdot 10^3 \frac{MA}{cm^2} \delta \left[ 1 - \left( \frac{\delta}{\delta^*} \right)^{1.5} \right]^{\frac{1}{2}} . \quad (3.148)$$

Eq. (3.148) shows that the zero-temperature critical current density has the same doping dependence as the upper critical magnetic field. In the pseudogap region  $\delta \lesssim \delta^*$  one finds  $j_c(0) \sim 10^2 \text{ MA/cm}^2$ , confirming that the critical depairing current density in hole doped cuprate superconductors can reach very high values.

To extract a quantitative estimate of the parameter  $b''$  we need to compare the temperature dependence of the critical current density to observations. In Fig. 11 we display the temperature dependence of the critical current density for the hole doped cuprate superconductors  $\text{Bi}_2\text{Sr}_2\text{CaCu}_2\text{O}_8$  (Bi-2212) and  $\text{Bi}_{1.8}\text{Pb}_{0.26}\text{Sr}_2\text{Ca}_2\text{Cu}_3\text{O}_{10+x}$  (Bi-2223). In the top panel, the data correspond to the average critical current density of Bi-2212 hollow cylinder ( $T_c = 92 \text{ K}$ ) and a tabular polycrystalline sample of Pb-doped Bi-2223 ( $T_c = 108 \text{ K}$ ) [88]. By fitting the data to the Ginzburg-Landau scaling law Eq. (3.142), the authors of Ref. [88] found  $j_c(0) \simeq 2.3 \cdot 10^4 \text{ A/cm}^2$ ,  $\gamma \simeq 2.5$  for Bi-2212, and  $j_c(0) \simeq 5.0 \cdot 10^3 \text{ A/cm}^2$ ,  $\gamma \simeq 1.5$  for Bi-2223. The resulting best-fit curves are displayed in Fig. 11 as dashed lines. We performed the fit of data to our Eq. (3.146). The resulting

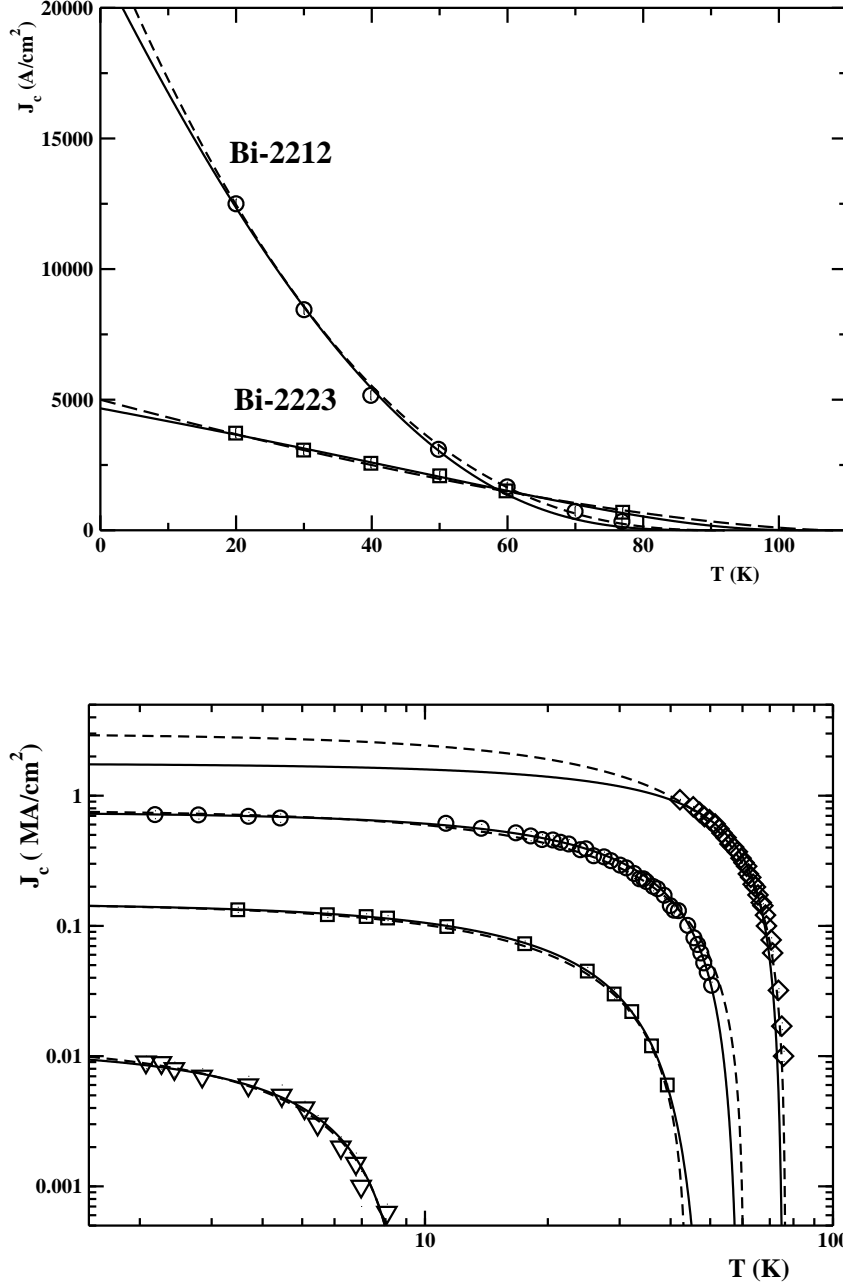


Figure 11: (Top) Critical current density versus the temperature for optimal doped Bi-2212 (open circles) and Bi-2223 (open squares). Data have been extracted from Fig. 3 in Ref. [88]. The dashed and solid lines are the fits to Eq. (3.142) and Eq. (3.146) respectively. (Bottom) Critical current density versus the temperature for Bi-2212 with different hole doping fraction in the pseudogap region. Data have been taken from Fig. 5, panel a, in Ref. [89]. The dashed and solid lines are the fits to Eq. (3.142) and Eq. (3.146) respectively.



fits, displayed as full lines, are practically indistinguishable from the Ginzburg-Landau power law. As concern the parameter  $b''$ , we found  $b'' \simeq 4.7, 2.3$  for Bi-2212 and Bi-2223 respectively, while for the zero-temperature critical current densities we found values consistent with the Ginzburg-Landau fits.

In the bottom panel of Fig. 11, we report the critical current density measurements for high quality Bi-2212 thin films for different hole doping fraction reported in Ref. [89]. The data correspond to critical temperature  $T_c \simeq 9\text{ K}, 44\text{ K}, 60.5\text{ K}, 76.5\text{ K}$ . The corresponding hole doped fraction  $\delta$  has been determined by using the phenomenological relationship Eq. (3.94) by assuming  $T_c^{max} \simeq 76.5\text{ K}$ . The authors of Ref. [89] found that the temperature dependence of the critical current density can be reproduced by the Ginzburg-Landau phenomenological power law with  $\gamma \simeq 1.5$  for all doping fraction  $\delta$ . Indeed, we have fitted the data to Eq. (3.142) with fixed  $\gamma = 1.5$  (see dashed lines in Fig. 11, bottom panel). On the other hand, the fits of the data to Eq. (3.146), displayed as solid lines in Fig. 11, bottom panel, track quite closely the Ginzburg-Landau phenomenological power law. Moreover, we found  $b'' \simeq 2.7$  almost independently on the doping fraction. It is worthwhile to observe that the best-fit parameter  $b''$  assumes quite different values for the same compound. In fact, for Bi-2212 hollow cylinder we obtained  $b'' \simeq 4.7$ , while for Bi-2212 thin films  $b'' \simeq 2.7$ . This can be easily understood within our model, for  $b''$  results from both the screening of the superfluid velocity and the depletion of the superconductive condensate fraction due to thermal proliferation of vortex-antivortex excitations. It is natural, therefore, to expect that this screening mechanism is more efficient in bulk material with respect to thin films. Note that this also explains naturally why critical current densities in superconducting films are much larger than in bulk material.

## 4 The Nodal Quasielectron Liquid

It is now well established that hole doped high temperature cuprate superconductors in the pseudogap region have an electron-like Fermi surface occupying a small fraction of the Brillouin zone. Indeed, angle resolved photoemission studies (see Refs. [90, 91, 92] and references therein) showed that low-energy excitations are characterized by Fermi arcs, namely truncate segments of a Fermi surface. Moreover, several recent studies (see Refs. [93, 94, 95, 96] and references therein) reported unambiguous identification of quantum oscillations in high magnetic fields. Interestingly enough, the measured low oscillation frequencies reveals a Fermi surface made of small pockets. In fact, from the Luttinger's theorem [97] and the Onsager relation [98, 99] between the frequency and the cross-sectional area of the orbit (see, for example, Refs. [100, 101, 102]), it results that the area of the pocket correspond to about a few percent of the first Brillouin zone area in sharp contrast to that of overdoped cuprates where the frequency corresponds to a large hole Fermi surface. In addition, there is convincing evidence of negative Hall and Seebeck effects which reveals that these pockets are electron-like rather than hole-like. Moreover, it turns out that these pockets are associated with states near the nodal region of the Brillouin zone. In I we provided some theoretical arguments to justify the occurrence of the nodal quasielectron liquid. Let us, briefly, recapitulate the main arguments presented in I, Sect. 4.4.

From the geometry of the  $\text{CuO}_2$  planes we argued:

$$\varphi(\vec{\rho}) = \varphi(\rho, \theta) = \varphi(\rho) \cdot \cos(2\theta), \quad (4.1)$$

where the coordinate axis are directed along the  $Cu - O$  bond directions. This is the most natural choice since the wavefunction is sizable along the  $Cu - O$  bonds and vanishes at  $\theta = \pm \frac{\pi}{4}$ . Let us consider the Fourier transform of the wavefunction:

$$\tilde{\varphi}(\vec{k}) = \int d\vec{\rho} \varphi(\rho, \theta) \exp(i\vec{k} \cdot \vec{\rho}) . \quad (4.2)$$

Assuming that the  $k_x, k_y$  axis are oriented along the copper-oxygen bond directions, one readily obtains:

$$\tilde{\varphi}(k, \theta_k) = \tilde{\varphi}(k) \cos(2\theta_k) \quad (4.3)$$

where:

$$\tilde{\varphi}(k) = -2\pi \int_0^\infty d\rho \rho \varphi(\rho) J_2(k\rho) . \quad (4.4)$$

We see, thus, that the Fourier transform of the wavefunction vanishes along the *nodal* directions:

$$\theta_k = \pm \frac{\pi}{4} , \quad (4.5)$$

while it is sizable along the *antinodal* directions:

$$\theta_k = 0 , \pm \frac{\pi}{2} . \quad (4.6)$$

Even though the pair wavefunction vanishes along the nodal directions  $k_x = \pm k_y$  ( $\theta_k = \pm \frac{\pi}{4}$ ), there are not nodal low-lying hole excitations. This is due to the fact that the pairing of the holes is in the real space and not in momentum space [103]. On the other hand, we may freely perform rotations of the pairs without spending energy since this modify only the phase of pair wavefunction. The rigid rotations of pairs is equivalent to hopping of electrons according to the hopping term in the Hamiltonian Eq. (1.1):

$$\hat{H}_0^{(e)} = -t \sum_{\langle i,j \rangle, \sigma} \left[ \hat{c}_{i,\sigma}^\dagger \hat{c}_{j,\sigma} + \hat{c}_{j,\sigma}^\dagger \hat{c}_{i,\sigma} \right] . \quad (4.7)$$

We may diagonalize this Hamiltonian obtaining:

$$\hat{H}_0^{(e)} = \sum_{\vec{k}, \sigma} \varepsilon_{\vec{k}}^{(e)} \hat{\psi}_e^\dagger(\vec{k}, \sigma) \hat{\psi}_e(\vec{k}, \sigma) . \quad (4.8)$$

In the small- $k$  limit we have:

$$\varepsilon_{\vec{k}}^{(e)} \simeq \frac{\hbar^2 \vec{k}^2}{2m_e^*} , \quad (4.9)$$

where:

$$m_e^* = \frac{\hbar^2}{2t a_0^2} \simeq 2.17 m_e . \quad (4.10)$$

Since there are  $1 - \delta$  electrons per  $Cu$  atoms, from the Hamiltonian Eq. (4.8) we may determine the electron Fermi energy:

$$\varepsilon_F^{(e)} = \frac{\hbar^2 (\vec{k}_F^{(e)})^2}{2m_e^*} , \quad a_0 k_F^{(e)} \simeq \sqrt{2\pi(1 - \delta)} . \quad (4.11)$$

At first glance, one expects that the quasielectrons fill in momentum space the circle

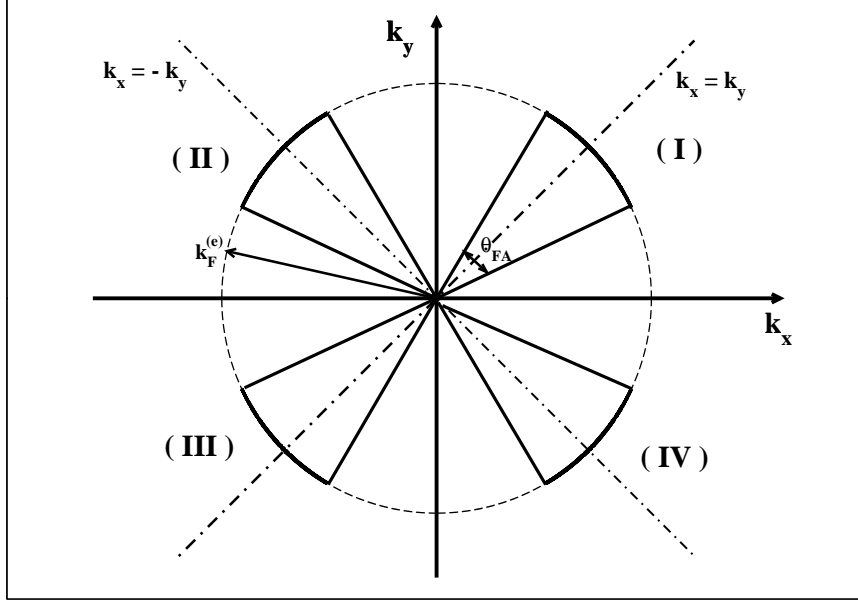


Figure 12: The quasielectron Fermi sector and Fermi arcs in the first Brillouin zone. For later convenience, the we have labelled the four quadrant of the Brillouin zone.

with radius  $k_F^{(e)}$  (the electron Fermi surface). However, one should keep in mind that the hopping of electrons is possible thanks to the paired holes. Since in momentum space the wavefunction of a given pair is spread over a region around  $k \sim \frac{1}{\xi_0}$ , we see that the wavefunction of quasielectrons is likewise localized on a region in  $k$ -space around  $\frac{1}{\xi_0}$ . Thus, the quasielectrons do not have the needed coherence to propagate over large distances with a well defined momentum. However, this argument does not apply along the nodal directions where the momentum-space hole pair wavefunction vanishes. Therefore we are led to the conclusion that there are coherent quasielectrons that fill small circular sectors of the electron Fermi circle around the nodal directions  $k_x = \pm k_y$ . Thanks to the rotational symmetry, we have four circular sectors with the same area. Since the number of coherent quasielectrons is determined by the doping fraction of holes (assuming that all the holes are paired), we obtain (see Fig. 12):

$$\frac{\delta}{a_0^2} \simeq \frac{4 \times 2}{(2\pi)^2} \frac{1}{2} (k_F^{(e)})^2 \theta_{FA} , \quad (4.12)$$

namely

$$\theta_{FA} \simeq \frac{\pi}{2} \frac{\delta}{1 - \delta} . \quad (4.13)$$

We see, thus, that the Fermi surface is made by four Fermi arcs in qualitative agreement with the angle resolved photoemission data. Moreover, the area of the Fermi sector with respect to the area of the Fermi circle in overdoped region turns out to be:

$$\frac{\mathcal{A}_{FA}}{\mathcal{A}_{overdoped}} \simeq \frac{1}{4} \frac{\delta}{1 + \delta} . \quad (4.14)$$

For the typical value of hole doping fraction  $\delta \simeq 0.1$ , we infer from Eq. (4.14) that, indeed,  $\mathcal{A}_{FA}$  is about 2.3 % of the first Brillouin zone area in the overdoped region, in satisfying

agreement with quantum oscillation experiments.

It is useful to emphasize that the nodal quasielectron low-lying excitations are basically controlled by the pseudogap. Therefore, we expect that these excitations would be present up to the pseudogap temperature  $T^*$ . However, our previous arguments rely on the possibility to freely vary the phase of the hole pair wavefunction without spending energy. Therefore, we see that nodal quasielectron excitations are present only in the disordered phase of the pair condensate. Finally, we must admit that the discussion on the origin of the nodal quasielectron is somewhat qualitative and cannot be considered a truly microscopic explanation. However, in the spirit of our approach, the roughness of these arguments are nevertheless corroborated by the clear experimental evidence of the nodal quasielectron liquid in the pseudogap region of hole doped cuprate superconductors.

## 4.1 The nodal gap

The most extensive investigation of excitation gaps in high temperature cuprate superconductors has been done by angle resolved photoemission spectroscopy (ARPES) [90, 91, 92]. This technique generally gives informations on the electronic structure of a material. In the high temperature cuprate superconductors, due to the quasi-two dimensionality of the electronic structure, ARPES studies permit to unambiguously determine the momentum of the initial state from the measured final state momentum, since the component parallel to the surface is conserved in photoemission (note that the photon momentum can be neglected at the low photon energies typically used in experiments). From the detailed momentum dependence of the excitation gap along the Fermi surface contour, these studies suggested the coexistence of two distinct spectral gap components, namely the pseudogap and another gap which was identified with the superconductive gap [104, 105, 106, 107, 108, 109, 110, 111, 112, 113] (see, also, Ref. [15] and references therein). There are two main motivations which led to identify the second gap detected in ARPES experiments with the superconductive gap. First, the gap were sizable in the nodal regions in momentum space. Second, the gap closes at the critical temperature  $T_c$ . Therefore, it was natural to consider the gap as the d-wave BCS gap. However, this point of view is in striking contrast with the substantial experimental evidence that the superconductive transition is driven by the B-K-T transition, for in this case there is not any superconductive gap to play with. In addition, we have already seen that the temperature dependence of the London penetration length within the weak coupling d-wave BCS theory is in undeniable disagreement with the experimental data. Indeed, now we shall show that the gap detected in ARPES studies, which will be referred to as nodal gap, is not the superconductive gap but, nevertheless, it is related intimately to the low-lying excitations of the hole pair superfluid condensate.

In ARPES experiments the superfluid condensate is excited by the incoming photons. We saw in Sect. 3.1 that the low-lying condensate excitations are rotons which behave like elementary quasiparticle with mass  $2m_h^*$  and charge  $2e$ . Since the in-plane photon momentum is negligible, naively one expects that the lowest energy excitations would be two rotons with opposite superfluid velocity. However, we known that  $\varepsilon_{roton} \sim \Delta_2$ , so that these kind of configurations are lying at very high energies. Moreover, the roton-antiroton pairs do not give rise directly to photoelectrons and, therefore, they can be hardly detected in ARPES experiments. On the other hand, if we take into account that in the vortex core region the condensate is phase disordered, then we see that, according to the

discussion in Sect. 4, a moving roton can excite nodal quasielectrons in such a way that the roton momentum can be compensated. In other words, we are led to consider condensate configurations corresponding to a moving roton and a few of nodal quasielectrons with opposite velocities. We have seen that the energy of the nodal quasielectrons is:

$$\varepsilon_{\vec{k}}^{(e)} \simeq \frac{\hbar^2 \vec{k}^2}{2m_e^*} . \quad (4.15)$$

Eq. (4.15) is relevant in the superfluid condensate rest frame. If the condensate has velocity  $\vec{v}_s$ , then, following the well-known Landau's arguments (see, eg, Ref. [114]), we have:

$$\varepsilon_{\vec{k}}^{(e)} \simeq \frac{1}{2} m_e^* (\vec{v}_e + \vec{v}_s)^2 \simeq \frac{\hbar^2 \vec{k}^2}{2m_e^*} + \hbar \vec{k} \cdot \vec{v}_s + \frac{1}{2} m_e^* v_s^2 . \quad (4.16)$$

The low-lying excitation spectrum of the nodal quasielectrons is determined by:

$$\varepsilon_{\vec{k}}^{(e)} - \varepsilon_F^{(e)} \geq 0 . \quad (4.17)$$

Combining Eqs. (4.16) and (4.17), and observing that  $\cos \theta_{\vec{k}\vec{v}_s} \simeq -1$  since the total momentum must vanish, we obtain readily:

$$\varepsilon_{\vec{k}}^{(e)} - \varepsilon_F^{(e)} \gtrsim \hbar k v_s - \frac{1}{2} m_e^* v_s^2 . \quad (4.18)$$

For  $k \approx k_F^{(e)}$  and using Eq. (3.43) one can check that the second term on the right hand side of Eq. (4.18) is negligible with respect to the first term. Therefore we obtain that near the Fermi surface the nodal quasielectron spectrum is gapped:

$$\varepsilon_{\vec{k}}^{(e)} - \varepsilon_F^{(e)} \gtrsim \hbar k v_s , \quad k \gtrsim k_F^{(e)} . \quad (4.19)$$

This allow to introduce the nodal gap:

$$\Delta_{nodal} \simeq \hbar k_F^{(e)} v_s . \quad (4.20)$$

Evidently, the nodal gap determines the energy gap size at the Fermi surface. Nevertheless, from Eq. (4.19) we see that the quasiparticle excitation energy dispersion is linear in the wavenumber  $k$  with slope  $\hbar v_s$ . The temperature dependence of the nodal gap is mainly due to the thermal screening of the superfluid velocity as implied by Eq. (3.53):

$$\Delta_{nodal}(T) \simeq \Delta_{nodal}(0) e^{-b \left[ \frac{1}{\sqrt{1-T/T_c}} - 1 \right]} , \quad T \lesssim T_c , \quad (4.21)$$

where:

$$\Delta_{nodal}(0) \simeq \hbar k_F^{(e)} v_s(0) . \quad (4.22)$$

Before comparing our results to experimental data, it is useful to determine the doping dependence of the nodal gap. This can be easily accomplished using our previous results on the superfluid velocity of rotons, Eq. (3.43), and on the Fermi wavenumber of nodal quasielectrons, Eq. (4.11):

$$\Delta_{nodal}(0) \simeq \frac{\hbar}{a_0} \sqrt{2\pi(1-\delta)} \frac{\hbar}{2m_h^* d_0} \frac{2\pi}{d_0} \simeq \pi^{\frac{3}{2}} \frac{\hbar^2}{m_h^* a_0^2} \sqrt{\delta(1-\delta)} . \quad (4.23)$$

A few comments are in order. Firstly, the nodal gap is sizable in the nodal regions in momentum space  $k_x \simeq \pm k_y$ , for the nodal quasielectron excitations are present only there. The doping dependence of the nodal gap is quite different from the pseudogap and the critical temperature  $T_c$ . In fact, the pseudogap decreases with increasing doping according to Eq. (2.14), while the critical temperature scales roughly linearly with the hole doping  $\delta$  (see Eq. (2.19)). This has interesting consequences. In fact, let us consider the ratio between the nodal gap and the critical temperature:

$$\frac{\Delta_{nodal}(0)}{k_B T_c} \sim \sqrt{\frac{1-\delta}{\delta}}. \quad (4.24)$$

If one identifies the nodal gap with the weak coupling d-wave BCS gap, then this ratio should be  $\sim 2.14$  (see Eq. (A.16)) independently on the hole doping. In contrast, Eq. (4.24) implies that that ratio is doping dependent and it increases roughly as  $\sim 1/\sqrt{\delta}$  in the highly underdoped region, in qualitative agreement with observations.

It should be evident that our interpretation of the nodal gap being highly unconventional needs to be compared both qualitative and quantitatively with observations. We attempted several checks to test both the dependence on temperature and on hole doping of the nodal gap by comparing to available ARPES studies in literature. Here we present some illustrative examples of such comparisons. In Ref. [107] it was investigated the doping dependence of the pseudogap and nodal gap in high-quality single crystals of LSCO by angle resolved photoemission spectroscopy. The hole doping fractions were  $\delta = 0.03, 0.07, 0.15$ . For  $\delta = 0.07, 0.15$  the critical temperatures were  $T_c \simeq 14 K, 39 K$  respectively. The sample with hole doping  $\delta = 0.03$  was not superconducting. In Fig. 13, top panel, we display the doping dependence of the pseudogap  $\Delta_2(\delta)$  and the nodal gap  $\Delta_{nodal}(\delta)$ . The data have been extracted from Fig. 2, panel c, in Ref. [107]. As regard the pseudogap, we compare the data to Eq. (2.14) by taking  $\Delta_2(0) \simeq 60 meV$ . Note that this value for  $\Delta_2(0)$  is in reasonable agreement with the estimate obtained with the numerical values of the model parameters. The doping dependence of the nodal gap is given by Eq. (4.23). Accordingly, in Fig. 13, top panel, we display

$$\Delta_{nodal} \simeq 40 meV \sqrt{\delta(1-\delta)}, \quad \delta \gtrsim \delta_{min} \simeq 0.05, \quad (4.25)$$

where the constant has been fixed to match the data. For  $\delta < \delta_{min}$  the nodal gap vanishes since, as we said, it is related to the low-lying excitations of the superfluid condensate. We see that the data are in satisfying agreement with our theoretical expectations. Nevertheless, it must be mentioned that the estimate of the constant in Eq. (4.25) with the model parameters gave a value higher by about one order of magnitude. This could be due to the fact that in LSCO the  $T_c^{max} \sim 40 K$ , while in our model  $T_c^{max} \sim 100 K$  (see Fig. 2). Moreover, the data for the nodal gap are taken at finite temperature where the gaps are somewhat smaller with respect to the zero-temperature values.

We have seen that the nodal quasielectron excitation energy dispersion is linear in the wavenumber  $k$  with slope  $\hbar v_s$ . Following the practice common among experimental physicists this slope is called nodal Fermi velocity  $v_F$ . Note that  $v_F$  does not have the dimension of a velocity but its dimension is energy  $\times$  length. According to our pervious discussion, we find that the nodal Fermi velocity depends on hole doping according to:

$$v_F \simeq \hbar v_s \simeq \frac{\pi}{\sqrt{2}} \frac{\hbar^2}{m_h^* a_0} \sqrt{\delta}. \quad (4.26)$$

In fact, a doping dependent nodal Fermi velocity has been revealed by high-resolution ARPES [115]. In Fig. 13, bottom panel, we report the doping dependence of the nodal Fermi velocity obtained in Ref. [115] by high-resolution ARPES spectra for Bi-2212 with doping in the range  $0.076 < \delta < 0.14$ . The nodal Fermi velocity was obtained from the slope of the excitation energy spectra in the range  $0 - 7 \text{ meV}$ . The data for  $v_F$  are contrasted to Eq. (4.26). More precisely, we compare the data with:

$$v_F \simeq 4.22 \text{ meV } \text{\AA} \sqrt{\delta}. \quad (4.27)$$

Even in this case, we found that the estimate of the constant with the model parameters produces a value about a factor  $\sim 5$  smaller than in Eq. (4.27). Nevertheless, we see that the puzzling doping dependence of the nodal Fermi velocity is in fair agreement with our model calculations. Interestingly, the authors of Ref. [115] reported that to fully characterize the ARPES spectra it was needed two different velocities. In fact, they introduced the nodal Fermi velocity  $v_{mid}$  defined by the linear fits of the spectra in the energy range  $30 - 40 \text{ meV}$ . Looking at Fig. 13, bottom panel, it is evident that  $v_{mid}$  does not display a strong doping dependence, while  $v_F$  has a pronounced dependence on doping. Since the nodal Fermi velocity is extracted from the excitation spectrum in an energy range well above the nodal gap, we suggest that the high-energy spectrum is due to unconstrained nodal quasielectrons. If this is the case, then the relevant Fermi velocity would be:

$$v_{mid} \simeq \frac{\hbar^2 k_F}{m_e^*} \simeq \frac{\hbar^2}{m_e^* a_0} \sqrt{1 - \delta}. \quad (4.28)$$

In fact, in Fig. 13, bottom panel, we see that the data can be accounted for quite accurately by:

$$v_{mid} \simeq 1.90 \text{ meV } \text{\AA} \sqrt{\delta}. \quad (4.29)$$

We would like to note that, this time, the estimate of the constant with the model parameters produces a value in fair agreement with the value in Eq. (4.29).

We turn, now, on the temperature dependence of the nodal gap. In Ref. [116] it was presented spectroscopic studies of the cuprate superconductor compound Bi-2223 in the optimal doped region. These authors employed both scanning tunneling spectroscopy [117] and Andreev-Saint-James reflection spectroscopy [118]. The tunneling spectroscopy, that in principle is sensitive to any gap in the excitation spectra, detected a rather large gap which, however, did not reveal any appreciable temperature dependence. On the contrary, it was reported a qualitatively different temperature dependence of the energy gap observed in superconductor-normal-superconductor junctions that unequivocally exhibited Andreev reflections. Remarkably, the data for the temperature dependence of the gap detected in Andreev spectroscopy were in reasonable agreement with the phenomenological BCS-like relation:

$$\frac{\Delta_{nodal}(T)}{\Delta_{nodal}(0)} \simeq \sqrt{1 - \left(\frac{T}{T_c}\right)^4}. \quad (4.30)$$

Indeed, in Fig. 14 we report the temperature dependence of the energy gap detected with the Andreev spectroscopy. The data has been extracted from Fig. 2 of Ref. [116]. We compare the data with the phenomenological relation Eq. (4.30) (dot-dashed line). We see, in fact, that this relation accounts quite well the temperature dependence of the energy gap. On the other hand, the temperature behavior of the the weak-coupling BCS

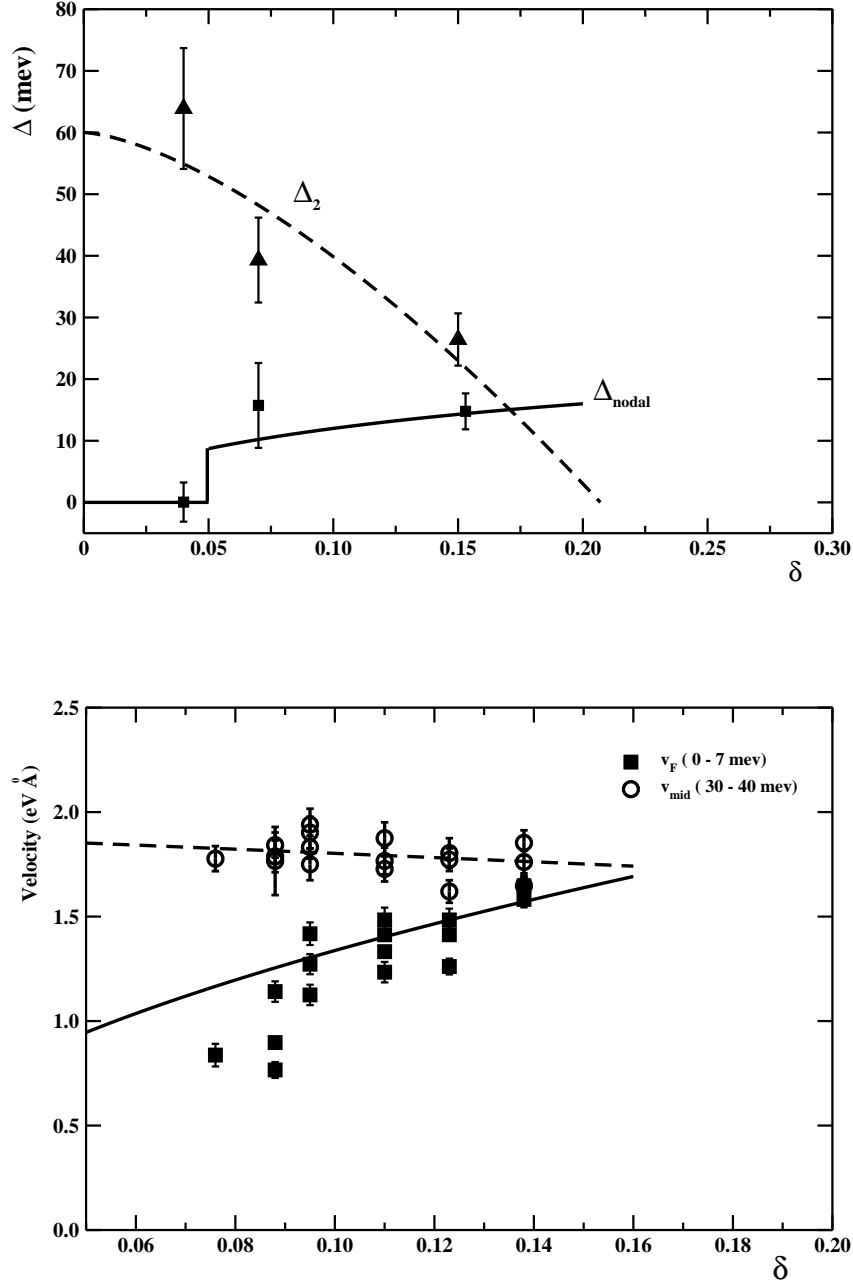


Figure 13: (Top) Doping dependence of the pseudogap and nodal gap. The data refer to lightly to optimally doped LSCO and have been extracted from Fig. 2, panel c, in Ref. [107]. The solid line is Eq. (4.25), the dashed line is Eq. (2.14) assuming  $\Delta_2(0) \simeq 60 \text{ meV}$ . (Bottom) Doping dependence of the low- and high-energy nodal Fermi velocities extracted from momentum distribution analysis in underdoped Bi-2212. The data have been taken from Fig. 3, panel a) of Ref. [115]. The solid and dashed lines are our Eq. (4.27) and Eq. (4.29) respectively.



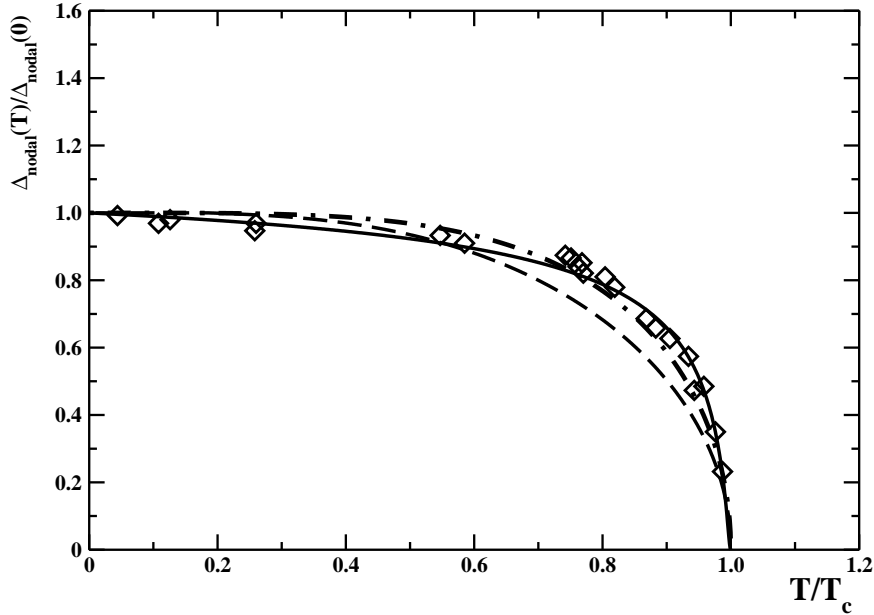


Figure 14: Temperature dependence of the nodal gap for Bi-2223 as extracted from Andreev reflection spectroscopy. The data have been taken from Fig. 2 of Ref. [116]. The solid line is our Eq. (4.21) with  $b \simeq 0.193$ , the dashed line is the weak coupling d-wave BCS gap, Eq. (A.33), and the dot-dashed line is the phenomenological relation, Eq. (4.30).

gap (see Eq. (A.33) in Appendix A) is seen to deviate from the data. In fact, the BCS d-wave gap underestimates the gap for  $T/T_c \gtrsim 0.7$  (see the dashed line in Fig. 14).

Our interpretation of the puzzling results presented in Ref. [116] is as follows. The tunnel data are sensitive to the pseudogap, but cannot detect easily the nodal gap since one does not have excitations of the condensate in tunneling spectroscopy experiments. On the other hand, Andreev reflection spectroscopy is sensitive to the low-lying excitations. This implies that the Andreev gap must be identify with the nodal gap. According to our theory, the pseudogap does not display a pronounced temperature dependence for temperatures within the critical temperature since  $T_c < T^*$ . Moreover, the temperature dependence of the nodal gap is given by Eq. (4.21). Accordingly, we fitted the Andreev gap data to our Eq. (4.21) leaving  $b$  as free fitting parameter. Remarkably, we found a very good fit with  $b \simeq 0.193$ . Indeed, the fitted curve, displayed as solid line in Fig. 14, follows quite closely the phenomenological law Eq. (4.30). Nevertheless, it seems that our best fit compare with the data slightly better than Eq. (4.30).

We, also, tried several comparisons between Eq. (4.21) and more recent data in the literature. Here, we merely present our results for two different ARPES studies of the nodal energy gap. In Ref. [119] it was presented the temperature dependence of the nodal energy gap extracted from spectra taken by angle resolved photoemission spectroscopy for underdoped Bi-2212 ( $T_c \simeq 92\text{ K}$ ). In Fig. 15, top panel, we display the nodal energy gap versus the temperature. The data correspond to those in Ref. [119], Fig. 2, panel d. We compare the data to the weak coupling d-wave BCS relation by taking  $\Delta_{\text{nodal}}(T = 0) \simeq 14.4\text{ meV}$  and  $T_c \simeq 92.0\text{ K}$ . Fig. 15 show that the BCS relation is in fair agreement with the data mainly due to the large experimental uncertainties. However, one sees that Eq. (4.21), with  $b \simeq 0.193$ , compares better to the data. Finally, we considered the angle resolved photoemission spectroscopy study for the same compound Bi-2212 with a slightly differ-

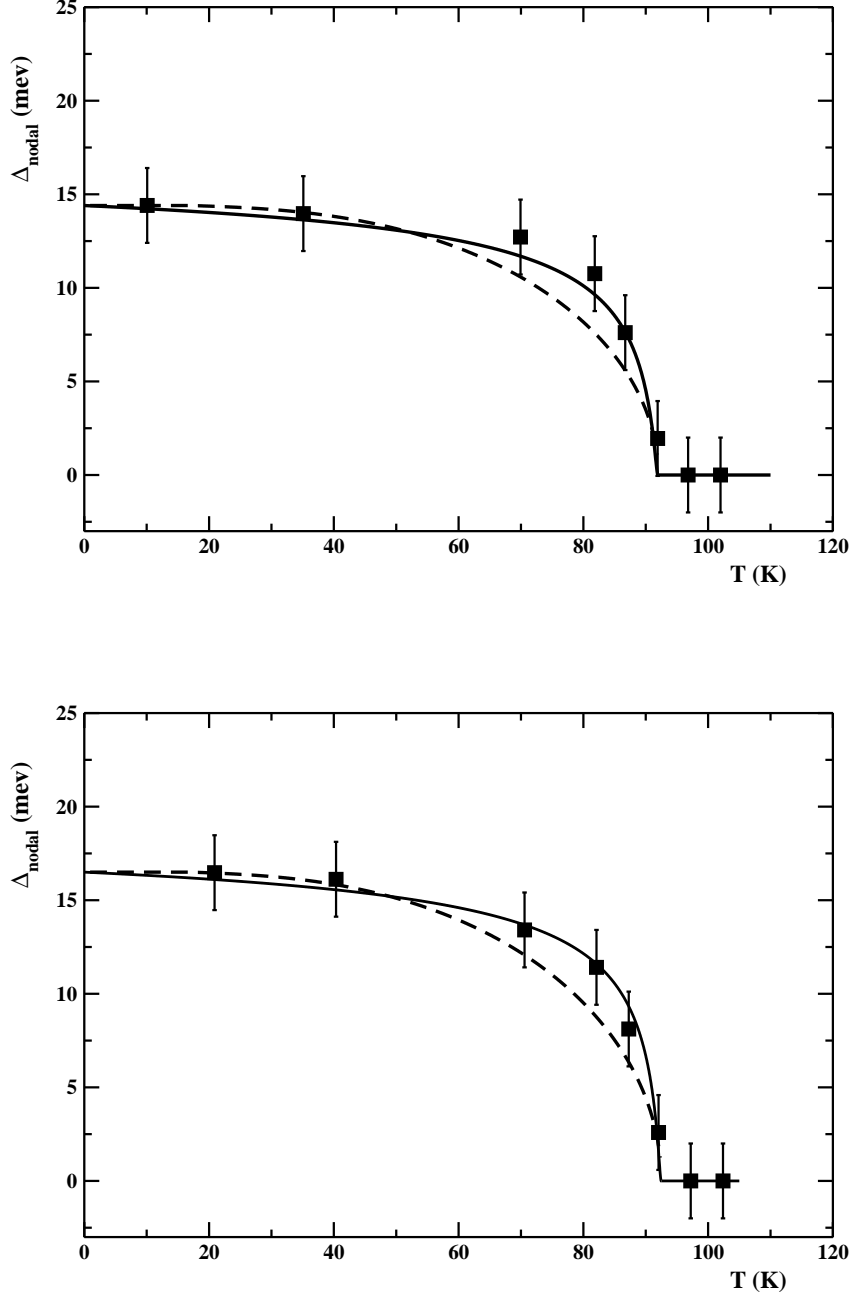


Figure 15: (Top) Temperature dependence of the nodal gap for Bi-2212 as extracted from angle resolved photoemission spectroscopy. The data have been taken from Fig. 2, panel d, in Ref. [119]. The solid and dashed curves are Eq. (4.21) with  $b \simeq 0.193$  and the BCS d-wave gap respectively, assuming  $\Delta_{\text{nodal}}(T = 0) \simeq 14.4$  meV and  $T_c \simeq 92.0$  K. (Bottom) Temperature dependence of the nodal gap for Bi-2212 as extracted from angle resolved photoemission spectroscopy. The data have been taken from Fig. 7, panel d, in Ref. [120]. The solid and dashed curves are Eq. (4.21) with  $b \simeq 0.193$  and the BCS d-wave gap respectively assuming  $\Delta_{\text{nodal}}(T = 0) \simeq 16.5$  meV and  $T_c \simeq 92.5$  K.

ent critical temperature ( $T_c \simeq 92.5 K$ ). The data for the nodal energy gap, displayed in Fig. 15, bottom panel, have been extracted from Fig. 7, panel d, in Ref. [120]. Again, we see that our nodal gap Eq. (4.21) compares moderately better than the BCS d-wave gap.

## 4.2 Thermodynamics of the nodal quasielectron liquid

We intend to calculate the thermal properties of the nodal quasielectron liquid. Throughout this Section we shall take the nodal liquid as a free and independent gas of quasiparticles. Here, we are explicitly neglecting corrections due to Coulomb electron-electron or electron-ion interactions. The effects of the interactions with the lattice ions will be discussed in Sect. 5. Coulomb interactions are the main mechanism for electron-electron Umklapp scatterings. These processes are relevant mainly in transport phenomena which, however, are beyond the aims of the present paper.

When the temperature is not zero the thermal distribution of nodal quasielectron is the Fermi-Dirac distribution:

$$f(\varepsilon_{\vec{k}}^{(e)}) = \frac{1}{e^{\frac{\varepsilon_{\vec{k}}^{(e)} - \mu^{(e)}(T)}{k_B T}} + 1} , \quad (4.31)$$

where  $\mu^{(e)}(T)$  is the quasielectron chemical potential. At zero temperature  $\mu^{(e)}(0) = \varepsilon_F^{(e)}$ . The temperature corrections to the quasielectron chemical potential can be obtained from:

$$n^{(e)} \simeq \frac{\delta}{a_0^2} = 2 \int_{FA} \frac{d\vec{k}}{(2\pi)^2} \frac{1}{e^{\frac{\varepsilon_{\vec{k}}^{(e)} - \mu^{(e)}(T)}{k_B T}} + 1} , \quad (4.32)$$

where the angular integration is performed over the four Fermi arcs (FA), see Fig. 12. Introducing the density of state per spin at the Fermi energy:

$$\mathcal{N}(0) \equiv \int_{FA} \frac{d\vec{k}}{(2\pi)^2} \delta[\varepsilon_{\vec{k}}^{(e)} - \varepsilon_F^{(e)}] \simeq \frac{m_e^*}{\pi^2 \hbar^2} \theta_{FA} , \quad (4.33)$$

Eq. (4.32) can be rewritten as:

$$n^{(e)} = 2 \mathcal{N}(0) \int_0^\infty d\varepsilon \frac{1}{e^{\frac{\varepsilon - \mu^{(e)}(T)}{k_B T}} + 1} . \quad (4.34)$$

It is easy to check that:

$$\int_0^\infty d\varepsilon \frac{1}{e^{\frac{\varepsilon - \mu^{(e)}(T)}{k_B T}} + 1} = \mu^{(e)}(T) + \mathcal{O}(e^{-\frac{\mu^{(e)}(T)}{k_B T}}) . \quad (4.35)$$

Therefore, neglecting the exponentially small thermal corrections, we find  $\mu^{(e)}(T) \simeq \varepsilon_F^{(e)}$ . We are interested in the calculation of the electronic contribution to the specific heat. Actually, experimentally one generally measures the specific heat at constant pressure. However, it is known that for temperatures such that  $k_B T \ll \varepsilon_F^{(e)}$  the specific heat at constant pressure is practically coincident with the specific heat at constant volume. The quasielectron contribution to the constant-volume specific heat is:

$$c^{(e)}(T) = \frac{\partial \mathbf{u}^{(e)}(T)}{\partial T} , \quad (4.36)$$

$u^{(e)}(T)$  being the electronic energy density:

$$u^{(e)}(T) = 2 \int_{FA} \frac{d\vec{k}}{(2\pi)^2} \varepsilon_{\vec{k}}^{(e)} \frac{1}{e^{\frac{\varepsilon_{\vec{k}}^{(e)} - \mu^{(e)}(T)}{k_B T}} + 1} . \quad (4.37)$$

Rewriting Eq. (4.37) as:

$$u^{(e)}(T) = 2 \mathcal{N}(0) \int_0^\infty d\varepsilon \varepsilon \frac{1}{e^{\frac{\varepsilon - \mu^{(e)}(T)}{k_B T}} + 1} , \quad (4.38)$$

and taking into account that [121]

$$\int_0^\infty d\xi \frac{\xi}{e^\xi + 1} = \frac{\pi^2}{12} , \quad (4.39)$$

we readily obtain:

$$u^{(e)}(T) \simeq \mathcal{N}(0) (\varepsilon_F^{(e)})^2 \left[ 1 + \frac{\pi^2}{3} \left( \frac{k_B T}{\varepsilon_F^{(e)}} \right)^2 \right] . \quad (4.40)$$

Whereupon we obtain for the specific heat:

$$c^{(e)}(T) \simeq \frac{2}{3} \pi^2 \mathcal{N}(0) k_B^2 T . \quad (4.41)$$

To compare with experiments it is convenient to introduce the molar specific heat:

$$c_m^{(e)}(T) = a_0^2 N_A c^{(e)}(T) . \quad (4.42)$$

Evidently we can write:

$$c_m^{(e)}(T) = \gamma_S T , \quad (4.43)$$

where the Sommerfeld coefficient is:

$$\gamma_S \simeq \frac{\delta}{1 - \delta} \frac{\pi}{3} \frac{m_e^* a_0^2}{\hbar^2} N_A k_B^2 . \quad (4.44)$$

Using the numerical values of the microscopic parameters, we find the estimate (in MKS units):

$$\gamma_S \simeq \frac{\delta}{1 - \delta} 6.82 \frac{mJ}{mol K^2} . \quad (4.45)$$

This last equation implies that in the pseudogap region  $\delta \sim 0.1$ ,  $\gamma_S \sim 1.0 mJ/mol K^2$ . In the following Section we will deal with the effects of an applied magnetic field on the low-temperature specific heat in hole doped cuprate superconductors in the pseudogap region. In fact, there are some controversial experimental evidences for a field-induced Sommerfeld coefficient in the electronic specific heat (see the general survey in Refs. [58, 59]). At low temperatures the external magnetic field penetrates into the superconductor with an array of Abrikosov vortices. Long time ago, it was pointed out [122] that in d-wave superconductors, due to the line nodes of the superconducting gap, there is a field-induced Sommerfeld coefficient in the electronic specific heat with Sommerfeld coefficient  $\gamma_S(H) \sim$

$\sqrt{H}$ . Basically, this effect is due to the supercurrent circulating around an Abrikosov vortex which shift the quasiparticle energy by Doppler effect modifying, thereby, the density of states at the Fermi energy. In our approach, the low-lying excitations are the nodal quasielectrons which can be excited in the core of the vortex where the pair condensate is phase disordered. Following Ref. [122] we may employ the semiclassical approach where the momentum and position of quasiparticles are commuting variables. The effects of the supercurrent circulating around a vortex is accounted for by a Doppler shift of the quasiparticle energy according to Eq. (4.16). Thus, for the nodal quasielectrons we have:

$$\varepsilon_{\vec{k}}(\vec{R}) \simeq \frac{\hbar^2 \vec{k}^2}{2 m_e^*} + \hbar \vec{k} \cdot \vec{v}_s(\vec{R}) , \quad (4.46)$$

where  $\vec{v}_s(\vec{R})$  is the superfluid velocity around an Abrikosov vortex. Adopting polar coordinates, we have:

$$\vec{v}_s(\vec{R}) = \vec{v}_s(R, \theta_R) \simeq \frac{\hbar}{4 m_h^*} \frac{\hat{\theta}_R}{R} . \quad (4.47)$$

The Doppler shift Eq. (4.47) could modify the density of state. To see this, we need to evaluate the density of state per spin at the Fermi surface averaged over the vortex:

$$< \mathcal{N}(0) >_{vor} \equiv \int \frac{d\vec{k}}{(2\pi)^2} \int d\vec{R} \delta \left[ \varepsilon_{\vec{k}}(\vec{R}) - \varepsilon_F^{(e)} \right] \frac{1}{\pi d_V^2} , \quad (4.48)$$

where  $d_V$  is the average distance between vortices. Eq. (4.48) refers to an isolated Abrikosov vortex. However, since the high temperature superconductors are extreme type-II superconductors and  $d_V \gg \xi_V \simeq d_0$ , the dilute vortex approximation should be reliable. Now, we observe that:

$$\begin{aligned} \varepsilon_{\vec{k}}(\vec{R}) - \varepsilon_F^{(e)} = \\ \frac{\hbar^2}{2m_e^*} \left[ k^2 + \frac{m_e^*}{2m_h^*} \frac{k}{R} \sin(\theta_R + \theta_k) - (k_F^{(e)})^2 \right] . \end{aligned} \quad (4.49)$$

So that we obtain:

$$\begin{aligned} < \mathcal{N}(0) >_{vor} \simeq \frac{2m_e^*}{\hbar^2} \int_{FA} \frac{d\theta_k}{4\pi^2} \int_0^\infty dk k \int d\theta_R \\ \int_{\xi_V}^{d_V} dR \frac{R}{\pi d_V^2} \delta \left[ k^2 + \frac{m_e^*}{2m_h^*} \frac{k}{R} \sin(\theta_R + \theta_k) - (k_F^{(e)})^2 \right] . \end{aligned} \quad (4.50)$$

The integration over  $k$  can be done easily once one realizes that:

$$k^2 + \frac{m_e^*}{2m_h^*} \frac{k}{R} \sin(\theta_R + \theta_k) - (k_F^{(e)})^2 = (k - k_+)(k - k_-) , \quad (4.51)$$

$$k_{\pm} = \frac{m_e^*}{4m_h^* R} \sin(\theta_R + \theta_k) \pm \sqrt{\left[ \frac{m_e^*}{4m_h^* R} \sin(\theta_R + \theta_k) \right]^2 + \left( k_F^{(e)} \right)^2} .$$

We get:

$$\begin{aligned} < \mathcal{N}(0) >_{vor} \simeq \mathcal{N}(0) + \frac{m_e^*}{\hbar^2} \int_{FA} \frac{d\theta_k}{4\pi^2} \int d\theta_R \\ \int_{\xi_V}^{d_V} dR \frac{R}{\pi d_V^2} \frac{\frac{m_e^*}{4m_h^* R} \sin(\theta_R + \theta_k)}{\sqrt{\left[ \frac{m_e^*}{4m_h^* R} \sin(\theta_R + \theta_k) \right]^2 + \left( k_F^{(e)} \right)^2}} . \end{aligned} \quad (4.52)$$

Now, it is easy to check that the angular integration over  $\theta_R$  in the second term on the right hand side of Eq. (4.52) vanishes. Therefore we end with the following remarkable result:

$$\langle \mathcal{N}(0) \rangle_{vor} \simeq \mathcal{N}(0) . \quad (4.53)$$

Note that this last equation replaces Eq. (4.67) in I. Likewise, one can check that Eq. (4.53) extends also to thermal activated rotons which, in any case, are not relevant at low temperatures.

### 4.3 Low temperature specific heat

The specific heat is a bulk thermodynamic measurement that probes all excitations in a system. In order to extract the excitations arising only from the electronic quasiparticle density of states, all other contributions to the specific heat need to be subtracted out. Specific heat data refer to the specific heat per mole that are usually quoted in joules per mole per degree Kelvin. In the following, we will not distinguish between the specific heat at constant pressure and the specific heat at constant volume for, at low temperatures, the two specific heats differ by a negligible amount.

In the simplest case, the specific heat of a metal is the sum of the lattice specific heat, the phonon contribution, and the contribution of the conduction electrons. In the Debye model, the crystal lattice is considered as a continuous isotropic medium and thereby it turns out that the phonon contribution to the specific heat is proportional to  $T^3$  at low temperatures. At higher temperatures this Debye interpolation is insufficient to describe the phonon specific heat, so that one includes higher order terms. Usually, it turns out that it is enough to consider a term proportional to  $T^5$ . The resulting phonon contribution to the specific heat can be written as:

$$c_{phonon} = \beta_1 T^3 + \beta_2 T^5 . \quad (4.54)$$

Alternatively, the phonon contribution can be parametrized as:

$$c_{phonon} = \beta_1 T^3 + N_E \left( \frac{T}{T_E} \right)^2 \frac{e^{\frac{T}{T_E}}}{\left[ 1 - e^{\frac{T}{T_E}} \right]^2} . \quad (4.55)$$

The second term represents an Einstein contribution associated to optical phonons and it is characterized by the excitation of oscillators with a single frequency. In Eq. (4.55)  $T_E$  is the Einstein temperature and  $N_E$  is the Einstein constant. The electronic specific heat depends linearly on temperature, and it is the dominating contribution to the specific heat at sufficiently low temperatures:

$$c^{(e)} = \gamma T . \quad (4.56)$$

The constant  $\gamma$  can be easily obtained as the intercept at  $T = 0$  in a plot of  $c/T$  versus  $T^2$ . However, generally in hole doped cuprate superconductors an upturn of the specific heat has been found at very low temperatures [58, 59]. This upturn is interpreted as a Schottky anomaly. Indeed, it is known that in paramagnetic salts a Schottky anomaly has been observed. The Schottky specific heat at low temperatures may be significantly larger than the electronic and the lattice specific heats. The nature of the Schottky term

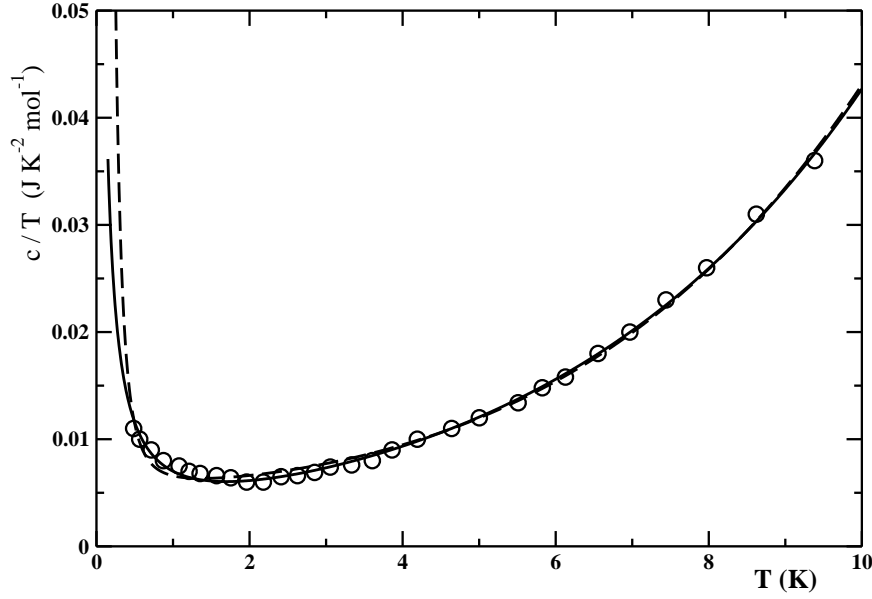


Figure 16: Temperature dependence of the specific heat divided by the temperature for underdoped YBCO,  $T_c \simeq 89 K$ . The data have been taken from Fig. 9.4, upper insert, in Ref. [59]. The dashed line is the best fit of data to Eq. (4.60). The solid line is the best fit of the data to Eq.(4.69).

is not well understood and it is generally ascribed to paramagnetic centers arising from disorder. The Schottky contribution to the specific heat is of the form:

$$c_{Schottky} = k_B N_A n z^2 \frac{e^z}{[1 + e^z]^2} , \quad z = \frac{g\mu_B H_{eff}}{k_B T} , \quad (4.57)$$

where  $\mu_B$  is the Bohr magneton,  $g$  is the Landè g-factor,  $n$  is the number of mole of the Schottky centers, and  $H_{eff}$  is a microscopic effective magnetic field. In the temperature regime of interest it results that  $k_B T \gg \mu_B H_{eff}$ , so that the Schottky specific heat falls off with the inverse square of the temperature:

$$c_{Schottky} \simeq \frac{a}{T^2} . \quad (4.58)$$

At low temperatures the specific heat comprises three contributions:

$$c(T) = c^{(e)}(T) + c_{phonon}(T) + c_{Schottky}(T) , \quad (4.59)$$

which, according to our previous discussion, can be written as:

$$c(T) \simeq \frac{a}{T^2} + \gamma T + \beta_1 T^3 + \beta_2 T^5 . \quad (4.60)$$

For illustrative purposes, in Fig. 16 we shows the low temperature specific heat data of underdoped YBCO,  $T_c \simeq 89 K$ . The data have been taken from Fig. 9.4, upper insert, in Ref. [59]. The low temperature upturn is clearly displayed by the specific heat data. In fact, we tried to fit the data to Eq. (4.60). As a result we found the following values for

the fitting parameters (see the dashed line in Fig. 16):

$$\begin{aligned} a &\simeq 0.714 \text{ mJ K mole}^{-1} , \\ \gamma &\simeq 5.66 \text{ mJ K}^{-2} \text{ mole}^{-1} , \\ \beta_1 &\simeq 0.212 \text{ mJ K}^{-4} \text{ mole}^{-1} , \\ \beta_2 &\simeq 0.0016 \text{ mJ K}^{-6} \text{ mole}^{-1} . \end{aligned} \tag{4.61}$$

An interesting feature resides in the fact that the fit leads to a non-zero value for  $\gamma$ . In fact, this holds quite generally in any hole doped cuprate superconductors with the observed values for  $\gamma$  in the range  $1 - 10 \text{ mJ K}^{-2} \text{ mole}^{-1}$ . The presence of such a term looks puzzling. In fully gapped superconductors the electronic specific heat is exponentially suppressed at low temperatures. On the other hand, if one identifies the nodal gap observed in angle resolved photoemission experiments with the d-wave BCS gap, then the density of states at the Fermi energy does not need to vanish along the gap nodes. In particular, the quasi two-dimensional d-wave gap proposed for cuprate superconductors gives rise to a quadratic temperature term in the specific heat. Moreover, the coefficient of the quadratic term associated with the lines of gap nodes may be estimated to be  $a_{\text{nodal}} \approx \gamma_n/T_c$ , where  $\gamma_n$  is the normal-state Sommerfeld coefficient. Therefore, one obtains the estimate  $a_{\text{nodal}} \approx 0.1 \text{ mJ K}^{-3} \text{ mole}^{-1}$ . Nevertheless, we added to the specific heat Eq. (4.60) the quadratic term  $a_{\text{nodal}} T^2$  and fitted the data. We obtained for the best fitted  $a_{\text{nodal}}$  a value consistent with zero,  $a_{\text{nodal}} \lesssim 0.01 \text{ mJ K}^{-3} \text{ mole}^{-1}$ . In general, these results are interpreted by assuming that the linear term  $\gamma T$  is an additive contribution to the specific heat which is extrinsic to the superconductivity. As concern the quadratic term, it is believed that such term is masked by the phonon contribution so that it is difficult to extract its value by fitting the low-temperature specific heat data.

We discuss, now, the peculiar temperature dependence of the specific heat at low temperatures in cuprate superconductors within our phenomenological theory. The specific heat is fully determined by the low-lying excitation of superfluid condensate. We have seen that the low-lying condensate excitations are the roton quasiparticles. However, at low temperatures the rotons contribution to the internal energy is exponentially suppressed. So that we are left with nodal quasielectrons as the only relevant low-energy excitations in the superconductive phase at low enough temperatures. We showed in Sect. 4.2 that the specific heat of the nodal quasielectron gas rises linearly with the temperature with Sommerfeld coefficient given by Eq. (4.44). However, we must take into account that nodal quasielectrons can be excited only in the phase disordered hole pair condensate. At low temperatures the phase disordered condensate is only a tiny fraction of the condensate. In fact, we may interpret the phase disordered condensate as the condensate normal fraction in an effective two fluid picture:

$$n_n(T) = n_s(0) - n_s(T) . \tag{4.62}$$

So that the fraction of phase disordered condensate is:

$$\frac{n_n(T)}{n_s(0)} = 1 - \frac{n_s(T)}{n_s(0)} \simeq 1 - e^{-b' \left[ \frac{1}{\sqrt{1-T/T_c}} - 1 \right]} = \frac{b'}{2} \frac{T}{T_c} + \mathcal{O}\left(\frac{T^2}{T_c^2}\right) , \quad T \ll T_c . \tag{4.63}$$

Therefore, at low temperatures the internal energy density of nodal quasielectrons is:

$$\mathbf{u}^{(ne)}(T) = n_n(T) \mathbf{u}^{(e)}(T) \simeq \frac{b'}{2} \frac{T}{T_c} \mathcal{N}(0) (\varepsilon_F^{(e)})^2 \left[ 1 + \frac{\pi^2}{3} \left( \frac{k_B T}{\varepsilon_F^{(e)}} \right)^2 \right] . \tag{4.64}$$



Whereupon one obtains the nodal quasielectron specific heat at constant volume:

$$c_V^{(ne)}(T) = \frac{\partial \mathbf{u}^{(ne)}(T)}{\partial T} , \quad (4.65)$$

and the molar specific heat:

$$c^{(ne)}(T) = a_0^2 N_A c_V^{(ne)}(T) \simeq \frac{b'}{2} a_0^2 N_A \mathcal{N}(0) \frac{(\varepsilon_F^{(e)})^2}{T_c} + \frac{\pi^2}{2} b' a_0^2 N_A \mathcal{N}(0) \frac{k_B^2}{T_c} T^2. \quad (4.66)$$

We see, then, that at low temperatures the nodal quasielectrons contribute to the specific heat with a term of the form:

$$c^{(ne)}(T) \simeq a_1 + a_2 T^2 , \quad (4.67)$$

where:

$$a_1 \simeq \frac{b'}{2} a_0^2 N_A \mathcal{N}(0) \frac{(\varepsilon_F^{(e)})^2}{T_c} , \quad a_2 \simeq \frac{\pi^2}{2} b' a_0^2 N_A \mathcal{N}(0) \frac{k_B^2}{T_c} . \quad (4.68)$$

Accordingly, we tried to fit the specific heat data with the following functional form:

$$c(T) \simeq a_1 + a_2 T^2 + \beta_1 T^3 + \beta_2 T^5 . \quad (4.69)$$

Remarkably, we found that Eq. (4.69) is able to track quite well the data. Indeed, we obtained the best fit with the following values of the parameters (see the full curve in Fig. 16):

$$\begin{aligned} a_1 &\simeq 5.307 \text{ mJ K}^{-1} \text{ mole}^{-1} , \\ a_2 &\simeq 1.534 \text{ mJ K}^{-3} \text{ mole}^{-1} , \\ \beta_1 &\simeq 0.088 \text{ mJ K}^{-4} \text{ mole}^{-1} , \\ \beta_2 &\simeq 0.0018 \text{ mJ K}^{-6} \text{ mole}^{-1} . \end{aligned} \quad (4.70)$$

Fig. 16 shows that both functional forms, Eq. (4.60) and Eq. (4.69), are quite consistent with measurements. Note that our Eq. (4.69) avoids to introduce a Schottky-like or a linear term to account for the temperature dependence of the low temperature specific heat. It must be mentioned, however, that if one evaluates the two coefficients  $a_1$  and  $a_2$  by means of the parameters of our model, then it results in an overestimate by order of magnitude with respect to the best-fitted values. At moment, we have not found any means of explaining this discrepancy.

To conclude the present Section, we would like to discuss the low temperature specific heat in presence of an applied magnetic field. At low temperatures and in magnetic fields of the order of a few Tesla it is well established that hole doped superconductors in the pseudogap region are in a vortex state. In fact, it results that  $H > H_{c1}$ , but the magnetic field strength is too small to suppress the superconductivity, i.e.  $H \ll H_{c2}$ . From the experimental point of view, it is established that the specific heat is of the form:

$$c(H, T) \simeq c(T) + \Delta c(H, T) , \quad (4.71)$$

where  $c(T)$  is the low-temperature specific heat in absence of the external magnetic field. The specific heat of most high temperature superconductors in external magnetic field displays a broad low temperature structure which usually is ascribed to a Schottky anomaly.

Even in this case, the origin of such anomaly is believed to arise from particles with spin whose concentration is, in general, dependent on the magnetic field strength. The Schottky contribution is given by Eq. (4.57) where  $H_{eff} \simeq H$  for strong enough applied magnetic fields. For temperatures not too low,  $T \gtrsim 3 - 4 K$ , the Schottky term is negligible and it turns out that  $\Delta c(H, T)$  increases linearly with the temperature. Therefore, we can write:

$$\Delta c(H, T) \simeq c_{Schottky}(H, T) + \gamma(H) T . \quad (4.72)$$

Early measurements on optimal doping YBCO [123, 124, 125, 126, 127] performed at magnetic fields up to  $16 T$  evidenced a coefficient of the low-temperature linear term growing with the magnetic field according to  $\gamma(H) \sim \sqrt{H}$ . This dependence on the magnetic field is understood to be a clear signature of a d-wave BCS gap [122, 128]. More recently, this peculiar dependence of  $\gamma(H)$  on the magnetic field strength has been confirmed in Ref. [129] where it is reported the low temperature measurements of the specific heat in underdoped YBCO with magnetic field up to  $45 T$ . However, in Ref. [130] it is reported the low temperature specific heat of underdoped YBCO ( $\delta \simeq 0.076, 0.084$ ) in applied magnetic field up to  $34.5 T$ . These authors observed two regimes in the low temperature limit. Namely, below a characteristic magnetic field  $H' \sim 13 T$  the coefficient of the linear temperature term in the specific heat behaves like  $\gamma(H) \sim \sqrt{H}$  as previously reported. However, near the above characteristic magnetic field there is a sharp inflection followed by a linear behavior of  $\gamma(H)$  with  $H$ :

$$\begin{aligned} \gamma(H) &= A_c H , \quad H \gtrsim H' , \\ A_c &\simeq 0.16 \text{ mJ K}^{-2} \text{ mole}^{-1} T^{-1} . \end{aligned} \quad (4.73)$$

Indeed, we shall see that in our theory we can account quite easily for  $\Delta c(H, T)$  of the form given by Eq. (4.72) with  $\gamma(H) \sim H$ , as well as with a suitable Schottky term. In type-II superconductors the applied magnetic field exceeding the lower critical field penetrates into the system with an array of Abrikosov vortices. Since an Abrikosov vortex carries one magnetic flux quantum, as the applied magnetic field increases more and more Abrikosov vortices are formed. As discussed in Sect. 3.5, in our theory the upper critical magnetic field is much smaller than the Landau-Ginzburg critical magnetic field where the Abrikosov vortices become to overlap. So that, the density of Abrikosov vortices is given by:

$$n_V \simeq \frac{H}{\phi_0} . \quad (4.74)$$

From Eq. (4.74) it follows that the average distance between vortices is  $d_H \simeq \sqrt{\phi_0/H}$ . Now, it is easy to check that  $d_H \gg \xi_V \simeq d_0$  for applied magnetic field strengths up to  $40 T$ . Therefore, we see that we may employ safely the dilute vortex approximation. Concerning the specific heat at low temperatures, we already noticed that the only relevant low-energy excitations are the nodal quasielectrons which, however, can be excited only in the phase disordered condensate. Since we argued that in the vortex core the condensate is phase disordered, we see that at low temperatures the specific heat comprises two contributions due to nodal quasielectrons excitations arising from the disorder condensate fraction outside the vortices and the disorder condensate in the vortex cores. Therefore, since the Abrikosov vortices are dilute, to a good approximation the specific heat can be written as in Eq. (4.71). The first term on the right hand side of Eq. (4.71) is the contribution due to the tiny disorder fraction of the hole condensate. Evidently this term is

almost independent on the strength of the applied magnetic field and it has been already discussed. Now we show that the other term can be written as in Eq. (4.72). In fact, we have written down the nodal quasielectron contribution to the constant volume specific heat, Eq. (4.41). Therefore we have:

$$\Delta c_V^{(ne)}(H, T) \simeq \pi \xi_V^2 \frac{H}{\phi_0} \frac{2}{3} \pi^2 < \mathcal{N}(0) >_{vor} k_B^2 T, \quad (4.75)$$

and the molar specific heat:

$$\Delta c^{(ne)}(H, T) = a_0^2 N_A \Delta c_V^{(ne)}(H, T). \quad (4.76)$$

Taking into account Eq. (4.53) and Eq. (4.44) we can write:

$$\Delta c^{(ne)}(H, T) = \gamma(H) T, \quad (4.77)$$

where:

$$\gamma(H) \simeq \pi \xi_V^2 \frac{H}{\phi_0} a_0^2 N_A \frac{2}{3} \pi^2 \mathcal{N}(0) k_B^2 = \pi \xi_V^2 \frac{H}{\phi_0} \gamma_S. \quad (4.78)$$

Evidently,  $\gamma(H)$  is conform to Eq. (4.73) with

$$A_s \simeq \pi \xi_V^2 \frac{1}{\phi_0} \gamma_S. \quad (4.79)$$

The Schottky-like term in the specific heat arises as follows. In the Abrikosov vortex core there is a non-zero microscopic magnetic field  $h(0)$ . Now, the spatial average of  $h(0)$  is the magnetic induction  $B$  not the applied magnetic field  $H$ . For magnetic field strengths employed in the experiments and at low temperatures the microscopic magnetic field is given by Eq. (3.113):

$$h(0) \simeq \frac{\phi_0}{2\pi\lambda^2(0)} \ln(\kappa). \quad (4.80)$$

This tiny magnetic field induces the Zeeman splitting of the energy of the hole bound states (see I, Sect. 4.1):

$$\varepsilon_{Zeeman} \simeq \pm \frac{\hbar e h(0)}{m_h^* c}. \quad (4.81)$$

The presence of energy levels separated by a very small energy difference gives rise to the specific heat at constant volume:

$$c_V^{Zeeman}(H, T) \simeq k_B z^2 \frac{e^z}{[1 + e^z]^2}, \quad z = \frac{2\hbar e h(0)}{m_h^* c k_B T}. \quad (4.82)$$

So that we find the following Schottky-like molar specific heat:

$$c_{Schottky}(H, T) = \pi \xi_V^2 \frac{H}{\phi_0} a_0^2 N_A c_V^{Zeeman}(H, T). \quad (4.83)$$

Actually, since  $\varepsilon_{Zeeman} \ll k_B T$ , the Schottky-like specific heat can be written as:

$$c_{Schottky}(H, T) \simeq A \frac{H}{T^2}. \quad (4.84)$$

In conclusion, we found that at low temperatures and in external magnetic field the specific heat acquires an additional contribution which can be parametrized as:

$$\Delta c(H, T) \simeq A \frac{H}{T^2} + A_s H T. \quad (4.85)$$

Even though Eq. (4.85) seems to be in qualitative agreement with observations, it would be of great interest to reanalyze the experimental data following our theoretical suggestions.

## 5 Charge Density Wave Instability

In this Section we will focus on charge order in hole doped cuprate superconductors in the pseudogap region <sup>12</sup>. For charge order, in general, it is intended an electronic phase which breaks translational symmetry through a self - organization into periodic structures incompatible with the periodicity of the underlying lattice. In fact, there is growing evidence of a charge order existing in the pseudogap state of several cuprate families (see Refs. [132, 133, 134, 135, 136, 137, 138, 139, 140, 141, 142, 143, 144, 145, 146, 147, 148, 149, 150, 151, 152]) which also coexists and competes with superconductivity at lower temperatures. Recently, it seems that there is a consensus on the presence of periodic modulations in the electronic density, a phenomenon called charge density wave (CDW). Clearly, the ubiquitous presence of charge density wave correlations is adding complexity to the physics of high temperature superconductivity.

Charge density waves were discussed long time ago by Fröhlich [153] and Peierls [154] (see also Refs. [155, 156] and references therein). In fact, it was pointed out that a one dimensional metal coupled to the underlying lattice is not stable at low temperatures. Due to the peculiar topology of the Fermi surface in one dimensional metals with respect to three dimensional systems, the bare charge susceptibility diverges at wavevector  $q = 2k_F$ , where  $k_F$  is the Fermi wavenumber. As a result, the formation of an electronic charge modulation with wavevector  $q$  is favored with respect to homogeneous configurations. Since in conductors the electrons are coupled to the ion lattices, such a deep reorganization of the electronic carrier distribution alters the ionic lattice resulting in a small deformation to lower the total electrostatic energy of the electron-phonon system. In fact, the ions move towards new equilibrium positions leading to the so-called Peierls deformation. The ionic displacements are limited in extent not to exceed in the elastic energy cost. The resulting ground state of the coupled electron-phonon system is characterized by a gap in the single-particle excitation spectrum and by the presence of collective modes. Usually, a ground state with density waves is associated to a highly anisotropic conduction bands, such as organic and inorganic materials with quasi-one dimensional or quasi-two dimensional electronic structures [155, 156].

Besides the electronic spectrum, the formation of a charge density wave also affects other quasiparticle excitations. Most prominently there appears the so-called Kohn anomaly [157] which correspond to a softening of the phonon responsible for the electron-phonon instability. Remarkably, in hole doped cuprate superconductors in the pseudogap region it seems that giant phonon anomalies are common to the  $CuO_2$  planes. In particular, neutron and X-ray inelastic scattering studies identified the anomalous behavior of longitudinal optical phonons arising from the in-plane  $Cu - O$  bond-stretching modes (see the review Ref. [158] and references therein). These anomalies resemble those associated with the observed Kohn anomalies in quasi one-dimensional conductors with nested Fermi surfaces. This strongly suggests that the in-plane  $Cu - O$  bond-stretching modes are deeply involved in the observed charge density wave formation in the underdoped cuprates. In our highly idealized model there are two degenerate bond-stretching longitudinal optical phonon modes, as schematically illustrated in Fig. 17. In the pseudogap region the only low-lying excitations which may interact with these longitudinal phonons are the nodal quasielectrons. In fact, we have seen in Sect. 5 that the nodal quasielectrons are intimately tied to the bound hole pairs. The Coulomb interactions between the nodal

---

<sup>12</sup>For a recent review see Ref. [131].

quasielectrons and the lattice ions give rise to an effective electron-phonon coupling. Now, we consider a model Hamiltonian where the coupling of the nodal quasielectrons with the bond-stretching phonons is at the heart of the charge density wave instabilities. Evidently the planar lattice displacements are written as (see Fig. 17):

$$\vec{u}(\vec{r}) = u_1(\vec{r}) \hat{x} + u_2(\vec{r}) \hat{y} \quad , \quad \vec{r} = (x, y) \quad . \quad (5.1)$$

Adopting the quasi-harmonic approximation the in-plane lattice vibrations are described by the following Hamiltonian:

$$\hat{H}^{(ph)} = \sum_{i=1}^2 \sum_{\vec{q}} \left\{ \frac{\hat{P}_i(\vec{q}) \hat{P}_i(-\vec{q})}{2M} + \frac{M\Omega^2(\vec{q})}{2} \hat{Q}_i(\vec{q}) \hat{Q}_i(-\vec{q}) \right\} , \quad (5.2)$$

where  $\hat{Q}_i(\vec{q})$  and  $\hat{P}_i(\vec{q})$ ,  $i = 1, 2$ , are the normal coordinates and conjugate momenta corresponding to the lattice displacements  $u_1(\vec{r})$  and  $u_2(\vec{r})$  respectively;  $\Omega(\vec{q})$  is the normal mode frequency with wavevector  $\vec{q}$ , and  $M$  is the reduced atomic mass of the *Cu* and *O* ions:

$$\frac{1}{M} = \frac{1}{M_{Cu}} + \frac{1}{M_O} \quad . \quad (5.3)$$

We may introduce the phonon creation and annihilation operators as follows:

$$\hat{Q}_i(\vec{q}) = \sqrt{\frac{\hbar}{2M\Omega(\vec{q})}} \left[ \hat{b}_i(\vec{q}) + \hat{b}_i^\dagger(-\vec{q}) \right] , \quad (5.4)$$

$$\hat{P}_i(\vec{q}) = i \sqrt{\frac{\hbar M \Omega(\vec{q})}{2}} \left[ \hat{b}_i^\dagger(\vec{q}) - \hat{b}_i(-\vec{q}) \right] . \quad (5.5)$$

These operators satisfy the canonical commutation relations:

$$\left[ \hat{b}_i(\vec{q}) , \hat{b}_j^\dagger(\vec{q}') \right] = \delta_{i,j} \delta_{\vec{q},\vec{q}'} , \quad (5.6)$$

while all the other commutators are vanishing. In fact, it is easy to check that:

$$\left[ \hat{Q}_i(\vec{q}) , \hat{P}_j(\vec{q}') \right] = i \hbar \delta_{i,j} \delta_{\vec{q},\vec{q}'} . \quad (5.7)$$

Using Eqs. (5.4), (5.5) and (5.6) the phonon Hamiltonian can be rewritten as:

$$\hat{H}^{(ph)} = \sum_{i=1}^2 \sum_{\vec{q}} \hbar \Omega(\vec{q}) \left[ \hat{b}_i^\dagger(\vec{q}) \hat{b}_i(\vec{q}) + \frac{1}{2} \right] . \quad (5.8)$$

The planar lattice displacements can be expressed in terms of the creation and annihilation operators according to:

$$u_i(\vec{r}) = \frac{1}{\sqrt{N_u}} \sum_{\vec{q}} \sqrt{\frac{\hbar}{2M\Omega(\vec{q})}} \left[ \hat{b}_i(\vec{q}) + \hat{b}_i^\dagger(-\vec{q}) \right] e^{i\vec{q} \cdot \vec{r}} , \quad (5.9)$$

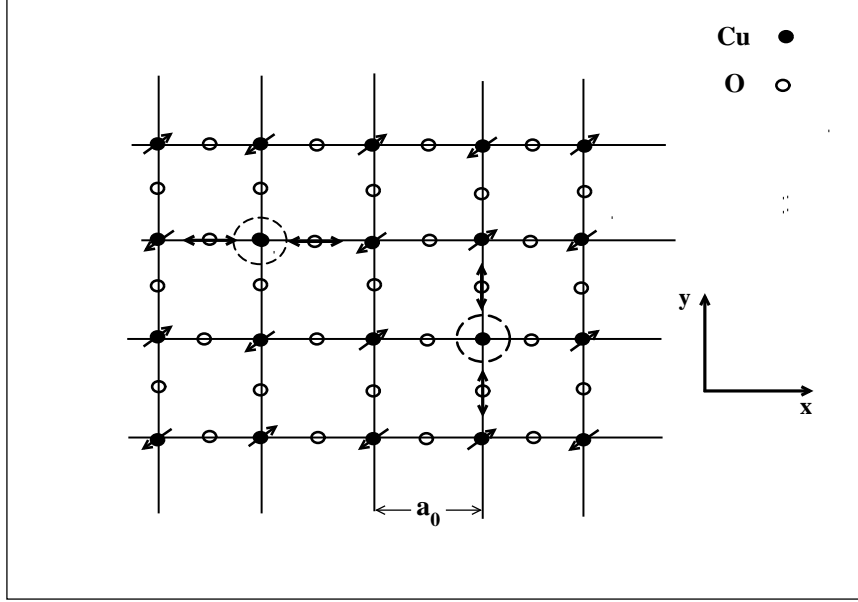


Figure 17: The idealized square copper-oxide plane with lattice spacing  $a_0$ . The dashed ellipses represent two holes in the antiferromagnetic background. The arrows indicate the longitudinal bond-stretching modes along the planar  $Cu - O$  bonds.

where  $N_u$  is the number of unit cell such that the lattice volume is  $V = N_u V_u$ ,  $V_u = a_0^2$  being the unit cell volume. As concern the nodal quasielectron Hamiltonian, according to Sect. 4 we have:

$$\hat{H}^{(e)} = \sum_{\vec{k}, \sigma} \left( \varepsilon_{\vec{k}}^{(e)} - \varepsilon_F^{(e)} \right) \hat{\psi}_e^\dagger(\vec{k}, \sigma) \hat{\psi}_e(\vec{k}, \sigma). \quad (5.10)$$

The electron-phonon interaction is usually obtained in the rigid ion approximation. In terms of the creation and annihilation operators the interaction Hamiltonian reads:

$$\hat{H}^{(e-ph)} \simeq \frac{1}{V} \sum_{\vec{q}, \vec{k}, \sigma} \sum_{i=1}^2 g_i(\vec{q}) \left( \hat{b}_i(\vec{q}) + \hat{b}_i^\dagger(-\vec{q}) \right) \hat{\psi}_e^\dagger(\vec{k} + \vec{q}, \sigma) \hat{\psi}_e(\vec{k}, \sigma), \quad (5.11)$$

where [156]

$$g_i(\vec{q}) \simeq \sqrt{\frac{\hbar}{2M\Omega(\vec{q})}} |q_i| V(\vec{q}), \quad \vec{q} = (q_1, q_2). \quad (5.12)$$

In Eq. (5.12)  $V(\vec{q})$  is the Fourier transform of the interaction potential between nodal quasielectrons and the lattice ions. Accordingly, we assume:

$$V(\vec{q}) \simeq \int d\vec{r} e^{i\vec{q}\cdot\vec{r}} \frac{e^2}{|\vec{r}|} = \frac{2\pi e^2}{|\vec{q}|}. \quad (5.13)$$

Therefore, we are lead to the following effective Fröhlich Hamiltonian:

$$\hat{H}_{eff} = \hat{H}^{(e)} + \hat{H}^{(ph)} + \hat{H}^{(e-ph)}. \quad (5.14)$$

Note that the interaction Hamiltonian Eq. (5.11) can be rewritten as:

$$\hat{H}^{(e-ph)} \simeq \frac{1}{V} \sum_{\vec{q}, \vec{k}, \sigma} \sum_{i=1}^2 g_i(\vec{q}) \sqrt{\frac{2M\Omega(\vec{q})}{\hbar}} \hat{\psi}_e^\dagger(\vec{k} + \vec{q}, \sigma) \hat{\psi}_e(\vec{k}, \sigma) \hat{Q}_i(\vec{q}) . \quad (5.15)$$

Moreover, we have:

$$g_i(\vec{q}) \simeq \sqrt{\frac{\hbar}{2M\Omega(\vec{q})}} 2\pi e^2 \hat{q}_i . \quad (5.16)$$

It is useful to consider the equation of motion of the normal coordinates:

$$\frac{\partial}{\partial t} \hat{Q}_i(\vec{q}, t) = \frac{1}{i\hbar} [\hat{Q}_i, \hat{H}_{eff}] . \quad (5.17)$$

A straightforward calculation leads to:

$$\frac{\partial}{\partial t} \hat{Q}_i(\vec{q}, t) = \frac{\hat{P}_i(\vec{q}, t)}{M} . \quad (5.18)$$

Using Eq. (5.18) we obtain at once:

$$\begin{aligned} \frac{\partial^2}{\partial t^2} \hat{Q}_i(\vec{q}, t) &= \frac{1}{i\hbar} \left[ \frac{\hat{P}_i}{M}, \hat{H}_{eff} \right] = -\Omega^2(\vec{q}) \hat{Q}_i(\vec{q}, t) \\ &- g_i(\vec{q}) \sqrt{\frac{2\Omega(\vec{q})}{\hbar M}} \frac{1}{V} \sum_{\vec{k}, \sigma} \hat{\psi}_e^\dagger(\vec{k} + \vec{q}, \sigma) \hat{\psi}_e(\vec{k}, \sigma) . \end{aligned} \quad (5.19)$$

The last term on the right hand side of Eq. (5.19) is the effective force due to the modulation of the quasielectron density induced by the lattice displacements. To evaluate this term we use the adiabatic approximation, namely we are supposing that the ion and quasielectron motion can be decoupled. In fact, when a longitudinal wave progresses through the lattice, causing local rarefactions and compressions in the ion density, we may suppose that the quasielectrons move so as to screen out these fluctuations. Since the quasielectrons are able to respond to perturbations in times much shorter than the inverse lattice frequencies, then they will effectively be following the motion of the lattice instantaneously. Thereby, the presence of the quasielectrons results in a renormalization of the longitudinal frequencies of the ion vibrations. Within the framework of the linear response theory a time independent external potential  $\phi_{ex}(\vec{r})$  coupled to the quasielectron gas leads to a rearrangement of the density which, expressed in Fourier space, is given by [159, 160]:

$$\hat{\rho}(\vec{q}) = \left\langle \frac{1}{V} \sum_{\vec{k}, \sigma} \hat{\psi}_e^\dagger(\vec{k} + \vec{q}, \sigma) \hat{\psi}_e(\vec{k}, \sigma) \right\rangle = \chi(\vec{q}) \hat{\phi}_{ex}(\vec{q}) , \quad (5.20)$$

where the brackets mean the quantum average over the fermion degrees of freedom. In Eq. (5.20)  $\chi(\vec{q})$  is the so-called static Lindhard response function:

$$\chi(\vec{q}) = \frac{1}{V} \sum_{\vec{k}, \sigma} \frac{n(\vec{k}) - n(\vec{k} + \vec{q})}{\varepsilon_{\vec{k}}^{(e)} - \varepsilon_{\vec{k} + \vec{q}}^{(e)}} , \quad (5.21)$$

where  $n(\vec{k})$  is the zero-temperature occupation number,  $n(\vec{k}) = 1$  if  $\varepsilon_{\vec{k}}^{(e)} < \varepsilon_F^{(e)}$ ,  $n(\vec{k}) = 0$  otherwise. From Eq. (5.15) we infer that:

$$\hat{\phi}_{ex}(\vec{q}) = \frac{g_i(\vec{q})}{V_u} \sqrt{\frac{2M\Omega(\vec{q})}{\hbar}} \hat{Q}_i(\vec{q}) . \quad (5.22)$$

So that, in the adiabatic approximation, one obtains:

$$\left\langle \frac{1}{V} \sum_{\vec{k}, \sigma} \hat{\psi}_e^\dagger(\vec{k} + \vec{q}, \sigma) \hat{\psi}_e(\vec{k}, \sigma) \right\rangle \simeq \chi(\vec{q}) \frac{g_i(\vec{q})}{V_u} \sqrt{\frac{2M\Omega(\vec{q})}{\hbar}} \hat{Q}_i(\vec{q}) . \quad (5.23)$$

Inserting this last equation into Eq. (5.19) we get:

$$\frac{\partial^2}{\partial t^2} \hat{Q}_i(\vec{q}, t) \simeq - \left[ \Omega^2(\vec{q}) + \frac{2g_i^2(\vec{q})}{\hbar V_u} \chi(\vec{q}) \Omega(\vec{q}) \right] \hat{Q}_i(\vec{q}, t) . \quad (5.24)$$

Eq. (5.24) shows that, indeed, the quasielectrons give rise to a renormalization of the longitudinal bond-stretching frequencies:

$$\tilde{\Omega}^2(\vec{q}) \simeq \Omega^2(\vec{q}) + \frac{2g_i^2(\vec{q})}{\hbar V_u} \chi(\vec{q}) \Omega(\vec{q}) . \quad (5.25)$$

At finite temperatures one must perform the thermal average over the fermion degrees of freedom. As a result Eq. (5.23) still holds by replacing the zero-temperature Lindhard function with:

$$\chi(\vec{q}, T) = \frac{1}{V} \sum_{\vec{k}, \sigma} \frac{f(\varepsilon_{\vec{k}}^{(e)}) - f(\varepsilon_{\vec{k}+\vec{q}}^{(e)})}{\varepsilon_{\vec{k}}^{(e)} - \varepsilon_{\vec{k}+\vec{q}}^{(e)}} , \quad (5.26)$$

where  $f(\varepsilon)$  is the Fermi-Dirac distribution function Eq. (4.31).

For a one-dimensional electron gas it turns out that  $\chi(\vec{q})$  diverges at the Fermi surface nesting wavevectors  $|\vec{q}| = Q = 2k_F$ . The divergence of  $\chi(Q)$  implies that at zero temperature the one-dimensional electron gas is unstable with respect to the formation of a periodically varying electron charge density. At finite temperatures  $\chi(\vec{q}, T)$  attains its maximum value at  $|\vec{q}| = Q$ . Consequently the softening of the renormalized phonon frequencies  $\tilde{\Omega}(\vec{q})$  will be most significant at these wavevectors. In fact, for the one-dimensional electron gas the renormalized phonon frequency at  $|\vec{q}| = Q$  goes to zero at a critical temperature:

$$\tilde{\Omega}^2(Q, T_{CDW}) = 0 . \quad (5.27)$$

At the critical temperature  $T_{CDW}$  there is a phase transition to a state with a periodic static lattice distortion and an electron charge density modulation. This transition is generally referred to as the Peierls transition.

## 5.1 Charge-ordering wavenumber vectors

To determine the critical temperature of the Peierls instability in the nodal quasielectron gas we need to establish the divergences of the zero-temperature static Lindhard response function at some wavevector  $\vec{q} = \vec{Q}$ . Evidently we have:

$$\chi(\vec{q}) = 2 \int \frac{d\vec{k}}{(2\pi)^2} \frac{n(\vec{k}) - n(\vec{k} + \vec{q})}{\varepsilon_{\vec{k}}^{(e)} - \varepsilon_{\vec{k}+\vec{q}}^{(e)}} . \quad (5.28)$$



Now, we note that:

$$\int \frac{d\vec{k}}{(2\pi)^2} \frac{n(\vec{k} + \vec{q})}{\varepsilon_{\vec{k}}^{(e)} - \varepsilon_{\vec{k}+\vec{q}}^{(e)}} = \int \frac{d\vec{k}}{(2\pi)^2} \frac{n(\vec{k})}{\varepsilon_{\vec{k}-\vec{q}}^{(e)} - \varepsilon_{\vec{k}}^{(e)}} . \quad (5.29)$$

Putting  $\vec{k} \rightarrow -\vec{k}$  and noting that  $\varepsilon_{-\vec{k}}^{(e)} = \varepsilon_{\vec{k}}^{(e)}$ , we get:

$$\int \frac{d\vec{k}}{(2\pi)^2} \frac{n(\vec{k} + \vec{q})}{\varepsilon_{\vec{k}}^{(e)} - \varepsilon_{\vec{k}+\vec{q}}^{(e)}} = \int \frac{d\vec{k}}{(2\pi)^2} \frac{n(\vec{k})}{\varepsilon_{\vec{k}+\vec{q}}^{(e)} - \varepsilon_{\vec{k}}^{(e)}} . \quad (5.30)$$

So that we can write:

$$\chi(\vec{q}) = 4 \int \frac{d\vec{k}}{(2\pi)^2} \frac{n(\vec{k})}{\varepsilon_{\vec{k}}^{(e)} - \varepsilon_{\vec{k}+\vec{q}}^{(e)}} . \quad (5.31)$$

Since

$$\varepsilon_{\vec{k}}^{(e)} - \varepsilon_{\vec{k}+\vec{q}}^{(e)} = -\frac{\hbar^2 q}{m_e^*} \left[ \frac{q}{2} + k \cos \theta_{kq} \right] , \quad (5.32)$$

we readily obtain:

$$\chi(\vec{q}) = -\frac{m_e^*}{\pi^2 \hbar^2 q} \int_{FA} d\theta_k \int_0^{k_F^{(e)}} dk \frac{k}{\frac{q}{2} + k \cos \theta_{kq}} . \quad (5.33)$$

It is convenient to rewrite Eq. (5.33) as:

$$\begin{aligned} \chi(\vec{q}) = & -\frac{m_e^*}{\pi^2 \hbar^2 q} \int_{FA} d\theta_k \int_0^{k_F^{(e)}} dk \\ & \left[ \frac{1}{\cos \theta_{kq}} - \frac{q}{2 \cos \theta_{kq}} \frac{1}{\frac{q}{2} + k \cos \theta_{kq}} \right] . \end{aligned} \quad (5.34)$$

We see that the singularity in  $\chi(\vec{q})$  arises from the second term in the square brackets on the right hand side of Eq. (5.34) whenever:

$$q + 2 k_F^{(e)} \cos \theta_{kq} = 0 . \quad (5.35)$$

In Fig. 18 we display the nodal quasielectron Fermi arcs in the first Brillouin zone. It is worthwhile to recall that the  $k_x, k_y$  axes are oriented along the copper-oxygen bonds.  $Q_1$  and  $Q_2$  are the wavenumbers satisfying Eq. (5.35) that are relevant to trigger the density wave instabilities in the longitudinal bond-stretching planar modes. In fact, it is easy to see that, when

$$\vec{q} = \pm \vec{Q}_1 , \pm \vec{Q}_2 \quad ; \quad \vec{Q}_1 = (\sqrt{2} k_F^{(e)}, 0) , \quad \vec{Q}_2 = (0, \sqrt{2} k_F^{(e)}) , \quad (5.36)$$

the static response function diverges logarithmically. Let us consider, for instance,  $\vec{q} = -\vec{Q}_1$ . The singular part of the Lindhard function is:

$$\chi(Q_1) \simeq +\frac{m_e^*}{2\pi^2 \hbar^2} \int_{FA} d\theta_k \int_0^{k_F^{(e)}} dk \frac{1}{\cos \theta_{kq}} \frac{1}{\frac{q}{2} + k \cos \theta_{kq}} . \quad (5.37)$$

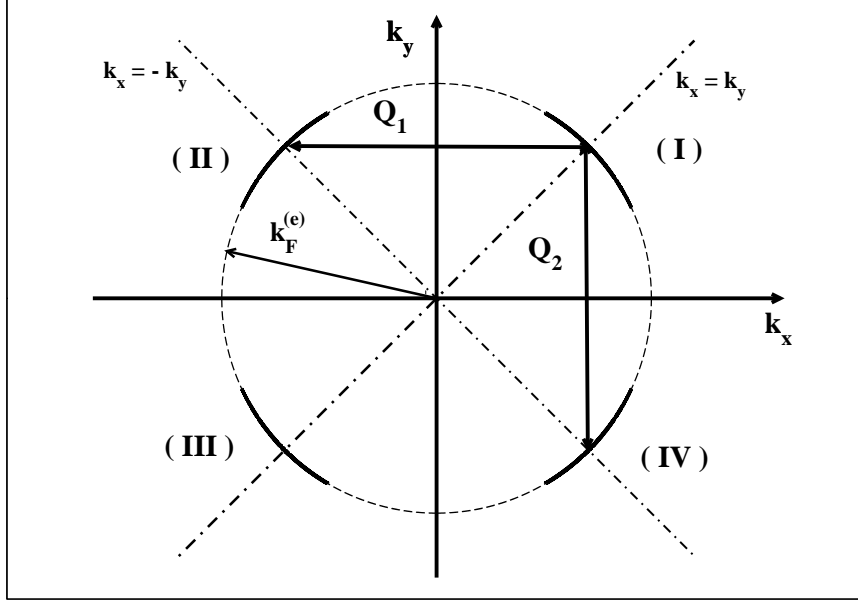


Figure 18: The quasielectron Fermi arcs in the first Brillouin zone labelled as in Fig. 12.  $Q_1$  and  $Q_2$  are the nesting wavenumbers leading to the charge density wave instability in the planar lattice displacements  $u_1(\vec{r})$  and  $u_2(\vec{r})$  respectively.

We find:

$$\chi(Q_1) \simeq + 2 \theta_{FA} \frac{m_e^*}{\pi^2 \hbar^2} \ln \left| 1 - \frac{\sqrt{2} k_F^{(e)}}{Q_1} \right|, \quad (5.38)$$

or, using Eq. (4.33)

$$\chi(Q_1) \simeq + 2 \mathcal{N}(0) \ln \left| 1 - \frac{\sqrt{2} k_F^{(e)}}{Q_1} \right|. \quad (5.39)$$

Obviously, Eq. (5.39) applies also to the wavevectors  $+\vec{Q}_1, \pm\vec{Q}_2$  since  $|\vec{Q}_1| = |\vec{Q}_2|$ . The logarithmic divergence of the static response function points to the instability of the nodal quasielectron gas towards the formation of a charge density wave. To determine the onset temperature for this instability we need to evaluate the Lindhard response function at finite temperatures:

$$\chi(\vec{q}, T) = 2 \int \frac{d\vec{k}}{(2\pi)^2} \frac{f(\varepsilon_{\vec{k}}^{(e)}) - f(\varepsilon_{\vec{k}+\vec{q}}^{(e)})}{\varepsilon_{\vec{k}}^{(e)} - \varepsilon_{\vec{k}+\vec{q}}^{(e)}}. \quad (5.40)$$

The main contributions to the integral in Eq. (5.40) come around the Fermi energy. So that we can write:

$$\varepsilon_{\vec{k}}^{(e)} - \varepsilon_F^{(e)} \simeq + \frac{\hbar^2 k_F^{(e)}}{m_e^*} (k - k_F^{(e)}), \quad (5.41)$$

$$\varepsilon_{\vec{k}+\vec{q}}^{(e)} - \varepsilon_F^{(e)} \simeq + \frac{\hbar^2}{2m_e^*} (q^2 + 2kq \cos \theta_{kq}), \quad (5.42)$$

$$\varepsilon_{\vec{k}}^{(e)} - \varepsilon_{\vec{k}+\vec{q}}^{(e)} \simeq - \frac{\hbar^2}{2m_e^*} (q^2 + 2kq \cos \theta_{kq}). \quad (5.43)$$

Therefore, for  $\vec{q} = -\vec{Q}_1$  we get:

$$\varepsilon_{\vec{k}+\vec{q}}^{(e)} - \varepsilon_F^{(e)} \simeq - \frac{\hbar^2 k_F^{(e)}}{m_e^*} (k - k_F^{(e)}) \simeq - (\varepsilon_{\vec{k}}^{(e)} - \varepsilon_F^{(e)}) , \quad (5.44)$$

$$\varepsilon_{\vec{k}}^{(e)} - \varepsilon_{\vec{k}+\vec{q}}^{(e)} \simeq + \frac{\hbar^2 k_F^{(e)}}{m_e^*} (k - k_F^{(e)}) \simeq + (\varepsilon_{\vec{k}}^{(e)} - \varepsilon_F^{(e)}) . \quad (5.45)$$

So that one finds:

$$\chi(Q_1, T) \simeq 2 \int \frac{d\vec{k}}{(2\pi)^2} \frac{f(\xi_{\vec{k}}) - f(-\xi_{\vec{k}})}{\xi_{\vec{k}}} , \quad \xi_{\vec{k}} = \varepsilon_{\vec{k}}^{(e)} - \varepsilon_F^{(e)} . \quad (5.46)$$

Now, observing that

$$\int \frac{d\vec{k}}{(2\pi)^2} \simeq \mathcal{N}(0) \int d\varepsilon_k^{(e)} , \quad (5.47)$$

we obtain:

$$\chi(Q_1, T) \simeq 2 \mathcal{N}(0) \int d\varepsilon_k^{(e)} \frac{f(\xi_{\vec{k}}) - f(-\xi_{\vec{k}})}{\xi_{\vec{k}}} \simeq 2 \mathcal{N}(0) \int_0^{\varepsilon_c} d\xi \frac{f(\xi) - f(-\xi)}{\xi} , \quad (5.48)$$

where  $\varepsilon_c$  is a high-energy cutoff. Finally, using

$$f(\xi) - f(-\xi) = - \tanh \left( \frac{\xi}{2k_B T} \right) , \quad (5.49)$$

we recast Eq. (5.48) into:

$$\chi(Q_1, T) \simeq - 2 \mathcal{N}(0) \int_0^{\frac{\varepsilon_c}{2k_B T}} \frac{dx}{x} \tanh x . \quad (5.50)$$

After taking into account that:

$$\int_0^\Lambda \frac{dx}{x} \tanh x \simeq \ln \Lambda - \ln \pi + 2 \ln 2 + \gamma , \quad (5.51)$$

where  $\gamma = 0.577216\dots$  is the Euler's constant<sup>13</sup>, we obtain finally:

$$\chi(Q_1, T) \simeq - 2 \mathcal{N}(0) \ln \left( \frac{2e^\gamma}{\pi} \frac{\varepsilon_c}{k_B T} \right) . \quad (5.52)$$

Regarding the cutoff energy  $\varepsilon_c$ , usually it is assumed to be of the order of the Fermi energy  $\varepsilon_F^{(e)}$ . However, as discussed in Sect. 4, the nodal quasielectrons are intimately related to the hole pairs. Therefore the natural high-energy cutoff should be the binding energy of the hole pairs:

$$\varepsilon_c \simeq \Delta_2(\delta) \quad (5.53)$$

which, indeed, turns out to be much smaller than the Fermi energy,  $\Delta_2(\delta) \ll \varepsilon_F^{(e)}$ .

---

<sup>13</sup>We must mention that in the literature sometimes our Euler's constant is denoted by  $C$ , while  $\gamma = e^C$ .

## 5.2 Critical temperature and gap

In the previous Section we argued that the nodal quasielectron density fluctuations at  $q = Q_1, Q_2$  cause the linear response function to diverge at low temperatures. In the pseudogap region, where  $\theta_{FA} \ll 1$ , the physical motivations for these instabilities reside on the fact that the nodal quasielectrons behave like the conduction electrons in quasi one-dimensional conductors. In fact, the wavevectors  $\pm \vec{Q}_1, \pm \vec{Q}_2$  are the nesting vectors connecting the Fermi arc sectors  $(I) - (II)$ ,  $(III) - (IV)$  and  $(I) - (IV)$ ,  $(II) - (III)$  respectively (see Fig. 18).

As discussed early, with decreasing temperature the renormalized longitudinal phonon frequency decreases and eventually it goes to zero. Indeed, inserting Eq. (5.52) into Eq. (5.25) we get:

$$\tilde{\Omega}^2(Q_1, T) \simeq \Omega^2(Q_1) \left[ 1 - \frac{4g^2(\vec{q})\mathcal{N}(0)}{\hbar\Omega(Q_1)V_u} \ln \left( \frac{2e^\gamma}{\pi} \frac{\varepsilon_c}{k_B T} \right) \right], \quad (5.54)$$

where, according to Eq. (5.16)

$$g(Q_1) \simeq \sqrt{\frac{\hbar}{2M\Omega(Q_1)}} 2\pi e^2. \quad (5.55)$$

Therefore, the critical temperature given by Eq. (5.27) is:

$$k_B T_{CDW} \simeq \frac{2e^\gamma}{\pi} \varepsilon_c e^{-\frac{\hbar\Omega(Q_1)V_u}{4g^2(Q_1)\mathcal{N}(0)}}. \quad (5.56)$$

Taking into account Eqs. (2.15) and (5.53) we find:

$$T_{CDW}(\delta) \simeq \frac{4e^\gamma}{\pi} T^*(\delta) e^{-\frac{\hbar\Omega(Q_1)V_u}{4g^2(Q_1)\mathcal{N}(0)}}. \quad (5.57)$$

Note that the doping dependence of the charge density wave critical temperature arises from the pseudogap temperature:

$$T^*(\delta) \simeq T^*(0) \left[ 1 - \left( \frac{\delta}{\delta_c} \right)^{\frac{3}{2}} \right], \quad (5.58)$$

and the density of states at the Fermi energy:

$$\mathcal{N}(0) \simeq \frac{1}{2\pi} \frac{m_e^*}{\hbar} \frac{\delta}{1-\delta}. \quad (5.59)$$

In fact, we can rewrite Eq. (5.57) as:

$$T_{CDW}(\delta) \simeq \frac{4e^\gamma}{\pi} T^*(0) \left[ 1 - \left( \frac{\delta}{\delta_c} \right)^{\frac{3}{2}} \right] e^{-\frac{1}{4\pi} \left( \frac{\hbar\Omega a_0}{e^2} \right)^2 \frac{M}{m_e^*} \frac{1-\delta}{\delta}} \quad (5.60)$$

where  $\Omega = \Omega(Q_1)$ . The sudden vanishing of the renormalized longitudinal phonon frequency at the critical temperature gives rise to a macroscopically occupied phonon modes with wavenumbers  $Q_i$  which, physically, corresponds to a static periodic distortion of the lattice displacements  $u_i(\vec{r})$  [161]. Accordingly, we may introduce the order parameters:

$$\Delta_{CDW}(Q_i) = \frac{g(Q_i)}{V_u} \left[ \langle \hat{b}_i(\vec{Q}_i) \rangle + \langle \hat{b}_i^\dagger(-\vec{Q}_i) \rangle \right]. \quad (5.61)$$

Since  $\langle \hat{b}_i^\dagger(-\vec{Q})_i \rangle = \langle \hat{b}_i(\vec{Q}_i) \rangle$  we have:

$$\Delta_{CDW}(Q_i) = \frac{2g(Q_i)}{V_u} \langle \hat{b}_i(\vec{Q}_i) \rangle. \quad (5.62)$$

Evidently we also have:

$$\Delta_{CDW}(Q_1) = \Delta_{CDW}(Q_2) \equiv \Delta_{CDW}. \quad (5.63)$$

Moreover, both the phonons with wavenumbers  $\pm\vec{Q}_i$  are involved, so that the order parameter may be assumed to be a real number. According to Eq. (5.9) the resulting lattice displacement distortions are:

$$\Delta u_i(\vec{r}) = \langle u_i(\vec{r}) \rangle = \sqrt{\frac{\hbar}{2M\Omega(Q_i)N_u}} \frac{2\Delta_{CDW}V_u}{g(Q_i)} \cos(\vec{Q}_i \cdot \vec{r}). \quad (5.64)$$

To determine the order parameter we minimize the condensation energy per unit cell. In the mean field approximation the effective Hamiltonian Eq. (5.14) reads:

$$\begin{aligned} \hat{H}_{eff} = & \frac{V_u^2 \Delta_{CDW}^2 \hbar \Omega(Q_1)}{2g^2(Q_1)} + \sum_{\vec{k}, \sigma} \left( \varepsilon_{\vec{k}}^{(e)} - \varepsilon_F^{(e)} \right) \hat{\psi}_e^\dagger(\vec{k}, \sigma) \hat{\psi}_e(\vec{k}, \sigma) \\ & + \frac{1}{V_u} \sum_{\vec{k}, \sigma} 2g(Q_1) \left\{ \langle \hat{b}_1(-\vec{Q}_1) \rangle \hat{\psi}_e^\dagger(\vec{k} - \vec{Q}_1, \sigma) \hat{\psi}_e(\vec{k}, \sigma) \right. \\ & \left. + \langle \hat{b}_1(+\vec{Q}_1) \rangle \hat{\psi}_e^\dagger(\vec{k} + \vec{Q}_1, \sigma) \hat{\psi}_e(\vec{k}, \sigma) \right\}, \end{aligned} \quad (5.65)$$

where, for definiteness, we are considering the charge density wave instability at  $q = Q_1$ . Using Eq. (5.62) we get:

$$\begin{aligned} \hat{H}_{eff} = & \frac{V_u^2 \Delta_{CDW}^2 \hbar \Omega(Q_1)}{2g^2(Q_1)} + \sum_{\vec{k}, \sigma} \left( \varepsilon_{\vec{k}}^{(e)} - \varepsilon_F^{(e)} \right) \hat{\psi}_e^\dagger(\vec{k}, \sigma) \hat{\psi}_e(\vec{k}, \sigma) \\ & + \Delta_{CDW} \sum_{\vec{k}, \sigma} \left\{ \hat{\psi}_e^\dagger(\vec{k} - \vec{Q}_1, \sigma) \hat{\psi}_e(\vec{k}, \sigma) + \hat{\psi}_e^\dagger(\vec{k} + \vec{Q}_1, \sigma) \hat{\psi}_e(\vec{k}, \sigma) \right\}. \end{aligned} \quad (5.66)$$

Let us consider the nodal quasielectrons in sectors (I) and (II) that are connected by the nesting wavevectors  $\pm\vec{Q}_1$ . We label by subscripts 1 and 2 the quasielectrons in the Fermi arc sectors (I) and (II) respectively. We consider only states near the Fermi level. After making use of Eq. (5.44) we get:

$$\begin{aligned} \hat{H}_{eff} \simeq & \frac{V_u^2 \Delta_{CDW}^2 \hbar \Omega(Q_1)}{2g^2(Q_1)} \\ & + V_u \frac{\mathcal{N}(0)}{2} \sum_{\sigma} \int d\varepsilon_{\vec{k}}^{(e)} \xi_{\vec{k}} \left[ \hat{\psi}_1^\dagger(\vec{k}, \sigma) \hat{\psi}_1(\vec{k}, \sigma) - \hat{\psi}_2^\dagger(\vec{k}, \sigma) \hat{\psi}_2(\vec{k}, \sigma) \right] \\ & + V_u \frac{\mathcal{N}(0)}{2} \Delta_{CDW} \sum_{\sigma} \int d\varepsilon_{\vec{k}}^{(e)} \left[ \hat{\psi}_2^\dagger(\vec{k}, \sigma) \hat{\psi}_1(\vec{k}, \sigma) + \hat{\psi}_1^\dagger(\vec{k}, \sigma) \hat{\psi}_2(\vec{k}, \sigma) \right], \end{aligned} \quad (5.67)$$

where  $\xi_{\vec{k}} = \varepsilon_{\vec{k}}^{(e)} - \varepsilon_F^{(e)}$ . Of course, we must add also the contribution due to the quasielectrons in the Fermi arc sectors (III) and (IV). The final result can be written as:

$$\begin{aligned} \hat{H}_{eff} &\simeq \frac{V_u^2 \Delta_{CDW}^2 \hbar \Omega(Q_1)}{2g^2(Q_1)} \\ &+ V_u \mathcal{N}(0) \sum_{\sigma} \int d\varepsilon_{\vec{k}}^{(e)} \xi_{\vec{k}} \left[ \hat{\psi}_1^{\dagger}(\vec{k}, \sigma) \hat{\psi}_1(\vec{k}, \sigma) - \hat{\psi}_2^{\dagger}(\vec{k}, \sigma) \hat{\psi}_2(\vec{k}, \sigma) \right] \\ &+ V_u \mathcal{N}(0) \Delta_{CDW} \sum_{\sigma} \int d\varepsilon_{\vec{k}}^{(e)} \left[ \hat{\psi}_2^{\dagger}(\vec{k}, \sigma) \hat{\psi}_1(\vec{k}, \sigma) + \hat{\psi}_1^{\dagger}(\vec{k}, \sigma) \hat{\psi}_2(\vec{k}, \sigma) \right]. \end{aligned} \quad (5.68)$$

The Hamiltonian Eq. (5.68) can be diagonalized by means of the Bogoliubov-Valatin canonical transformations [162, 163]:

$$\begin{aligned} \hat{\psi}_1(\vec{k}, \sigma) &= \cos\left(\frac{\theta_{\vec{k}}}{2}\right) \hat{\psi}_1(\vec{k}, \sigma) - \sin\left(\frac{\theta_{\vec{k}}}{2}\right) \hat{\psi}_2(\vec{k}, \sigma) \\ \hat{\psi}_2(\vec{k}, \sigma) &= \sin\left(\frac{\theta_{\vec{k}}}{2}\right) \hat{\psi}_1(\vec{k}, \sigma) + \cos\left(\frac{\theta_{\vec{k}}}{2}\right) \hat{\psi}_2(\vec{k}, \sigma). \end{aligned} \quad (5.69)$$

After some algebra we find:

$$\begin{aligned} \hat{H}_{eff} &\simeq \frac{V_u^2 \Delta_{CDW}^2 \hbar \Omega(Q_1)}{2g^2(Q_1)} + V_u \mathcal{N}(0) \sum_{\sigma} \int d\varepsilon_{\vec{k}}^{(e)} \\ &\left\{ \left[ \xi_{\vec{k}} \cos \theta_{\vec{k}} - \Delta_{CDW} \sin \theta_{\vec{k}} \right] \left[ \hat{\psi}_1^{\dagger}(\vec{k}, \sigma) \hat{\psi}_1(\vec{k}, \sigma) - \hat{\psi}_2^{\dagger}(\vec{k}, \sigma) \hat{\psi}_2(\vec{k}, \sigma) \right] \right. \\ &\left. + \left[ \xi_{\vec{k}} \sin \theta_{\vec{k}} + \Delta_{CDW} \cos \theta_{\vec{k}} \right] \left[ \hat{\psi}_2^{\dagger}(\vec{k}, \sigma) \hat{\psi}_1(\vec{k}, \sigma) + \hat{\psi}_1^{\dagger}(\vec{k}, \sigma) \hat{\psi}_2(\vec{k}, \sigma) \right] \right\}. \end{aligned} \quad (5.70)$$

To diagonalize the effective Hamiltonian we choose the angles  $\theta_{\vec{k}}$  such that:

$$\xi_{\vec{k}} \sin \theta_{\vec{k}} + \Delta_{CDW} \cos \theta_{\vec{k}} = 0, \quad (5.71)$$

or equivalently:

$$\tan \theta_{\vec{k}} = - \frac{\Delta_{CDW}}{\xi_{\vec{k}}}. \quad (5.72)$$

From Eq. (5.72) we get:

$$\cos \theta_{\vec{k}} = \frac{\xi_{\vec{k}}}{\sqrt{\xi_{\vec{k}}^2 + \Delta_{CDW}^2}}, \quad \sin \theta_{\vec{k}} = - \frac{\Delta_{CDW}}{\sqrt{\xi_{\vec{k}}^2 + \Delta_{CDW}^2}}. \quad (5.73)$$

Therefore we have:

$$\begin{aligned} \hat{H}_{eff} &\simeq \frac{V_u^2 \Delta_{CDW}^2}{g^2(Q_1)} \frac{\hbar \Omega(Q_1)}{2} \\ &+ V_u \mathcal{N}(0) \sum_{\sigma} \int d\varepsilon_{\vec{k}}^{(e)} \sqrt{\xi_{\vec{k}}^2 + \Delta_{CDW}^2} \left[ \hat{\psi}_1^{\dagger}(\vec{k}, \sigma) \hat{\psi}_1(\vec{k}, \sigma) - \hat{\psi}_2^{\dagger}(\vec{k}, \sigma) \hat{\psi}_2(\vec{k}, \sigma) \right]. \end{aligned} \quad (5.74)$$

Introducing the energy measured relative to the Fermi energy:

$$\tilde{\varepsilon}_k^{(e)} = \text{sign}(k - k_F^{(e)}) \sqrt{\xi_k^2 + \Delta_{CDW}^2} , \quad (5.75)$$

we may rewrite the Hamiltonian as:

$$\begin{aligned} \hat{H}_{eff} &\simeq \frac{V_u^2 \Delta_{CDW}^2}{g^2(Q_1)} \frac{\hbar \Omega(Q_1)}{2} \\ &+ V_u \mathcal{N}(0) \sum_{\sigma} \int d\varepsilon_k^{(e)} \tilde{\varepsilon}_k^{(e)} \left[ \hat{\psi}_1^\dagger(\vec{k}, \sigma) \hat{\psi}_1(\vec{k}, \sigma) + \hat{\psi}_2^\dagger(\vec{k}, \sigma) \hat{\psi}_2(\vec{k}, \sigma) \right] . \end{aligned} \quad (5.76)$$

The Hamiltonian Eq. (5.76) shows that in the charge density wave state the spectrum of the nodal quasielectron excitations develops a gap  $\Delta_{CDW}$ . The opening of the gap leads, in turns, to the lowering of the electron energy:

$$\Delta E_c^{(e)} \simeq 2 V_u \mathcal{N}(0) \int_0^{\varepsilon_c} d\xi_{\vec{k}} \left[ \xi_{\vec{k}} - \sqrt{\xi_{\vec{k}}^2 + \Delta_{CDW}^2} \right] . \quad (5.77)$$

A straightforward integration gives:

$$\Delta E_c^{(e)} \simeq 2 V_u \mathcal{N}(0) \left\{ \frac{\varepsilon_c}{2} - \frac{1}{2} \varepsilon_c \sqrt{\varepsilon_c^2 + \Delta_{CDW}^2} - \frac{\Delta_{CDW}^2}{2} \ln \left[ \frac{\varepsilon_c + \sqrt{\varepsilon_c^2 + \Delta_{CDW}^2}}{\Delta_{CDW}} \right] \right\} . \quad (5.78)$$

In the weak coupling limit  $\Delta_{CDW} \ll \varepsilon_c$  we obtain:

$$\Delta E_c^{(e)} \simeq 2 V_u \mathcal{N}(0) \left\{ - \frac{\Delta_{CDW}^2}{4} - \frac{\Delta_{CDW}^2}{2} \ln \left( \frac{2\varepsilon_c}{\Delta_{CDW}} \right) \right\} . \quad (5.79)$$

The total condensation energy is therefore:

$$\Delta E_c \simeq \frac{V_u^2 \Delta_{CDW}^2}{g^2(Q_1)} \frac{\hbar \Omega(Q_1)}{2} + 2 V_u \mathcal{N}(0) \left\{ - \frac{\Delta_{CDW}^2}{4} - \frac{\Delta_{CDW}^2}{2} \ln \left( \frac{2\varepsilon_c}{\Delta_{CDW}} \right) \right\} . \quad (5.80)$$

Minimizing the condensation energy with respect to  $\Delta_{CDW}$  we get:

$$\Delta_{CDW} \simeq 2 \varepsilon_c e^{-\frac{\hbar \Omega(Q_1) V_u}{2g^2(Q_1) \mathcal{N}(0)}} . \quad (5.81)$$

The whole approach can be extended easily to finite temperatures. In fact, the thermodynamics has been worked out for the first time in Ref. [164]. It can be seen that the thermodynamics of the phase transition and the temperature dependence of the charge density wave gap are the same as those in the s-wave weak coupling BCS superconductors [161, 165]. Therefore, for the critical temperature one finds:

$$k_B T_{CDW} \simeq \frac{e^\gamma}{\pi} \Delta_{CDW} \simeq \frac{2e^\gamma}{\pi} \varepsilon_c e^{-\frac{\hbar \Omega(Q_1) V_u}{2g^2(Q_1) \mathcal{N}(0)}} . \quad (5.82)$$

The temperature dependence of the gap is given by:

$$\begin{aligned} \ln \left( \frac{T}{T_{CDW}} \right) &\simeq - \int_0^\infty dx \left\{ \frac{1}{x} \tanh\left(\frac{x}{2}\right) - \frac{1}{\sqrt{x^2 + z^2}} \tanh\left(\frac{\sqrt{x^2 + z^2}}{2}\right) \right\} , \\ z &= \frac{\Delta_{CDW}(T)}{k_B T} . \end{aligned} \quad (5.83)$$

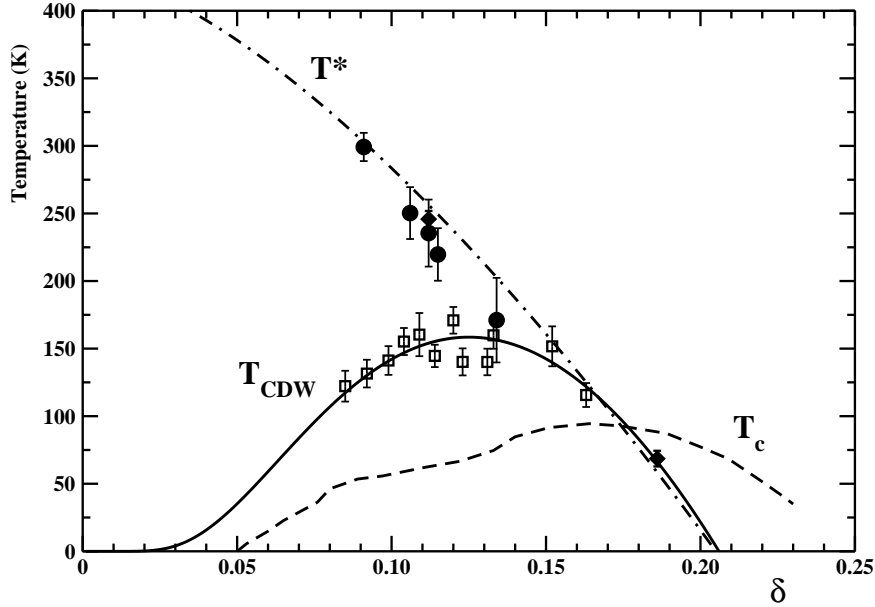


Figure 19: The phase diagram in the pseudogap region for YBCO. The dashed curve is the superconductive critical temperature  $T_c$ . Full circles and diamonds are the pseudogap temperatures  $T^*$  as determined by neutron diffraction measurement and resonant ultrasound respectively. The dot-dashed line is Eq. (5.58) with  $T^*(0)$  given by Eq. (5.85). The charge density wave critical temperatures  $T_{CDW}$  (open squares) have been estimated by means of X-ray diffraction experiments. The full curve is our Eq. (5.84).

It is noteworthy to emphasize that the charge density wave critical temperature given by Eq. (5.82) does not agree with Eq. (5.56). In fact, the argument of the exponential in Eq. (5.56) is one half the one in Eq. (5.82). This means that Eq. (5.56) overestimates by a considerable amount the charge density wave critical temperature. This difference resides into the fact that in the estimate Eq. (5.56) one does not include the quasielectron correlations built in the ground state wavefunction. On the other hand, Eq. (5.82) includes these correlation effects, albeit in the mean field approximation.

It is interesting to display explicitly the doping dependence of the charge density wave critical temperature. Instead of Eq. (5.60), now we have:

$$T_{CDW}(\delta) \simeq \frac{4e^\gamma}{\pi} T^*(0) \left[ 1 - \left( \frac{\delta}{\delta_c} \right)^{\frac{3}{2}} \right] e^{-\frac{1}{2\pi} \left( \frac{\hbar\Omega(Q_1)a_0}{e^2} \right)^2 \frac{M}{m_e^*} \frac{1-\delta}{\delta}}. \quad (5.84)$$

Eq. (5.84) can be contrasted to experimental observations. To this end, in Fig. 19 we display the observed phase diagram for YBCO in the pseudogap region. The dashed curve outlines the doping dependence of the critical temperature  $T_c(\delta)$ . The data for the critical superconductive temperature have been taken from Fig. 3 in Ref. [166]. The pseudogap temperatures  $T^*$  have been determined by neutron diffraction measurement (full circles) and resonant ultrasound (full diamonds). The data have been taken from Fig. 3 in Ref. [167]. Note that the data are in satisfying agreement with our Eq. (5.58), displayed as the dot-dashed line in Fig. 19, by assuming:

$$T^*(0) \simeq 430 \text{ K}. \quad (5.85)$$

As regard the charge density wave critical temperature, the onset of charge order are detected in X-ray diffraction below the critical temperature  $T_{CDW}$ . The data (open squares)



have been taken from Fig. 10 in Ref. [141] and Table I in Ref. [142]. To compare our theoretical estimate of the charge density critical temperature, Eq. (5.84), we used the numerical values of the model parameters and  $T^*(0)$  given in Eq. (5.85). The reduced atomic mass of the  $Cu$  and  $O$  ions is evaluated by Eq. (5.3) using  $M_{Cu} \simeq 63.5 M_P$  and  $M_O \simeq 16 M_P$ ,  $M_P$  being the proton mass. To match the data we used:

$$\hbar \Omega(Q_1) \simeq 35.5 \text{ meV} \quad (5.86)$$

corresponding to a frequency  $\sim 10 \text{ THz}$ , which compares well with the observed bond-stretching frequencies in cuprates. Indeed, Fig. 19 shows that Eq. (5.84) is in satisfying agreement with the charge density wave critical temperature data. In particular we see that our theoretical calculations reproduce the shallow maximum at  $\delta \simeq 0.12$  displayed by the data. It is worth to note that the charge density wave long range order in cuprates seems to set in in a rather small hole doping range,  $0.08 \lesssim \delta \lesssim 0.17$ , around the charge density wave critical temperature maximum at  $\delta \simeq 0.12$ . In our opinion this could be easily explained if the coherence length in charge density wave cannot grow too much. Indeed, the coherence length may be hindered by crystalline imperfections and defects which are inevitably present in hole doped cuprates. In general, the appearance of the energy gap  $\Delta_{CDW}$  also leads to a finite coherence length  $\xi_{CDW}$ . The expression of the coherence length is the same as the BCS coherence length and, at zero temperature, it is given by:

$$\xi_{CDW} \simeq \frac{\hbar v_F^{(e)}}{\pi \Delta_{CDW}}, \quad (5.87)$$

where  $v_F^{(e)}$  is the quasielectron Fermi velocity. From Eq. (5.87) we may easily infer the doping dependence of the charge density wave coherence length:

$$\xi_{CDW}(\delta) \simeq \frac{4 a_0}{\sqrt{2\pi}} \sqrt{1 - \delta} \frac{t}{\Delta_{CDW}(\delta)}, \quad (5.88)$$

where, according to Eq. (5.82):

$$\Delta_{CDW}(\delta) \simeq \frac{\pi}{e\gamma} k_B T_{CDW}(\delta). \quad (5.89)$$

In Fig. 20 we show the doping dependence of the coherence length and compare with available data for YBCO and  $Bi_2Sr_{2-x}La_xCuO_{6+\delta}$  (Bi-2201). The data for YBCO have been taken from Table I of Ref. [142] where the doping dependence of the charge density wave order was analyzed with a bulk-sensitive high-energy x-ray study. The data for Bi-2201 have been taken from Table 1 of Ref. [146] where charge order was observed by combining resonant x-ray scattering, scanning-tunneling microscopy, and angle resolved photoemission spectroscopy. To match the experimental data we scaled  $\xi_{CDW}(\delta)$  by a factor 2.1 and 0.85 for YBCO and Bi-2201 respectively. In any case, we see that in the doping range  $0.08 \lesssim \delta \lesssim 0.17$  the coherence length does not vary appreciably with the doping. However, outside that doping range  $\xi_{CDW}$  increases suddenly. Now, it is reasonable to assume that the presence of lattice imperfections and defects tend to impede the grow of the coherence length beyond a certain length. Therefore, outside the small hole doping range around  $\delta \simeq 0.12$  the charge order cannot develop as a true long-range order, but it should manifest itself through short-range correlations.

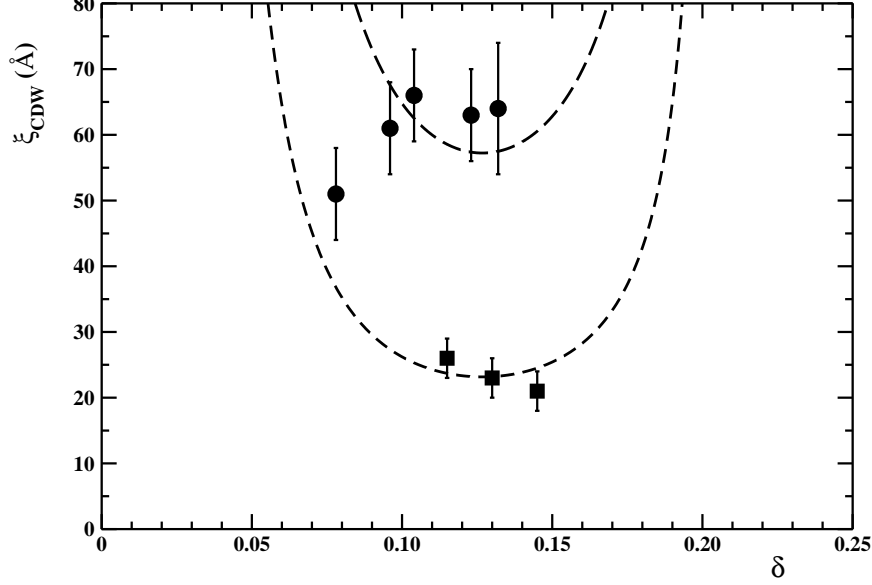


Figure 20: The charge density wave coherence length versus the hole doping for YBCO (full circles) and Bi-2201 (full squares). The dashed curves correspond to Eq. (5.88) scaled by a factor 2.1 and 0.85 for YBCO and Bi-2201 respectively.

Let us consider the small Peierls lattice deformations which, after using Eq. (5.64), can be written as:

$$\Delta \vec{u}(\vec{r}) = \langle \vec{u}(\vec{r}) \rangle \simeq \sqrt{\frac{\hbar}{2M\Omega(Q)N_u}} \frac{2\Delta_{CDW}V_u}{g(Q)} \left[ \cos(Qx) \hat{x} + \cos(Qy) \hat{y} \right], \quad (5.90)$$

where we used

$$\vec{Q}_1 = (Q, 0), \quad \vec{Q}_2 = (0, Q), \quad Q \simeq \sqrt{2} k_F^{(e)}, \quad (5.91)$$

and

$$g(Q_1) \simeq g(Q_2) \equiv g(Q), \quad \Omega(Q_1) \simeq \Omega(Q_2) \equiv \Omega(Q). \quad (5.92)$$

The charge-order wavenumber vectors are conventionally expressed in terms of the reciprocal lattice constant:

$$a_0^* = \frac{2\pi}{a_0} \quad (5.93)$$

as:

$$\vec{Q}_1 = a_0^*(H, 0), \quad \vec{Q}_2 = a_0^*(0, K). \quad (5.94)$$

After using Eq. (4.11), we find:

$$H = K \simeq \sqrt{\frac{1-\delta}{\pi}}. \quad (5.95)$$

From Eq. (5.95) it follows that  $Q$  smoothly decreases upon increasing the hole doping  $\delta$  in fair agreement with observations. However, the observed charge-order wavenumbers is not much more than half the value as here determined. This is, mainly, due to our over exemplified model which leads to an overestimate of the nesting wavevectors of the nodal quasielectron Fermi circle.

In our approach the charge density wave always exhibits wavenumber vectors parallel to the planar Cu-O bonds. It is interesting to note that in Ref. [138] it is provided the first thermodynamic signature of the charge-order phase transition in underdoped YBCO. In particular, the comparison of different acoustic modes indicated that the charge modulation were biaxial, namely directed both along the  $\hat{x}$  and  $\hat{y}$  axes. Remarkably, in Ref.[148], by using resonant X-ray scattering to resolve the charge modulations in the two cuprate families Bi-2201 and YBCO in the underdoped region, it was established that the charge modulations run parallel to the copper-oxygen bond directions. Moreover the pattern of the charge density wave turned out to be compatible with Eq. (5.90).

Finally, it is worthwhile to estimate quantitatively the amplitude of the atomic planar displacement induced by the charge density wave. Let us consider the small Peierls lattice deformations which, after using Eq. (5.64), can be written as:

$$\Delta u \simeq \sqrt{\frac{\hbar}{2M\Omega(Q)}} \frac{2\Delta_{CDW}V_u}{g(Q)}. \quad (5.96)$$

Ref. [135] reported the X-ray diffraction study of a detwinned single crystal of YBCO with hole concentration per planar Cu  $\delta \simeq 0.12$  ( $T_c \simeq 67 K$ ). The authors of Ref. [135] by using high-energy X-ray diffraction showed that a charge density wave develops in the normal state of superconducting YBCO below the critical temperature  $T_{CDW} \simeq 135 K$ . In particular, from the intensity ratio between the incommensurate satellite peaks and Bragg reflection peaks these authors were able to estimate the amplitude of the lattice distortion in the charge density wave. In fact, they reported the upper limit [135]:

$$\frac{\Delta u}{a_0} \lesssim 10^{-3}. \quad (5.97)$$

To determine  $\Delta u$ , we need the charge density wave gap. Since for the YBCO crystal used in Ref. [135] the charge density wave critical temperature was  $T_{CDW} \simeq 135 K$ , using Eq. (5.89) we find:

$$\Delta_{CDW} \simeq 20.5 \text{ meV}. \quad (5.98)$$

Once we known the charge density wave gap, we may easily evaluate the lattice displacement by Eq. (5.96):

$$\frac{\Delta u}{a_0} \simeq 1.8 \cdot 10^{-3}, \quad (5.99)$$

which, indeed, is in reasonable agreement with Eq. (5.97).

### 5.3 Competition between charge density wave and superconductivity

We said that there is growing evidence of a charge order existing in the pseudogap state of several cuprate families. Actually, charge density wave order and superconductivity are competing phases. It is widely believed that understanding the interplay between superconductivity and charge order is essential to clarify the origin of the high temperature superconductivity in cuprate materials. In fact, there are several experimental observations showing that superconductivity weakens the charge density order and, conversely,

the charge order tends to weaken superconductivity. Moreover, application of a magnetic field restores the charge density wave amplitude below the superconductive critical temperature, while it has no appreciable effect for temperatures above the critical temperature. The effects of applied magnetic fields on the charge density wave order will be discussed in the next Section. In the present Section we focus on the competition between charge density wave and superconductivity.

As we have already discussed, the charge-order state is driven by the nodal Fermi arc instability. Moreover, we know that nodal quasielectron excitations are possible if the paired holes are phase disordered. Therefore, by using an argument similar to that employed in Sect. 4.3, we see that the number of the nodal quasielectron excitations is reduced in the superconductive region by:

$$\frac{n_n(T)}{n_s(0)} \simeq 1 - e^{-b' \left[ \frac{1}{\sqrt{1-T/T_c}} - 1 \right]}, \quad T \leq T_c. \quad (5.100)$$

Qualitatively, it is evident that below the superconductive critical temperature the number of available nodal quasielectron excitations decreases thereby suppressing the charge density wave gap. Since the fully microscopic approach becomes difficult, the simplest way to determine quantitatively the expected depletion of the charge density wave gap in the superconductive phase is to deal with the free energy functional within the Ginzburg-Landau theory. The free energy functional appropriate to the regime of small charge density wave order parameter  $\Delta(\vec{r})$  can be written as:

$$F_{CDW}[\Delta] \simeq F[0] + \int d\vec{r} \left\{ a(T) |\Delta(\vec{r})|^2 + b(T) |\Delta(\vec{r})|^4 \right\}. \quad (5.101)$$

In Eq. (5.101) we are neglecting the energy associated with the spatial variation of the order parameter. Indeed, we are mainly interested in the limit of homogeneous charge density order parameter where  $\Delta(\vec{r})$  reduces to  $\Delta_{CDW}$ . The two coefficients in the Ginzburg-Landau free energy functional can be evaluated near the transition temperature  $T_{CDW}$  within the weak coupling s-wave BCS microscopic theory. One finds (see, eg, Ref. [46]):

$$a(T) \simeq \mathcal{N}(0) \left( \frac{T}{T_{CDW}} - 1 \right) \quad (5.102)$$

and

$$b(T) \simeq \mathcal{N}(0) \frac{7 \zeta(3)}{8 \pi^2 k_B^2 T_{CDW}^2}, \quad (5.103)$$

where  $\zeta(z)$  is the Euler-Riemann zeta function [121]. Note that, within this approximation, the coefficient  $b$  is almost independent on the temperature while  $a(T)$  is positive above the charge density critical temperature, vanishes at  $T_{CDW}$ , and it becomes negative below the transition temperature.

The temperature dependence of the order parameter is obtained from the equilibrium condition:

$$\frac{\delta F_{CDW}[\Delta]}{\delta \Delta(\vec{r})} = 0. \quad (5.104)$$

For homogeneous order parameter, above the transition temperature the minimum of the free energy functional is at  $\Delta = 0$ . For temperatures below  $T_{CDW}$  we get instead:

$$\Delta^2(T) \simeq \frac{8 \pi^2}{7 \zeta(3)} k_B^2 T_{CDW}^2 \left[ 1 - \frac{T}{T_{CDW}} \right]. \quad (5.105)$$

It can easily be seen that, as expected, Eq. (5.105) agrees with the solution of the BCS Eq. (5.83) at least for temperatures not too far from the charge density wave critical temperature.

In the superconductive region we may take care of the depletion of the nodal quasielectron excitations by allowing the Ginzburg-Landau parameter  $a(T)$  to be reduced according to Eq. (5.100). Therefore, we are led to assume:

$$a(T) \simeq \mathcal{N}(0) \left( \frac{T}{T_{CDW}} - 1 \right) , \quad T_c \leq T \leq T_{CDW} \quad (5.106)$$

$$a(T) \simeq \mathcal{N}(0) \left\{ 1 - e^{-b' \left[ \frac{1}{\sqrt{1-T/T_c}} - 1 \right]} \right\} \left( \frac{T}{T_{CDW}} - 1 \right) , \quad T \leq T_c$$

while the parameter  $b$  is still kept temperature independent. Correspondingly, for homogeneous order parameter and for temperatures below  $T_{CDW}$  we obtain:

$$\Delta(T) \simeq \Delta_{CDW}(T) , \quad T_c \leq T \leq T_{CDW} \quad (5.107)$$

$$\Delta(T) \simeq \sqrt{1 - e^{-b' \left[ \frac{1}{\sqrt{1-T/T_c}} - 1 \right]}} \Delta_{CDW}(T) , \quad T \leq T_c$$

where  $\Delta_{CDW}(T)$  is the the solution of Eq. (5.83). In fact, Eq. (5.107) implies that the charge density wave gap is quickly reduced in the superconductive phase in qualitative agreements with observations. For illustrative purposes, we show here how our results offer a consistent interpretation of the recent angle resolved photoemission spectroscopy studies presented in Ref. [37]. These authors examined the momentum-resolved single particle spectra of hole doped cuprate Bi-2212 in the optimal doping region by utilizing a low-energy laser source which allowed to obtain high-quality spectra with very sharp line shapes. The high quality of the data allowed to determine the energy gap as the peak energy of the single particle spectra. In Fig. 21 we report the temperature dependence of the spectral gap for optimal doped Bi-2212 ( $T_c \simeq 92 K$ ). The data have been extracted from Fig. 2, panel a), of Ref. [37]. The data correspond to  $\varepsilon_{peak}$  at  $\phi \simeq 24^\circ$ , where  $\phi$  gives the direction of the Fermi wavevector as defined in Fig. 3, panel d), of Ref. [37]. As it is evident from Fig. 21, the spectral energy gap does not close at the superconductive critical temperature  $T_c \simeq 92 K$ , but it survives beyond  $T_c$  until the higher temperature  $T_{pair} \simeq 137 K$ . According to Ref. [37] the spectral gap  $\varepsilon_{peak}$  is interpreted as the energy pairing-gap in the nodal region persisting even above the superconductive critical temperature, and vanishing only at the critical temperature  $T_{pair}$  far above  $T_c$ . Moreover, this pairing-gap seems to evolve with temperature according to the weak coupling s-wave BCS gap function with onset temperature  $T_{pair}$ . Actually, this interpretation is in contradiction with several observations which pointed to a phase-incoherent superconductivity in the pseudogap region. In order to reach a sensible picture of these puzzling results we must assume that the temperature  $T_{pair}$  signals the onset of charge order,  $T_{pair} = T_{CDW}$ . In fact, we have already seen in Sect. 5.2 that long-range charge order in cuprates sets in a small hole doping range near the optimal doped region (see Fig. 19). Note that within this interpretation we may explain naturally both the absence of the gapless Fermi arcs above the superconductive temperature and the presence of Bogoliubov quasiparticle low-lying

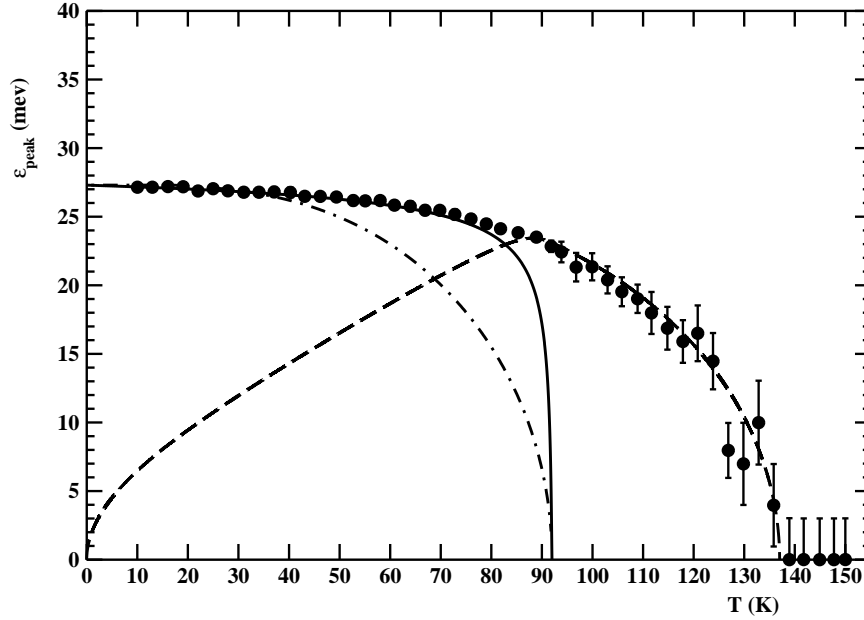


Figure 21: The spectral peak energy versus the temperature for optimal doped Bi-2212,  $T_c \simeq 92\text{ K}$ . The data have been extracted from Fig. 2, panel a), of Ref. [37]. The solid line is the nodal gap Eq. (4.21) with  $b \simeq 0.08$  and  $\Delta_{\text{nodal}}(0) \simeq 27.3\text{ meV}$ . For comparison we also display the weak coupling d-wave BCS gap (dot-dashed line). The dashed curve is the charge density wave gap Eq. (5.107) with  $\Delta_{\text{CDW}}(0) \simeq 27.0\text{ meV}$ ,  $T_{\text{CDW}} \simeq 137\text{ K}$ , and  $b' \simeq 1.0$ .

excitations [37] due to the charge density wave gapped state. In addition, the temperature evolution of the spectral gap as implied by Eq. (5.107) is in satisfying agreement with experimental data for temperatures above the superconductive critical temperature  $T_c$  (see the dashed line in Fig. 21). In the superconductive region the charge density wave gap is rapidly suppressed. In this region the observed single-particle gap is caused by the nodal gap as discussed at length in Sect. 4.1. Remarkably, the thermal evolution of the nodal gap, Eq. (4.21), is quite consistent with the data at least for temperatures not too close to the superconductive critical temperature (see the full curve in Fig. 21). Near the critical temperature  $T_c$  there is competition between the two gaps, so that the spectral gap evolves smoothly from the nodal gap to the charge density gap.

## 5.4 Effects of the magnetic field

Several experimental observations indicated that the charge density wave is unaffected by applied magnetic fields in the normal state. In fact, for temperatures above the superconductive critical temperature  $T_c$ , a magnetic field applied perpendicular to the  $\text{CuO}_2$  plane has no appreciable effects. However, in the superconductive region  $T < T_c$  an applied magnetic field causes an increase of the intensity of the charge density wave signal. The magnetic field also seem to make the charge density wave order more coherent. These experimental observations are usually interpreted as a clear evidence for competition between charge density wave and superconducting orders.

Let us, now, discuss in our model the effects of the magnetic field on the charge density wave. It will be shown that the effects of magnetic fields on the charge density wave

ground state are sizable in the superconductive region, while they are negligible small in the normal region. Indeed, in the normal non-superconductive phase the magnetic field acts on the spins of the nodal quasielectrons only since, in general, the effect of spin-orbit interactions are negligible. The Zeeman splitting of the quasielectron energy at the Fermi level will reduce the pairing interaction and eventually it leads to a non-condensate metallic state where the charge density wave energy gap is driven to zero. It turns out that the problem is quite similar to the influence of applied external fields on the Peierls instability in quasi one-dimensional conductors. As we said, there is a formal resemblance between the energy gap in the Peierls state and the energy gap in weak coupling s-wave BCS superconductors. In fact, in analogy to the calculations in the theory of superconductivity [168] one finds [169]:

$$\ln \frac{T_{CDW}(H)}{T_{CDW}} + \Re \psi \left( \frac{1}{2} + i \frac{\mu_B H}{2\pi k_B T_{CDW}(H)} \right) - \psi \left( \frac{1}{2} \right) = 0 , \quad (5.108)$$

where  $\psi(z)$  is the digamma function [121]. In Eq. (5.108)  $T_{CDW}(H)$  is the charge density wave critical temperature in presence of a transverse magnetic field  $H$ . By expanding to the first non-trivial order in  $\mu_B H$  we find:

$$\frac{T_{CDW}(H)}{T_{CDW}} \simeq 1 + \frac{1}{8\pi^2} \psi'' \left( \frac{1}{2} \right) \left( \frac{\mu_B H}{k_B T_{CDW}} \right)^2 , \quad (5.109)$$

where the prime denotes the derivative. Using [121]:

$$\psi'' \left( \frac{1}{2} \right) = -2 (2^3 - 1) \zeta(3) , \quad (5.110)$$

we obtain:

$$\frac{T_{CDW}(H) - T_{CDW}}{T_{CDW}} \simeq -\frac{7}{4\pi^2} \zeta(3) \left( \frac{\mu_B H}{k_B T_{CDW}} \right)^2 . \quad (5.111)$$

Note that this last result can be obtained directly by repeating the calculations presented in Ref. [161] for the case in which the quasielectron spin interacts with an external magnetic field [170]. From Eq. (5.111) it follows that even for magnetic field strength up to  $H \sim 10^2 T$  the charge density wave critical temperature decreases by a few percent only. In other words, in the non-superconductive region external magnetic fields do not affect appreciably the charge density wave ground state. However, we will see in the next Section that the dependence of the charge density wave gap on the magnetic field implied by Eq. (5.111) affects in a non-trivial manner the frequencies in the quantum oscillation phenomena in underdoped cuprate superconductors.

In the superconductive region we have already remarked that the number of available nodal quasielectron excitations decreases leading to a quickly suppression of the charge density wave instability. However, there are several experimental observations suggesting the restoration of charge order in presence of applied magnetic fields. Intriguingly, in Ref. [137] the charge order in underdoped YBCO was evidenced by using the line splitting of the nuclear magnetic resonance of some of copper and oxygen sites in  $CuO_2$  planes. Observations in the superconductive region indicated a sharp set in of charge order starting above a threshold transverse magnetic field. In particular the authors of Ref. [137] found that charge order occurs for temperatures below an onset temperature  $T_{charge}$  and for magnetic fields above a threshold field  $H_{charge}$ . This threshold magnetic field turned

out to be weakly dependent on the hole doping level with values varying in the range  $H_{charge} = 9 - 15 T$ . Evidently the finite value of the threshold magnetic field implies that there is no static long-range charge order in absence of external magnetic field. This gives a clear indication for a field-dependent transition to the charge ordered state. As the authors of Ref. [137] argued, the finite threshold magnetic field can be attributed to the presence of Abrikosov vortices. A magnetic field applied perpendicular to the  $CuO_2$  planes generates vortices. Now, the vortex cores represent normal region of radius  $\xi_V$  within the superconductor. So that it is expected that the charge order fluctuations detected in the normal region above the superconductive critical temperature continue to develop at low temperatures  $T < T_c$  within the cores [137, 171]. Therefore the halos of charge order are centered on the Abrikosov vortex cores and they extend over a typical distance of order of the charge density wave coherence length  $\xi_{CDW}$ . By increasing the strength of the magnetic field more Abrikosov vortices are added. Thus, the long-range charge order may be expected to appear once these halos start to overlaps. We said in Sect. 3.5 that in our theory the upper critical magnetic field is much smaller than the Landau-Ginzburg critical magnetic field where the Abrikosov vortices become to overlap. So that we will employ the dilute vortex approximation with the density of Abrikosov vortices given by Eq. (4.74). Since the average distance between vortices is  $d_H \simeq \sqrt{\frac{\phi_0}{H}}$ , the onset of the long-range static charge density order happens when:

$$d_H \simeq \sqrt{\frac{\phi_0}{H}} \lesssim 2 \xi_{CDW} . \quad (5.112)$$

From Eq. (5.112) we easily obtain:

$$H \gtrsim \frac{\phi_0}{4 \xi_{CDW}^2} \simeq H_{charge} . \quad (5.113)$$

It is useful to estimate quantitatively our determination of the threshold magnetic field. For YBCO from Fig. 20 we see that  $\xi_{CDW} \simeq 65 \text{ \AA}$  almost independently on the hole doping around  $\delta \simeq 0.12$ . So that we get:

$$H_{charge} \simeq \frac{\phi_0}{4 \xi_{CDW}^2} \simeq 12.3 T , \quad (5.114)$$

which compares rather well with observations. The long-range charge order, which sets in the superconductive region for magnetic fields above the threshold field, persists for temperatures below a critical temperature  $T_{CDW}(H)$  (denoted as  $T_{charge}$  in Ref. [137]) that is different from the charge density wave critical temperature in the normal region. Indeed, it resulted that the maximum of  $T_{CDW}(H)$  occurs at  $\delta \simeq 0.11 - 0.12$  within the superconductive dome and the charge density wave and superconductive transition temperatures were similar,  $T_{CDW}(H) \sim T_c$ . In Fig. 22 we display the charge density wave critical temperature for YBCO in an external magnetic field above the threshold field. The data have been taken from Fig. 2, panel b, of Ref. [137]. Note that, once the long-range order is established, on increasing the magnetic field further the splitting of the nuclear magnetic resonance line saturates. This indicates that the charge density wave gap and transition temperature become field independent for magnetic fields well above the threshold field.

To determine the field-induced charge order transition temperature in our approach we



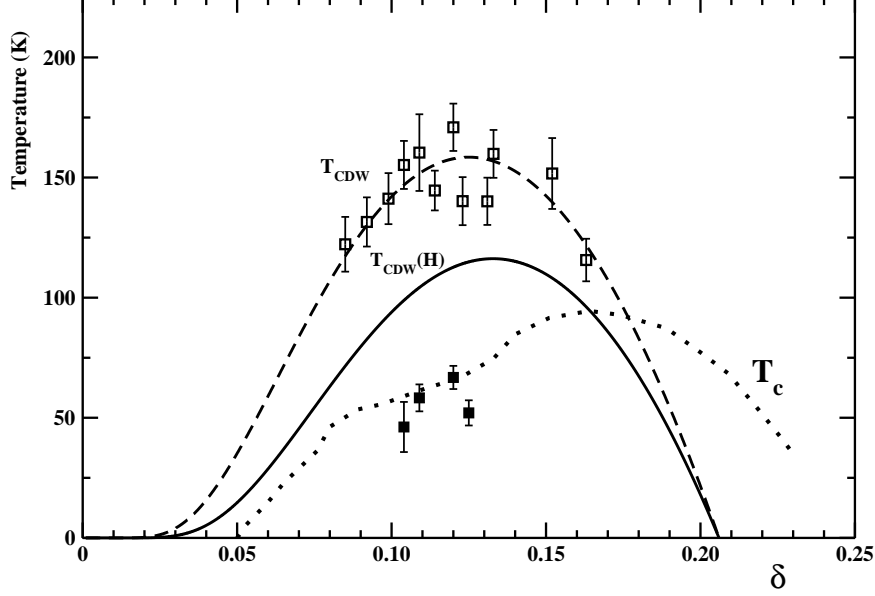


Figure 22: Charge density wave critical temperature versus the hole doping. Full squares correspond to the charge density wave critical temperature for YBCO in an external magnetic field. The data have been taken from Fig. 2, panel b, of Ref. [137]. The full line is Eq. (5.117) with  $N_{charge} \simeq 0.785$ . For comparison we also display the charge density wave critical temperatures  $T_{CDW}$  (open squares) at zero magnetic field. The dashed line is as in Fig. 19. The dotted line represents the superconducting transition temperature  $T_c$ .

could work within the Ginzburg-Landau theory as we did in Sect. 5.3. However, in the present case we need to include in the free energy functional the energy associated with the spatial variation of the order parameter and to take care of the interactions of nodal quasielectrons with the Abrikosov vortices. Actually, since we do not have at our disposal the relevant microscopic calculations we shall follow a very simple description which nevertheless should capture the essential aspects of the problem. As repeatedly alluded before, we know that the number of the nodal quasielectron excitations is strongly reduced in the superconductive region at low temperatures. The nodal quasielectron low-lying excitations relevant to the charge density wave instability are tied to the vortex cores which represent normal region within the superconductor. The nodal quasielectron excitations affect the charge density wave gap through the density of state per spin at the Fermi level. We may roughly estimate the effective density of state as:

$$\langle \mathcal{N}(0) \rangle_{eff} \simeq N_{charge} \langle \mathcal{N}(0) \rangle_{vor} , \quad (5.115)$$

where  $N_{charge}$  is the number of Abrikosov vortices in the coherence region once the long-range charge order sets in. Evidently we have:

$$N_{charge} \simeq \frac{H_{charge}}{\phi_0} \times \pi \xi_{CDW}^2 . \quad (5.116)$$

taking into account Eq. (4.53) we find that Eq. (5.57) is modified as:

$$T_{CDW}(H) \simeq \frac{4e^\gamma}{\pi} T^*(\delta) e^{-\frac{\hbar\Omega(Q_1)V_u}{2g^2(Q_1)\mathcal{N}(0)N_{charge}}} . \quad (5.117)$$

To contrast Eq. (5.117) with available experimental informations, we need to evaluate  $N_{charge}$ . Combining Eqs. (5.113) and (5.116) we reach the estimate:

$$N_{charge} \simeq \frac{\pi}{4} \simeq 0.785 . \quad (5.118)$$

In Fig. 22 we compare Eq. (5.117) with  $N_{charge}$  given by Eq. (5.118) to the available measurements. It is worthwhile to recall that charge order is sensitive to disorder, which is a prominent feature of all cuprates. So that our qualitative estimate of the charge density wave critical temperature Eq. (5.117) is intended to be valid only in a small hole doping range around  $\delta \simeq 0.12$ . We see that, indeed, the charge density critical temperature  $T_{CDW}(H)$  is reduced with respect to the charge order transition temperature in the normal region. However, our estimate is about a factor two higher with respect to the data. Nevertheless, the doping dependence turns out to be in fair agreement with observations. Note that increasing the magnetic field does not vary appreciably  $N_{charge}$  since the addition of more Abrikosov vortices is expected to do not further affect the long-range charge order. Therefore we expect that the charge density critical temperature Eq. (5.117) should saturate at strong enough magnetic field in qualitative agreement with observations. Despite the obviously simplistic nature of the description, the qualitative agreement suggests that our picture could provide a good starting point for explaining the field-induced charge order transition.

## 5.5 Quantum Oscillations

We conclude this Section by discussing the physics behind quantum oscillations in the pseudogap region of hole doped cuprates. Actually, quantum oscillations are widely studied measurements to probe the Fermi surface [102]. In fact, according to the Onsager quantization condition [98, 99] the quantum oscillation frequency is directly proportional to the cross-sectional area of the Fermi surface normal to the applied magnetic field direction. Due to this relationship, the observation of quantum oscillations is attributed to the presence of closed orbits on the Fermi surface.

A breakthrough in the area of high temperature superconductivity was the observation of quantum oscillations in cuprates<sup>14</sup>. In these experiments a strong magnetic field was applied to suppress the superconductivity, which most likely revealed the normal ground state, leading to the unambiguous identification of quantum oscillations both in the underdoped and overdoped regions. Actually, in the underdoped region the measured low oscillation frequencies revealed a Fermi surface made of small pockets as inferred by the Luttinger's theorem and the Onsager relation. More interestingly, it turned out that the area of the pocket corresponded to about a few percent of the first Brillouin zone area in sharp contrast to that of overdoped cuprates where the frequency corresponded to a large hole Fermi surface. Moreover, the clear evidence of negative Hall and Seebeck effects pointed to the conclusion that these pockets were electron-like rather than hole-like. Finally, it resulted that these pockets were associated with states near the nodal region of the Brillouin zone.

From these experimental studies we are led to suppose that the nodal quasielectron low-lying excitations are responsible for quantum oscillations in underdoped high temperature

---

<sup>14</sup>An up-to-date discussion can be found in the already quoted Refs. [93, 94, 95, 96].

cuprate superconductors. However, we have seen in Sect. 4 that the low-energy excitations of the quasielectron liquid are characterized by disconnected Fermi arcs in the first Brillouin zone as depicted in Fig. 12. According to the widely used Onsager paradigm, which is based on the quasi-classical quantization, the observation of quantum oscillations in thermodynamic quantities is possible thanks to the presence of closed orbits on the Fermi surface. Of course, since the low-lying nodal quasielectron excitations live on four disconnected Fermi arcs they cannot give rise to closed orbits. Nevertheless, when a quasiparticle Bragg diffracts at the Brillouin zone boundary it will have a momentum change given by a reciprocal lattice vector. The quasiparticle, then, can jump to a different slice of the Fermi surface. Looking at Fig. 18 we see that the nodal quasielectrons could be able to perform closed orbits if they suffer Bragg diffractions with reciprocal lattice vectors given by the nesting wavenumber vectors  $\vec{Q}_1$  and  $\vec{Q}_2$ . In general, these wavevectors are not commensurate with the reciprocal lattice of the planar  $\text{CuO}_2$  lattice. On the other hand,  $\vec{Q}_1$  and  $\vec{Q}_2$  are commensurate with the lattice distorted by the charge density wave since they are the nesting vectors triggering the charge density wave instability. We are led to conclude that Bragg reflections ensuring closed orbits are only possible in presence of the charge density wave. In the charge density wave ground state we know that the low energy nodal quasielectron excitations are gapped. Naively one expects that quantum oscillations would be suppressed due to the presence of a gap at the Fermi surface. Nevertheless, long time ago there have been measurements of Haas-van Alphen [172] and Haas-Shubnikov [173] quantum oscillation effects in transition-metal chalcogenide layer compounds which were known to have charge density wave ground states<sup>15</sup>. We see, then, that in our approach to observe quantum oscillations in underdoped cuprates it is necessary the presence of long-range charge order. As discussed before at low temperatures this is assured for applied magnetic fields above the threshold field  $H_{\text{charge}} \sim 10\text{ T}$ . In fact, quantum oscillations in hole doped cuprates are observed for magnetic field strengths well above  $H_{\text{charge}}$ . In the usual theory of quantum oscillations it is predicted that each extremal closed cross section of the Fermi surface gives rise to a well defined frequency in the oscillatory part of the thermodynamic potential, and hence in almost all thermodynamic as well as transport properties, so that each frequency appears together with its higher harmonic without mixing of frequencies. However, it has been suggested [176] that in charge density wave or spin density wave systems the interaction between Landau levels and many-body effects could produce nonlinear quantum oscillations. Indeed, we will suggest later on that the nonlinear dependence of the charge density wave order parameter on the magnetic field may be at the heart of the experimental observation of multiple quantum oscillation frequencies in underdoped high temperature cuprate superconductors.

The quantum mechanical treatment of the motion of free electrons in a uniform magnetic field leads to quantized energy levels labelled by an integer  $n$ <sup>16</sup>. The set of all levels with a given  $n$  is referred to as the  $n$ -th Landau level. The energy of Landau levels with high quantum numbers can be evaluated within the semiclassical approximation. Let  $\varepsilon_n$  be the energy of the  $n$ -th Landau level. For two-dimensional quasielectrons in a transverse uniform magnetic field  $H$ , the difference in energy of two adjacent levels is given by the

---

<sup>15</sup>A good account on transition-metal chalcogenide compounds can be found in Refs. [174, 175].

<sup>16</sup>See, e.g., Refs. [154, 177].

Planck constant divided by the period of the semiclassical closed orbit:

$$\Delta \varepsilon_n \equiv \varepsilon_{n+1} - \varepsilon_n \simeq \frac{h}{T(\varepsilon_n)} . \quad (5.119)$$

On the other hand, we have also:

$$T(\varepsilon_n) \simeq \frac{\hbar^2 c}{eH} \frac{\partial \mathcal{A}_{\vec{k}}(\varepsilon_n)}{\partial \varepsilon_n} , \quad (5.120)$$

where  $\mathcal{A}_{\vec{k}}(\varepsilon)$  is the k-space area enclosed by the closed orbit. Combining Eqs. (5.119) and (5.120) we get:

$$\varepsilon_{n+1} - \varepsilon_n \simeq \frac{2\pi eH}{\hbar c} \frac{1}{\frac{\partial \mathcal{A}_{\vec{k}}(\varepsilon_n)}{\partial \varepsilon_n}} . \quad (5.121)$$

Introducing the quasielectron cyclotron effective mass:

$$m_e^c = \frac{\hbar^2}{2\pi} \frac{\partial \mathcal{A}_{\vec{k}}(\varepsilon_n)}{\partial \varepsilon_n} , \quad (5.122)$$

we may rewrite Eq. (5.121) as:

$$\varepsilon_{n+1} - \varepsilon_n \simeq \hbar \omega_c , \quad \omega_c = \frac{eH}{m_e^c c} , \quad (5.123)$$

where  $\omega_c$  is the cyclotron frequency. It must be emphasized that the cyclotron effective mass is not, in general, the same as the quasielectron effective mass  $m_e^*$ . From Eq. (5.123) one gets:

$$\varepsilon_n \simeq \hbar \omega_c (n + \tilde{\gamma}) \quad (5.124)$$

where  $\tilde{\gamma}$  is a constant independent on  $n$ . In our simplified model the nodal quasielectrons satisfy the free electron dispersion relation. In this case it turns out that  $\tilde{\gamma} \simeq \frac{1}{2}$  [102]. Note that the Landau energy levels are highly degenerate with degeneracy:

$$g_L = \frac{V}{2\pi^2} \frac{eH}{\hbar c} . \quad (5.125)$$

We are interested in energies  $\varepsilon_n$  of the order of the Fermi energy  $\varepsilon_F^{(e)}$ . Observing that  $\hbar \omega_c \ll \varepsilon_F^{(e)}$ , to a good approximation we can write:

$$\frac{\partial \mathcal{A}_{\vec{k}}(\varepsilon_n)}{\partial \varepsilon_n} \simeq \frac{\mathcal{A}_{\vec{k}}(\varepsilon_{n+1}) - \mathcal{A}_{\vec{k}}(\varepsilon_n)}{\varepsilon_{n+1} - \varepsilon_n} . \quad (5.126)$$

Therefore, from Eq. (5.121) we are led to:

$$\mathcal{A}_{\vec{k}}(\varepsilon_{n+1}) - \mathcal{A}_{\vec{k}}(\varepsilon_n) \simeq \frac{2\pi eH}{\hbar c} , \quad (5.127)$$

which in turns gives the Onsager's relation:

$$\mathcal{A}_{\vec{k}}(\varepsilon_n) \simeq \frac{2\pi eH}{\hbar c} \left( n + \frac{1}{2} \right) . \quad (5.128)$$

The quantization condition Eq. (5.128) results in an oscillatory structure in the thermodynamic potential. The reason for this resides on the fact that, whenever the value of the magnetic field causes an orbit on the Fermi surface to satisfy that quantization condition with  $\varepsilon_n \simeq \varepsilon_F^{(e)}$ , then the density of states at the Fermi level is enormously enhanced. It follows that the density of states at the Fermi level will be singular at regularly spaced intervals in  $\frac{1}{H}$  given by:

$$\Delta\left(\frac{1}{H}\right) \simeq \frac{2\pi e}{\hbar c} \frac{1}{\mathcal{A}_{\vec{k}}(\varepsilon_F^{(e)})} . \quad (5.129)$$

Evidently, the oscillatory behavior as a function of  $\frac{1}{H}$  with period Eq. (5.129) appears in any quantity that depends on the density of states at the Fermi energy. To check this, let us consider the thermodynamic potential at zero temperature:

$$\Omega(H) = g_L \sum_{r=0}^n (\varepsilon_r - \varepsilon_F^{(e)}) \quad (5.130)$$

where the summation over  $r$  is to be taken only on Landau levels such that  $\varepsilon_r \lesssim \varepsilon_F^{(e)}$ . Actually, the summation in Eq. (5.130) can be worked out by the Poisson summation formula or by the Euler-MacLaurin formula. Using standard arguments one finds for the oscillating term in the thermodynamic potential [102]:

$$\Omega_{osc}(H) \simeq \frac{V}{4\pi^2} \frac{e^2 H^2}{m_e^c c^2} \sum_{n=1}^{\infty} \frac{1}{\pi^2 n^2} \cos \left( 2\pi n \left[ \frac{\hbar c \mathcal{A}_{\vec{k}}(\varepsilon_F^{(e)})}{2\pi e H} - \frac{1}{2} \right] \right) . \quad (5.131)$$

Eq. (5.131) shows that the thermodynamic potential is, in fact, a periodic function of  $\frac{1}{H}$  with period given by Eq. (5.129). At finite temperatures the probability of occupation of a state with energy  $\varepsilon = \varepsilon_n$  is given by the Fermi-Dirac distribution. It can be seen that the effect of a finite temperature is to reduce the oscillation amplitude by the temperature-dependent factor:

$$R_T(H, T) \simeq \frac{2\pi^2 n \frac{k_B T}{\hbar \omega_c}}{\sinh \left( 2\pi^2 n \frac{k_B T}{\hbar \omega_c} \right)} . \quad (5.132)$$

Moreover, if the quasielectrons have a finite relaxation time  $\tau$  due to scattering, then the Landau energy levels become broadened. This, in turns, leads to a further reduction of the oscillation amplitude by the so-called Dingle factor [178]:

$$R_D \simeq e^{-\pi n \frac{m_e^c c}{e H \tau}} . \quad (5.133)$$

To determine the oscillation frequencies according to Eq. (5.129) we need to evaluate the k-space area enclosed by the semiclassical orbit at the Fermi energy. In the charge density wave ground state the low-energy quasielectron excitations are gapped as in Eq. (5.75). Therefore we find:

$$\mathcal{A}_{\vec{k}}(\varepsilon_F^{(e)}) \simeq 4 \frac{m_e^*}{\hbar^2} \theta_{FA} \int_{\Delta_{CDW}}^{\varepsilon_F^{(e)}} d\xi_{\vec{k}} \frac{\xi_{\vec{k}}}{\sqrt{\xi_{\vec{k}}^2 - \Delta_{CDW}^2}} \simeq 4 \frac{m_e^*}{\hbar^2} \theta_{FA} \sqrt{(\varepsilon_F^{(e)})^2 - \Delta_{CDW}^2} , \quad (5.134)$$

while the fundamental oscillation frequency is:

$$F \simeq \frac{\hbar c}{2\pi e} \mathcal{A}_{\vec{k}}(\varepsilon_F^{(e)}) . \quad (5.135)$$

Usually it is enough to retain the fundamental component of oscillation in the thermodynamic potential:

$$\Omega_{osc}(H) \simeq A R_T R_D \cos\left(2\pi \frac{F}{H}\right) \quad (5.136)$$

where  $R_T$  and  $R_D$  are given by Eqs. (5.132) and (5.133) with  $n = 1$  respectively, and  $A$  is an overall amplitude. From Eq. (5.135) we obtain our estimate for the fundamental frequency:

$$F \simeq \frac{2 m_e^* c}{\pi e \hbar} \theta_{FA} \varepsilon_F^{(e)} \sqrt{1 - \left(\frac{\Delta_{CDW}}{\varepsilon_F^{(e)}}\right)^2} . \quad (5.137)$$

Since  $\Delta_{CDW} \ll \varepsilon_F^{(e)}$  to a good approximation we can write:

$$F \simeq F_0 \simeq \frac{2 m_e^* c}{\pi e \hbar} \theta_{FA} \varepsilon_F^{(e)} . \quad (5.138)$$

In terms of the microscopic parameters of our model we end with the quite simple result:

$$F \simeq F_0 \simeq \phi_0 \frac{\delta}{a_0^2} \quad (5.139)$$

where  $\phi_0$  is the magnetic flux quantum Eq. (3.98). We see, then, that the main frequency in quantum oscillation phenomena grows almost linearly with the hole doping in qualitative agreement with observations (see, eg, Fig. 2, panel B in Ref. [179]). Moreover, in the underdoped region  $\delta \sim 0.1$ , using Eq. (5.139) we obtain  $F_0 \simeq 1300 T$  that differs by a factor of few from the quantum oscillation fundamental frequency measured in YBCO,  $F_0 \simeq 530 T$ . Our previous discussion suggests that apparently the influence of the charge density wave gap on the oscillation frequencies is negligible small. However, we showed in Sect. 5.4 that the charge density wave gap is slightly affected by the applied magnetic field. In fact, combining Eqs. (5.82) and (5.111) we have:

$$\Delta_{CDW}(H) \simeq \Delta_{CDW} - \frac{7}{4} \frac{\zeta(3)}{e^{2\gamma}} \frac{(\mu_B H)^2}{k_B T_{CDW}} . \quad (5.140)$$

This last equation implies an explicit dependence of the fundamental frequency on the magnetic field:

$$F(H) \simeq F_0 \left[ 1 + \frac{7}{4} \frac{\zeta(3)}{e^{2\gamma}} \left( \frac{\mu_B H}{\varepsilon_F^{(e)}} \right)^2 \right] . \quad (5.141)$$

Although the effect of the magnetic field is tiny, Eq. (5.141) introduces a non-linear dependence of the fundamental frequency on the "time"  $t = \frac{1}{H}$ . As a consequence, the thermodynamic potential is no more a strictly periodic function, but it becomes a quasi-periodic function of the time  $t$ . In nonlinear quantum oscillations there is a mixing of frequencies which could account for multiple oscillation frequencies observed in underdoped high temperature cuprate superconductors. To illustrate this point, let us consider the following thermodynamic potential:

$$\Omega(t) = \cos[2\pi F(t) t] , \quad (5.142)$$

where  $t = \frac{1}{H}$  is measured in  $\text{Tesla}^{-1}$  and the frequency  $F$  in Tesla. According to Eq. (5.141) we can write:

$$F(t) = F_0 \left[ 1 + \frac{\alpha}{t^2} \right] . \quad (5.143)$$

The parameter  $\alpha$  can be inferred by comparing Eq. (5.143) with Eq. (5.141). If we rewrite the frequency as:

$$F(t) = F_0 + \delta F(t) \quad , \quad \delta F(t) = \alpha \frac{F_0}{t^2} \quad , \quad (5.144)$$

then in the Fourier transform of  $\Omega(t)$  one expects to find the superposition of the dominant  $F_0$  oscillation with weak-er amplitude oscillations of frequencies  $F_0 \pm \delta F(t)$  and  $\delta F(t)$ . However the small frequency  $\delta F(t)$  depends on  $t$ , so that to check the above expectations we need to evaluate numerically the Fourier transform of the thermodynamic potential:

$$\tilde{\Omega}(\nu) = \int_{-\infty}^{+\infty} dt e^{-2\pi i \nu t} \Omega(t) . \quad (5.145)$$

It is convenient to write this last equation in the following form:

$$\tilde{\Omega}(\nu) = \frac{1}{\pi} \int_0^{+\infty} dt \cos \nu t \cos \left( F_0 t + 4\pi^2 \alpha \frac{F_0}{t} \right) . \quad (5.146)$$

For  $\alpha = 0$  it is easy to check that:

$$\tilde{\Omega}(\nu) = \delta(\nu - F_0) . \quad (5.147)$$

This shows that  $\tilde{\Omega}(\nu)$  is a tempered distribution. Therefore, to evaluate numerically the Fourier transform of the thermodynamic potential we must smear the distribution with a suitable test function. The most natural choice is to consider test functions with compact support. Accordingly, we consider:

$$\tilde{\Omega}(\nu) = \frac{1}{\pi} \int_{\nu - \frac{\Delta\nu}{2}}^{\nu + \frac{\Delta\nu}{2}} d\nu' \int_0^{+\infty} dt \cos \nu' t \cos \left( F_0 t + 4\pi^2 \alpha \frac{F_0}{t} \right) , \quad (5.148)$$

which corresponds to a test function  $f_t = 1$  within the bin  $\Delta\nu$  centered at the given frequency  $\nu$ , while  $f_t = 0$  otherwise. We further introduce the smeared spectral power function:

$$P(\nu) = |\tilde{\Omega}(\nu)|^2 . \quad (5.149)$$

In Fig. 23 we present the spectral power function Eq. (5.149) by assuming:

$$F_0 = 500 \text{ T} \quad , \quad \alpha = 10^{-3} \text{ T}^{-2} . \quad (5.150)$$

Note that the main frequency  $F_0$  is close to the observed oscillation frequency in underdoped YBCO. As concern the parameter  $\alpha$ , to magnify the effect of the mixing of frequencies we assumed a value much greater than the one obtained by Eq. (5.141). For comparison we also display in Fig. 23 the spectral power for  $\alpha = 0$ . In this case the spectral power should correspond to a smeared delta-function. In fact, we see (dashed line in Fig. 23) that all the spectral power is concentrated within the two bins around the main frequency  $F_0$ . On the other hand, for a non-zero value of the parameter  $\alpha$  the spectral power turns out to be considerably modified (see the continuum curve in Fig. 23). Indeed,

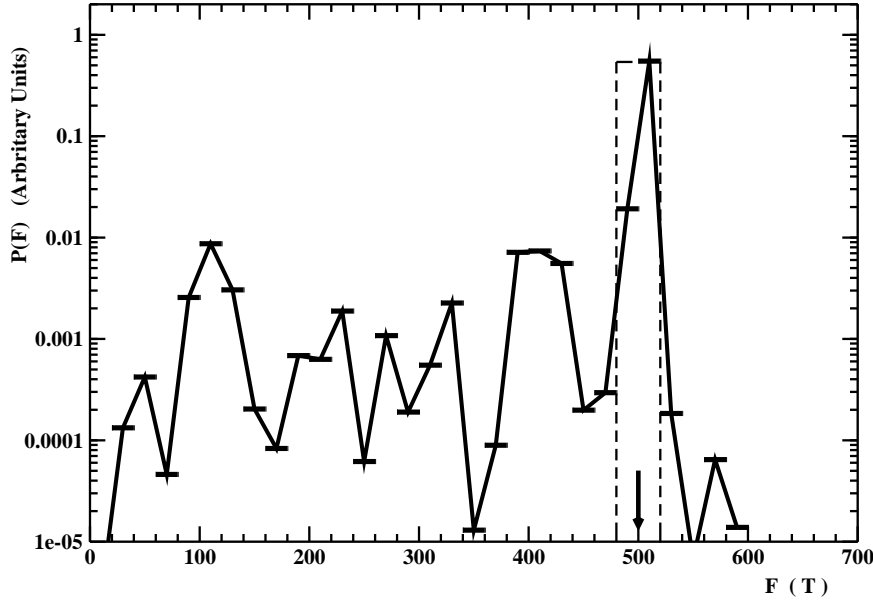


Figure 23: The spectral power function Eq. (5.149) versus the quantum oscillation frequency (measured in Tesla). The dotted line is the reference smeared spectral power corresponding to Eq. (5.147) with frequency  $F_0 = 500 T$  (indicated by the arrow) binned with bin size  $\Delta\nu = 20 T$ . The continuum line is the spectral power function corresponding to Eq. (5.148) adopting the same normalization as the reference spectral power.

the main peak in the Fourier transform is still at the frequency  $F_0$ . This peak accounts for about one half of the total spectral power. The other half of the spectral power is spread over multiple peaks. Interestingly enough, there are two peaks near the main frequency  $F_0 = 500 T$  corresponding to frequencies  $F_1 \simeq 440 T$  and  $F_2 = 550 T$ . It should be noted that the typical Fourier-transformed quantum oscillation amplitude in underdoped cuprates does show this characteristic almost symmetrically split three peaks structure. Usually, one explanation for the close frequencies in the Fourier transform is achieved by assuming a cylindrical Fermi surface that extends along the inter-layer direction with a small warping [180]. Indeed, warping manifests itself as a splitting corresponding to the so-called neck and belly frequencies. In this case the thermodynamic potential is customarily written as:

$$\Omega(t) = \cos(2\pi F_0 t) \times J_0(2\pi \Delta F t) , \quad (5.151)$$

where  $J_0$  is the Bessel function. In Eq. (5.151)  $\Delta F$  is the first harmonic of warping in the momentum direction perpendicular to the copper-oxide planes. Our results, however, are suggesting that the origin of multiple frequencies near the spectrally dominant frequency can be accounted for by the non-linearities in quantum oscillation phenomena due to the magnetic field dependence of the charge density wave gap. Another interesting feature in Fig. 23 is due to the presence of sizable spectral power in the low frequency region. In particular, there is a peak in the Fourier transform at  $F_3 \simeq 100 T$ . In the conventional interpretation this peak would be attributed to an additional small Fermi pocket of quasi-electrons or quasiholes, which would imply a drastic Fermi surface reconstruction. We feel that the qualitative agreement of Fig. 23 with the Fourier transform of the quantum oscillation amplitude in underdoped cuprates is suggesting that the origin of multiple



frequencies resides in the intrinsic non-linearity caused by the charge density wave gap. To conclude this Section, we briefly discuss the cyclotron effective mass. After taking into account Eq. (5.126) we rewrite Eq. (5.122) as:

$$m_e^c \simeq \frac{\hbar^2}{2\pi} \frac{\mathcal{A}_{\vec{k}}(\varepsilon_{n+1}) - \mathcal{A}_{\vec{k}}(\varepsilon_n)}{\varepsilon_{n+1} - \varepsilon_n} . \quad (5.152)$$

In quantum oscillations the involved Landau levels have energies very close to the Fermi energy. So that we may employ Eq. (5.134) to get:

$$m_e^c \simeq \frac{2}{\pi} m_e^* \theta_{FA} \sqrt{1 - \left( \frac{\Delta_{CDW}}{\varepsilon_F^{(e)}} \right)^2} . \quad (5.153)$$

So that, to a good approximation, we are left with the quite simple result:

$$m_e^c \simeq \frac{\delta}{1 - \delta} m_e^* . \quad (5.154)$$

Evidently the cyclotron effective mass is smaller than the quasielectron effective mass and it increases almost linearly with the hole doping fraction  $\delta$ . However, the cyclotron effective mass measured by quantum oscillations, generally, turns out to be greater than the effective mass and strongly dependent on the hole doping. Indeed, the cyclotron mass is seen to extrapolate to a mass divergence at two hole doping points,  $\delta_1$  and  $\delta_2$  (compare, for instance, with Fig. 11, panel d, in Ref. [96]). The precise values of these hole doping depend on the cuprate family. Nevertheless, several recent studies [181, 182, 183, 184, 16, 185, 186] indicated that:

$$\delta_1 \simeq 0.08 - 0.10 \quad , \quad \delta_2 \simeq 0.18 - 0.20 . \quad (5.155)$$

It is widely believed that the point  $\delta = \delta_1$  is a Lifshitz critical point due to a variation of the topology of the Fermi surface [187], while the point  $\delta = \delta_2$  is identified with a quantum critical point, i.e. a phase transition at zero temperature induced by tuning some external parameter of the system [188].

To extract the cyclotron mass from quantum oscillations the relevant oscillating amplitude is assumed to be of the form:

$$A_{osc} = A R_T R_D \cos(2\pi \frac{F}{H}) J_0(2\pi \frac{\Delta F}{H}) , \quad (5.156)$$

with

$$R_D \simeq e^{-\pi \frac{m_e^c c}{eH} \frac{1}{\tau}} , \quad (5.157)$$

$$R_T \simeq \frac{2\pi^2 k_B T \frac{m_e^c c}{\hbar e H}}{\sinh(2\pi^2 k_B T \frac{m_e^c c}{\hbar e H})} . \quad (5.158)$$

The cyclotron mass is, then, obtained by fitting for a particular hole doping the temperature dependence of the oscillating amplitude to Eq. (5.156), keeping  $\tau$  and  $F$  fixed. We feel, however, that the assumption of a temperature independent relaxation time in the pseudogap region of hole doped cuprates is highly questionable. In normal metals at low temperatures the relaxation time is dominated by the scattering of low-lying excitations

off impurities. In that case one can safely neglect the temperature dependence of the relaxation time at low enough temperatures. However, it must be remarked that in our approach the nodal quasielectrons are the effective low-lying excitations which are able to retain the needed quantum coherence only on the Fermi arcs. Therefore the quasielectron relaxation time is determined by scattering processes that preserve the quasielectron coherence. At low temperatures it results that the nodal quasielectron relaxation time is entirely due to the Coulomb interaction. In fact, Coulomb umklapp scattering between quasielectrons on opposite nodal Fermi arcs allows the quasielectrons to retain coherence and hence to contribute to the conduction processes. Notably the calculation of the relaxation time has been recently discussed in details in Ref. [189]. As a result one finds:

$$\frac{1}{\tau_{ee}} \sim T^2 . \quad (5.159)$$

Note that this temperature dependence is in agreement with the spectroscopic evidence for the Fermi liquid-like behavior of the relaxation rate in the pseudogap phase of hole doped cuprates [190, 191]. It is amusing to mention that the Coulomb umklapp processes are allowed in the rather narrow interval:

$$\tilde{\delta}_1 \lesssim \delta \lesssim \tilde{\delta}_2 . \quad (5.160)$$

The meaning of Eq. (5.160) is that outside this interval the nodal quasielectrons cannot contribute to the conduction processes. We found  $\tilde{\delta}_1 \simeq 0.15$ ,  $\tilde{\delta}_2 \simeq 0.21$ , which are remarkably close to the putative critical points Eq. (5.155). Actually, the slight difference can be presumably ascribed to the extreme simplifications of our model. So that, we are led to suspect that the origin of the puzzling critical points could reside in the peculiar doping dependence of the nodal quasielectron relaxation time.

For the purposes of determining the cyclotron mass from quantum oscillations we need to keep track of the temperature dependence of the relaxation time, Eq. (5.159). Then, a remarkably thing that occurs is that the Dingle factor Eq. (5.157) becomes temperature dependent. Therefore, before drawing any conclusions regarding the cyclotron mass, it is necessary to reanalyze the data with a fitting procedure which allows the Dingle factor to depend on the temperature.

## 6 Summary and Conclusions

Understanding high temperature superconductivity in copper oxides remains one of the most challenging problem in condensed matter physics. Since the discovery of superconductivity in cuprates [1] there has been a tremendous advance in understanding their physical properties and many experimental and theoretical points have been clarified. It has emerged that these compounds possess a number of unusual normal state and superconducting properties due to a complicated interplay of electronic, spin, and lattice degrees of freedom. In view of the fact that cuprates are very complex materials, no consensus on a common accepted interpretation of all the physical phenomena and the mechanism for formation of the superconducting state has yet been achieved. Notwithstanding, since long time P. W. Anderson convincingly stated [19, 20] that the essential physics, including superconductivity, was contained in an effective two dimensional square lattice Hubbard model. The electronic structure is such that at low energies there is a

single spin degenerate band of correlated electrons with a two-dimensional dispersion in the copper-oxygen plane, while the dispersion in the third direction may in first approximation be neglected. Indeed, numerical approaches have given strong reason to believe that this basic picture was correct, namely the two-dimensional Hubbard model captures the basic physics of the superconductivity and the pseudogap (for a recent comprehensive overview, see Ref. [192] and references therein).

The cuprate challenge could best met by the construction of a phenomenological simplified model inspired by experiment which, nevertheless, is able to capture at least qualitatively the physics of cuprate superconductors. In fact, in our previous paper [22] we attempted to find a picture that was as simple as possible and that represented phenomena as accurately as possible. The driving principle of the approach presented in I has been that the high temperature superconductivity could be understood within some framework along the line of the microscopic theory of Bardeen, Cooper, and Schrieffer. To construct a phenomenological model able to recover the most salient aspects of the unusual behavior seen in the various regions of the phase diagram of hole doped cuprates, we relied heavily on some assumptions. First, we assumed that the physics of the high temperature cuprates was deeply rooted in the copper-oxide planes. This allowed us to completely neglect the motion along the direction perpendicular to the  $CuO_2$  planes. In addition, we assumed that the single-band effective Hubbard model is sufficient to account for all the essential physics of the copper-oxide planes. Accordingly, in I we proposed an effective Hamiltonian aimed to describe the dynamics of the holes injected into the undoped copper-oxide planes. We arrived at our effective Hamiltonian by using known arguments on the motion of charge carriers in an antiferromagnetic background. Notwithstanding, we were unable to offer a truly microscopic derivation of the effective Hamiltonian. Thereby our arguments, albeit suggestive, cannot be considered as a first principle derivation. In spite of that, we showed that the effective Hamiltonian offered a consistent picture of the high transition temperature cuprate superconductors. Firstly, due to the reduced dimensionality the two-body attractive potential turned out to admit real-space d-wave bound states. The binding energy of these bound states, which plays the role of the pseudogap, decreases with increasing doping until it vanishes at a certain critical doping  $\delta = \delta^*$ . This allowed us to reach the conclusion that the key features of the underdoped side of the phase diagram were controlled by very strong pairing that is phase-disordered by thermal fluctuations. In our model the overdoped region is realized for hole doping in excess of the critical doping  $\delta^*$  where the pseudogap vanishes. It is well established that the long range antiferromagnetic order in the underdoped region is rapidly lost with increasing  $\delta$ , but nevertheless two-dimensional short-range order persists up to the overdoped region. This led us to conclude that in this region the conventional d-wave BCS framework account for many of the low-energy and low-temperature properties of the copper oxides, in nice agreement with several observations. Finally, we pointed out that in the optimal doped region the competition between the pseudogap and the d-wave BCS gap together with the enhanced role of the phase fluctuations makes the mean field approximation of doubtful validity.

The aim of the present paper was to discuss in greater details the physics of the underdoped region in hole doped high temperature cuprate superconductors. Indeed, recently the enigmatic cuprate superconductors have attracted resurgent interest with several reports and discussions of competing orders in the underdoped side. Even though in I we presented a partial account of the pseudogap region, we did not attempt a complete

discussion of the strange behavior of the cuprates in this region. In this paper we attempted a serious effort to bring together several observational features of the hole doped high temperature cuprate superconductors in the pseudogap region. We discussed in greater details with respect to I the structure of the hole pair condensate ground state. Moreover, we argued that the low-lying excitations of the condensate were the analog of rotons in  $^4\text{He}$ . One crucial point to enlighten was that these elementary excitations relied heavily on the phase coherence of the hole pair condensate. Taking into account that in the pseudogap region the superconductive transition is described by the Berezinskii-Kosterlitz-Thouless order-disorder transition and using the Kosterlitz's recursion relation for the screening length, we were able to establish the temperature dependence of both the superfluid velocity and the hole pair condensate fraction. We also considered the microscopic dynamics of the hole pair condensate in presence of applied magnetic fields transverse to the copper-oxide planes. We worked out the thermodynamics of the roton gas near the superconductive critical temperature. Remarkably, we found that even in the ideal gas approximation the specific heat anomaly in the critical region could be accounted for qualitatively and quantitatively by the roton gas. We discussed the electrodynamics of the charged hole pair condensate. In particular, we determined the dependence of the London penetration length on the hole doping fraction and on the temperature. We critically compared our peculiar temperature dependence of the penetration length with experimental observations for different class of cuprate superconductors in the underdoped and optimal doped regions. We carefully investigated the structure of the Abrikosov vortex and obtained the lower and upper critical magnetic fields. We found that the doping and temperature dependence of the critical magnetic fields compared in satisfying agreement with several experimental studies. We also determined and compared with selected observations the temperature dependence of the critical current.

Inspired by the cuprate phenomenology that points to a clear experimental evidence for nodal quasielectron quantum liquid, we developed some arguments to justify how the presence of the pseudogap were responsible for the formation of the quasielectron nodal Fermi liquid. In our approach the nodal quasielectrons are effective low energy excitations in the phase disordered hole pair condensate which retain their quantum coherence only in the nodal directions. We showed that the interplay between the condensate roton excitations and the nodal quasielectrons laid at the heart of the so-called nodal gap. We further determined the doping and temperature dependence of the nodal gap and contrasted successfully with available experimental data in literature. We also discussed the nodal Fermi velocity detected by angle resolved photoemission spectroscopy. We critically examined the contribution of the nodal quasielectrons to the low temperature specific heat with and without external transverse magnetic fields. We proposed that the charge density wave instabilities in hole doped high temperature superconductors were triggered by the interactions of nodal quasielectrons with longitudinal bond-stretching phonon modes of the planar copper-oxide lattice. Our proposal allowed us to determine and to compare with experimental data both the doping dependence of the charge density wave critical temperature and the temperature dependence of the charge density wave gap. We also were able to clarify the puzzling competition between charge order and superconductivity. Finally, we discussed the physics behind quantum oscillations in the pseudogap region. In particular, we suggested that the origin of multiple frequencies in quantum oscillations resided in the intrinsic non-linearity implied by the dependence of the charge density wave gap on applied magnetic fields.

The inherent complexity of the hole doped cuprates has hidden key features of the pairing mechanism in most experiments, preventing a satisfactory understanding of high temperature superconductivity. In our previous and in the present paper we have shown that a relatively simple model for the effective Hamiltonian based on plausible physical assumptions allowed to reach a coherent and fairly complete picture of hole doped high temperature cuprate superconductors. In our opinion, the results presented in our papers should be useful to reach a truly microscopic explanation of the high temperature superconductivity in cuprates. To conclude, we would like to stress that we did not discuss in the present paper the transport phenomena in cuprate superconductors. Actually, even though we already reached some partial results on this subject, we refrained to include even a partial account of these problematics in order to avoid the increase of the length of the present paper beyond reasonable limits.

## A D-Wave BCS Gap and Penetration Depth

In the overdoped region the superconductive instability is driven by the short-range attractive interaction between the quasiholes. This means that the pairing is in momentum space, so that the relevant superconducting ground state is the BCS variational ground state. At zero temperature the relevant gap equation has been discussed since long time [193]:

$$\Delta(\vec{k}) = -\frac{1}{2} \sum_{\vec{k}'} \frac{V(\vec{k} - \vec{k}') \Delta(\vec{k}')}{\sqrt{\xi_{\vec{k}'}^2 + |\Delta(\vec{k}')|^2}}, \quad (\text{A.1})$$

where:

$$\xi_{\vec{k}} = \frac{\hbar^2 \vec{k}^2}{2m_h^*} - \varepsilon_F, \quad (\text{A.2})$$

$\varepsilon_F$  being the Fermi energy, and

$$V(\vec{k} - \vec{k}') = \int d\vec{r} e^{-i(\vec{k} - \vec{k}') \cdot \vec{r}} V(r). \quad (\text{A.3})$$

Using the expansion:

$$e^{i\vec{k} \cdot \vec{r}} = e^{ikr \cos \theta_{kr}} = \sum_{m=-\infty}^{+\infty} e^{im(\theta_{kr} + \frac{\pi}{2})} J_m(kr), \quad (\text{A.4})$$

we may rewrite Eq. (A.1) as:

$$\Delta(\vec{k}) = -\frac{1}{2} \sum_{\vec{k}'} \sum_{m=-\infty}^{+\infty} e^{im\theta_{kk'}} \frac{V_m(k, k') \Delta(\vec{k}')}{\sqrt{\xi_{\vec{k}'}^2 + |\Delta(\vec{k}')|^2}}, \quad (\text{A.5})$$

with:

$$V_m(k, k') = 2\pi \int_0^\infty dr r V(r) J_m(kr) J_m(k'r). \quad (\text{A.6})$$

Equation (A.5) suggests that:

$$\Delta(\vec{k}) = \Delta(k, \theta_k) = \sum_{\ell=-\infty}^{+\infty} e^{i\ell\theta_k} \Delta_\ell(k), \quad (\text{A.7})$$

In the weak coupling limit Eq. (A.5) reduces to [193]:

$$\Delta_m(k, \theta_k) \simeq -\frac{1}{2} \sum_{\vec{k}'} e^{im\theta_{kk'}} \frac{V_m(k, k') \Delta_m(k', \theta_{k'})}{\sqrt{\xi_{\vec{k}'}^2 + |\Delta_m(k', \theta_{k'})|^2}}. \quad (\text{A.8})$$

As discussed in I, Eq. (A.8) admits non trivial solutions for the d-wave gap ( $m = \pm 2$ ). Moreover, we have [22]:

$$\Delta_2(k, \theta_k) = \Delta_{BCS}(k) \cos(2\theta_k). \quad (\text{A.9})$$

Thus, we end with the following gap equation:

$$\Delta_{BCS}(k) \simeq - \sum_{\vec{k}'} [\cos(2\theta_{k'})]^2 \frac{V_2(k, k') \Delta_{BCS}(k')}{\sqrt{\xi_{\vec{k}'}^2 + [\Delta_{BCS}(k') \cos(2\theta_{k'})]^2}}. \quad (\text{A.10})$$

Since the gap is sizable on the Fermi surface, we may further simplify Eq. (A.10) as:

$$1 \simeq -V_2 \int \frac{d\vec{k}'}{(2\pi)^2} \frac{[\cos(2\theta_{k'})]^2}{\sqrt{\xi_{\vec{k}'}^2 + [\Delta_{BCS} \cos(2\theta_{k'})]^2}} \quad (\text{A.11})$$

where  $\Delta_{BCS} = \Delta_{BCS}(k_F)$  and  $V_2 = V_2(k_F, k_F)$ . After some standard manipulations we obtain:

$$1 \simeq -\frac{V_2 m_h^*}{\hbar^2} \int_{-\varepsilon_c}^{+\varepsilon_c} \frac{d\xi}{(2\pi)^2} \int_0^{2\pi} d\theta \frac{[\cos(2\theta)]^2}{\sqrt{\xi^2 + [\Delta_{BCS} \cos(2\theta)]^2}} \quad (\text{A.12})$$

where  $\varepsilon_c$  is a high-energy cut-off which, usually is much smaller than the Fermi energy. Performing the integrals and using the approximation:

$$\text{archsinh} \left[ \frac{\varepsilon_c}{\Delta_{BCS} |\cos(2\theta)|} \right] \simeq \ln \left[ \frac{2\varepsilon_c}{\Delta_{BCS} |\cos(2\theta)|} \right], \quad (\text{A.13})$$

we get:

$$\Delta_{BCS} \simeq \frac{4\varepsilon_c}{\sqrt{e}} e^{-\frac{1}{\lambda_2}}, \quad (\text{A.14})$$

where:

$$\lambda_2 = \frac{m_h^* V_0}{\hbar^2} \int_0^{r_0(\delta)} dr r [J_2(k_F r)]^2. \quad (\text{A.15})$$

To obtain the critical temperature, we note that [194] (see below):

$$\frac{\Delta_{BCS}}{k_B T_c} \simeq \pi e^{\ln 2 - \frac{1}{2} - \gamma} \simeq 2.140. \quad (\text{A.16})$$

We obtain, thus, the BCS critical temperature  $T_c \equiv T_{BCS}$ :

$$k_B T_{BCS} \simeq \frac{2e^\gamma}{\pi} \varepsilon_c e^{-\frac{1}{\lambda_2}}. \quad (\text{A.17})$$

In I we argued that it is natural to identify the cut-off energy  $\varepsilon_c$  with  $\Delta_2(\delta = 0)$  which, indeed, is much smaller than the Fermi energy in the range of hole doping fraction of interest.

To obtain the thermal corrections to the BCS gap we use the well-known gap equation at finite temperatures [193, 194]. With the same approximations as before, we find that at finite temperature Eq. (A.11) is replaced by:

$$1 \simeq -V_2 \int \frac{d\vec{k}'}{(2\pi)^2} \frac{[\cos(2\theta_{k'})]^2}{\sqrt{\xi_{k'}^2 + [\Delta_{BCS} \cos(2\theta_{k'})]^2}} \tanh\left(\frac{\sqrt{\xi_{k'}^2 + [\cos(2\theta_{k'})]^2}}{2k_B T}\right). \quad (\text{A.18})$$

In principle, solving Eq. (A.18) one obtains the BCS energy gap at finite temperature,  $\Delta_{BCS}(T)$ . Note that at zero temperature Eq. (A.18) reduces to Eq. (A.11), so that  $\Delta_{BCS}(T = 0)$  is given by Eq. (A.14). To proceed further, we rewrite Eq. (A.18) in the following form:

$$\begin{aligned} \int \frac{d\vec{k}'}{(2\pi)^2} \frac{[\cos(2\theta_{k'})]^2}{\sqrt{\xi_{k'}^2 + [\Delta_{BCS} \cos(2\theta_{k'})]^2}} &= \int \frac{d\vec{k}'}{(2\pi)^2} \frac{[\cos(2\theta_{k'})]^2}{\sqrt{\xi_{k'}^2 + [\Delta_{BCS} \cos(2\theta_{k'})]^2}} \\ &+ \int \frac{d\vec{k}'}{(2\pi)^2} \frac{[\cos(2\theta_{k'})]^2}{\sqrt{\xi_{k'}^2 + [\Delta_{BCS} \cos(2\theta_{k'})]^2}} \left[ \tanh\left(\frac{\sqrt{\xi_{k'}^2 + [\Delta_{BCS} \cos(2\theta_{k'})]^2}}{2k_B T}\right) - 1 \right]. \end{aligned} \quad (\text{A.19})$$

Combining Eqs. (A.11) and (A.18), and in the same approximations as before, after some manipulations we obtain:

$$\begin{aligned} \int_0^{\varepsilon_c} d\xi \int_0^{2\pi} d\theta \frac{[\cos(2\theta)]^2}{\sqrt{\xi^2 + [\Delta_{BCS}(0) \cos(2\theta)]^2}} &= \int_0^{\varepsilon_c} d\xi \int_0^{2\pi} d\theta \frac{[\cos(2\theta)]^2}{\sqrt{\xi^2 + [\Delta_{BCS}(T) \cos(2\theta)]^2}} \\ &+ \int_0^{\varepsilon_c} d\xi \int_0^{2\pi} d\theta \frac{[\cos(2\theta)]^2}{\sqrt{\xi^2 + [\Delta_{BCS}(T) \cos(2\theta)]^2}} \left[ \tanh\left(\frac{\sqrt{\xi^2 + [\Delta_{BCS}(T) \cos(2\theta)]^2}}{2k_B T}\right) - 1 \right]. \end{aligned} \quad (\text{A.20})$$

Now, we observe that:

$$\begin{aligned} \int_0^{\varepsilon_c} d\xi \int_0^{2\pi} d\theta \frac{\cos^2(2\theta)}{\sqrt{\xi^2 + [\Delta \cos(2\theta)]^2}} &\simeq \int_0^{2\pi} d\theta \cos^2(2\theta) \log\left(\frac{2\varepsilon_c}{\Delta |\cos(2\theta)|}\right) \\ &= \pi \left[ \log\left(\frac{2\varepsilon_c}{\Delta}\right) + \log 2 - \frac{1}{2} \right]. \end{aligned} \quad (\text{A.21})$$

This allows us to put Eq. (A.20) into:

$$\begin{aligned} \pi \ln \left[ \frac{\Delta_{BCS}(T)}{\Delta_{BCS}(0)} \right] &= -2 \int_0^{\varepsilon_c} d\xi \int_0^{2\pi} d\theta \\ &\frac{\cos^2(2\theta)}{\sqrt{\xi^2 + [\Delta_{BCS}(T) \cos(2\theta)]^2}} \frac{1}{e^{\left(\frac{\sqrt{\xi^2 + [\Delta_{BCS}(T) \cos(2\theta)]^2}}{k_B T}\right)} + 1}. \end{aligned} \quad (\text{A.22})$$

Putting  $x = \frac{\xi}{k_B T}$  and using  $\varepsilon_c \gg k_B T$ , we obtain:

$$\pi \ln \left[ \frac{\Delta_{BCS}(T)}{\Delta_{BCS}(0)} \right] \simeq -2 \int_0^\infty dx \int_0^{2\pi} d\theta \frac{\cos^2(2\theta)}{\sqrt{x^2 + z^2}} \frac{1}{e^{(\sqrt{x^2 + z^2})} + 1} , \quad (\text{A.23})$$

where:

$$z = \frac{\Delta_{BCS}(T)}{k_B T} |\cos(2\theta)| . \quad (\text{A.24})$$

Let us consider:

$$F(z) = 2 \int_0^\infty dx \frac{1}{\sqrt{x^2 + z^2}} \frac{1}{e^{(\sqrt{x^2 + z^2})} + 1} = F_1(z) + F_2(z) , \quad (\text{A.25})$$

where:

$$F_1(z) = \int_0^\infty dx \left[ \frac{1}{\sqrt{x^2 + z^2}} - \frac{1}{x} \tanh\left(\frac{x}{2}\right) \right] , \quad (\text{A.26})$$

and

$$F_2(z) = \int_0^\infty dx \left[ \frac{1}{x} \tanh\left(\frac{x}{2}\right) - \frac{1}{\sqrt{x^2 + z^2}} \tanh\left(\frac{\sqrt{x^2 + z^2}}{2}\right) \right] . \quad (\text{A.27})$$

Since:

$$F_1(z) = \ln \left[ \frac{\pi}{e^\gamma z} \right] , \quad (\text{A.28})$$

we can rewrite Eq. (A.23) as:

$$\pi \ln \left[ \frac{\Delta_{BCS}(T)}{\Delta_{BCS}(0)} \right] \simeq - \int_0^{2\pi} d\theta \cos^2(2\theta) \ln \left[ \frac{\pi}{e^\gamma z} \right] - \int_0^{2\pi} d\theta \cos^2(2\theta) F_2(z) . \quad (\text{A.29})$$

Finally, observing that:

$$\int_0^{2\pi} d\theta \cos^2(2\theta) \ln \left[ \frac{\pi}{e^\gamma z} \right] = \pi \left( \ln \left[ \frac{\pi k_B T}{e^\gamma \Delta_{BCS}(T)} \right] + \ln 2 - \frac{1}{2} \right) , \quad (\text{A.30})$$

we obtain:

$$\pi \ln \left[ \frac{2\pi k_B T}{e^\gamma \sqrt{e} \Delta_{BCS}(0)} \right] = - \int_0^{2\pi} d\theta \cos^2(2\theta) F_2 \left( \frac{\Delta_{BCS}(T)}{k_B T} |\cos(2\theta)| \right) . \quad (\text{A.31})$$

The superconductive ordering sets in at a critical temperature where the energy gap vanishes. Since  $F_2(0) = 0$ , from Eq. (A.31) we obtain at once:

$$\frac{k_B T_{BCS}}{\Delta_{BCS}(0)} = \frac{e^\gamma \sqrt{e}}{2\pi} , \quad (\text{A.32})$$

which agrees with Eq. (A.16). This last equation allows us to write Eq. (A.31) in the more useful form:

$$\pi \ln \left( \frac{T}{T_{BCS}} \right) = - \int_0^{2\pi} d\theta \cos^2(2\theta) F_2 \left( \frac{\Delta_{BCS}(T)}{k_B T} |\cos(2\theta)| \right) . \quad (\text{A.33})$$



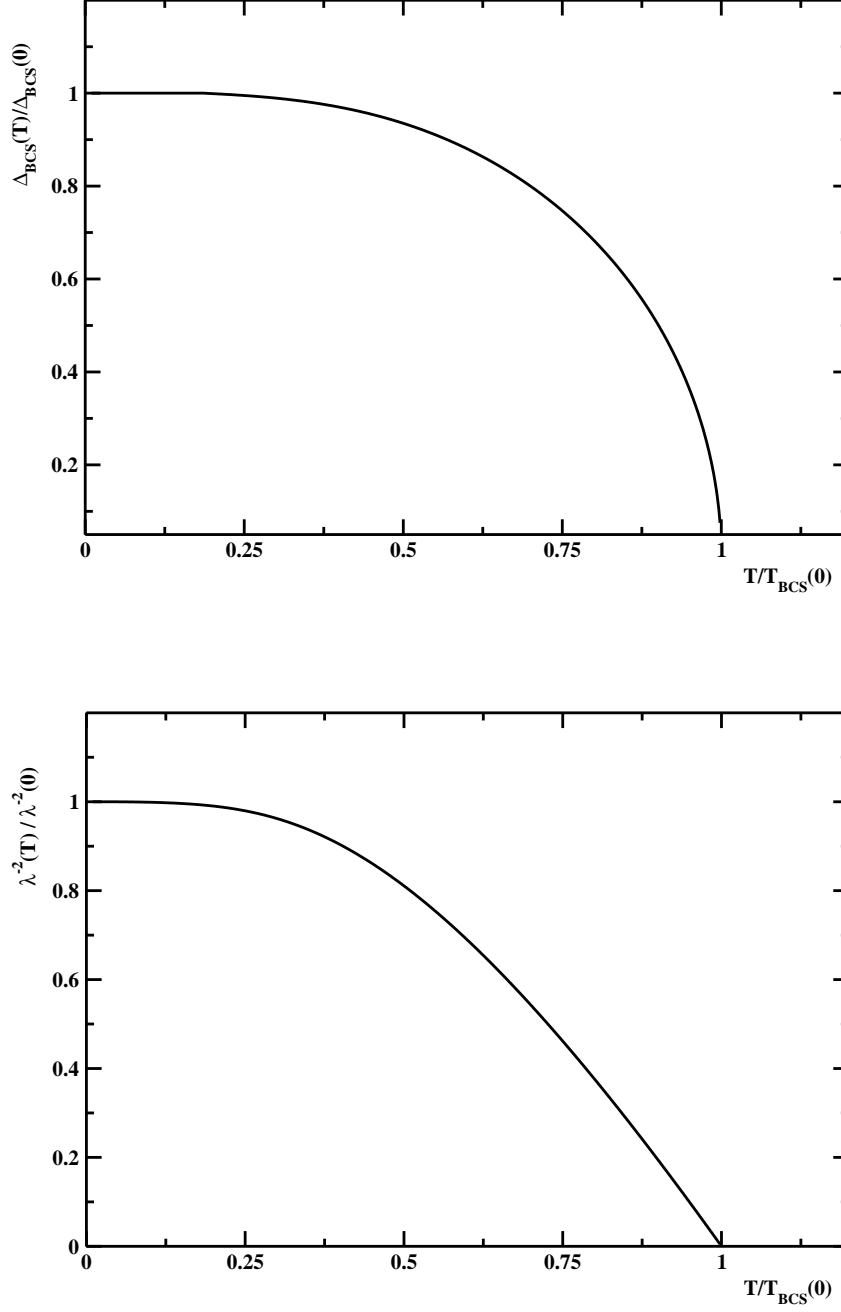


Figure 24: (Top) Temperature dependence of the BCS energy gap  $\Delta_{\text{BCS}}(T)$ . (Bottom) Temperature dependence of the BCS weak-coupling penetration depth  $\lambda^{-2}(T)$  in the London limit.

The remaining integral in Eq. (A.33) must be handled numerically. As a result one obtains the BCS energy gap as a function of the temperature. In Fig. 24, top panel, we display the BCS energy gap  $\Delta_{BCS}(T)$  versus the reduced temperature.

To conclude this Section, we address ourselves to the problem of evaluating the thermal behavior of the penetration length. In the London limit the BCS weak coupling d-wave theory gives for the penetration length the following expression (see, for instance, Ref. [87]):

$$\frac{\lambda^{-2}(T)}{\lambda^{-2}(0)} \simeq 1 - \frac{2}{\pi k_B T} \int_0^\infty dx \int_0^{2\pi} d\theta \cos^2(2\theta) \frac{e^{\frac{E}{k_B T}}}{\left[1 + e^{\frac{E}{k_B T}}\right]^2}, \quad (\text{A.34})$$

where

$$E = \sqrt{x^2 + \Delta_{BCS}^2(T) \cos^2(2\theta)}. \quad (\text{A.35})$$

For vanishing temperatures the integral in Eq. (A.34) vanishes as  $e^{-\Delta_{BCS}/k_B T}$ , so that the penetration length tends exponentially to the zero-temperature value. On the other hand, at the critical temperature  $T_{BCS}$ , the BCS energy gap vanishes. Then, from Eq. (A.34) we infer:

$$\frac{\lambda^{-2}(T_{BCS})}{\lambda^{-2}(0)} \simeq 1 - \frac{2}{\pi k_B T_{BCS}} \int_0^\infty dx \int_0^{2\pi} d\theta \cos^2(2\theta) \frac{e^{\frac{x}{k_B T_{BCS}}}}{\left[1 + e^{\frac{x}{k_B T_{BCS}}}\right]^2}. \quad (\text{A.36})$$

Observing that:

$$\int_0^{2\pi} d\theta \cos^2(2\theta) = \pi, \quad \frac{1}{k_B T_{BCS}} \int_0^\infty dx \frac{e^{\frac{x}{k_B T_{BCS}}}}{\left[1 + e^{\frac{x}{k_B T_{BCS}}}\right]^2} = \frac{1}{2}, \quad (\text{A.37})$$

one can easily check that, indeed,  $\lambda^{-2}(T_{BCS}) = 0$ . The temperature dependence of the London penetration length can be obtained by integrating numerically the double integral in Eq. (A.34), after taking into account the temperature dependence of the BCS gap. In Fig. 24, bottom panel, we display the BCS London penetration length versus the reduced temperature.

## References

- [1] J. G. Bednorz and K. A. Müller, *Z. Physik B* **64**, 189 (1986).
- [2] D. N. Besov and T. Timusk, *Rev. Mod. Phys.* **77**, 721 (2005).
- [3] A. J. Leggett, *Nature Physics* **2**, 135 (2006).
- [4] P. A. Lee, N. Nagaosa, and X. -G. Wen, *Rev. Mod. Phys.* **78**, 17 (2006).
- [5] J. R. Schrieffer and J. S. Brooks Eds., *Handbook of High-Temperature Superconductivity*, Springer Science + Business Media, New York, USA (2007).
- [6] N. Plakida, *High-Temperature Cuprate Superconductors*, Springer-Verlag, Berlin, Heidelberg (2010).

- [7] H. Alloul, *Compt. Rend. Phys.* **15**, 519 (2014).
- [8] R. Wesche, *Physical Properties of High-Temperature Superconductors*, J. Wiley & Sons, Ltd (2015).
- [9] L. Taillefer, *Annu. Rev. Condens. Matter Phys.* **1**, 51 (2010).
- [10] B. Keimer, S. A. Kivelson, M. R. Norman, S. Uchida, and J. Zaanen, *Nature* **518**, 179 (2015).
- [11] E. Fradkin, S. A. Kivelson, and J. M. Tranquada, *Rev. Mod. Phys.* **87**, 457 (2015).
- [12] T. Timusk and B. Statt, *Rep. Prog. Phys.* **62**, 61 (1999).
- [13] J. L. Tallon and J. W. Loran, *Physica C* **349**, 53 (2001).
- [14] C. Phillips, A. Saxena, and A. R. Bishop, *Rep. Prog. Phys.* **66**, 2111 (2003).
- [15] S. H fner, M. A. Hossain, A. Damascelli, and G. A. Sawatzky, *Rep. Prog. Phys.* **71**, 062501 (2008).
- [16] A. Sacuto, Y. Gallais, M. Cazayous, M.-A. M  asson, G. D. Gu, and D. Colson, *Rep. Prog. Phys.* **76**, 022502 (2013).
- [17] A. A. Kordyuk, *Low Temp. Phys.* **41**, 319 (2015).
- [18] E. Fradkin and S. A. Kivelson, *Nature Physics* **8**, 864 (2012).
- [19] P. W. Anderson, *Science* **235**, 1196 (1987).
- [20] P. W. Anderson, *The Theory of Superconductivity in the High- $T_c$  Cuprates*, Princeton University Press, Princeton, New Jersey (1997).
- [21] P. W. Anderson, *Phys. Rev.* **115**, 2 (1959).
- [22] P. Cea, *Riv. Nuovo Cim.* **3**, 41 (2013).
- [23] K. Huang and E. Manousakis, *Phys. Rev. B* **36**, 8302 (1987).
- [24] J. E. Hirsch, *Phys. Rev. Lett.* **59**, 228 (1987).
- [25] J. R. Schrieffer, X. -G. Wen, and S. -C. Zhang, *Phys. Rev. Lett.* **60**, 944 (1988); *Phys. Rev. B* **39**, 11663 (1989).
- [26] S. W. Jang, *et al.*, arXiv:1510.07479 (2015).
- [27] M. R. Schafroth, *Phys. Rev.* **100**, 463 (1955).
- [28] J. M. Blatt and S. T. Butler, *Phys. Rev.* **100**, 476 (1955).
- [29] J. M. Blatt, *Theory of Superconductivity* Academic Press, New York and London (1964).
- [30] N. D. Mermin and H. Wagner, *Phys. Rev. Lett.* **17**, 1133 (1966).

- [31] P. C. Hohenberg, Phys. Rev. **158**, 383 (1967).
- [32] Y. Yildirim and W. Ku, Phys. Rev. B **92**, 180501(R) (2015).
- [33] C. Renner, *et al.*, Phys. Rev. Lett. **80**, 149 (1998).
- [34] A. Kanigel, *et al.*, Phys. Rev. Lett. **101**, 137002 (2008).
- [35] H.-B. Yang, *et al.*, Nature **456**, 77 (2008).
- [36] V. Mishra, U. Chatterjee, J. C. Campuzano, and M. R. Norman, Nature Physics **10**, 357 (2014).
- [37] T. Kondo, *et al.*, Nature Commun. **6**, 7699 (2015).
- [38] V. L. Berezinskii, Sov. Phys. JETP **32**, 493 (1971); Sov. Phys. JETP **34**, 610 (1972).
- [39] J. M. Kosterlitz and D. J. Thouless, J. Phys. C **6**, 1181 (1973).
- [40] V. J. Emery and S. A. Kilvelson, Nature **374**, 434 (1995).
- [41] I. Hetel, T. R. Lemberger and M. Randeira, Nature Physics **3**, 700 (2007).
- [42] L. N. Cooper, Phys. Rev. **104**, 1189 (1956).
- [43] J. Bardeen, L. N. Cooper and J. R. Schrieffer, Phys. Rev. **106**, 162 (1957); Phys. Rev. **108**, 1175 (1957).
- [44] J. R. Schrieffer, *Theory of Superconductivity*, Revised Printing, Westview Press, USA (1999).
- [45] A. J. Leggett and S. Zhang, in W. Zwerger Ed, *The BCS-BEC Crossover and the Unitary Fermi Gas*, Springer-Verlag, Berlin, Heidelberg (2012).
- [46] A. J. Leggett, *Quantum Liquids*, Oxford University Press, Oxford (2012).
- [47] R. P. Feynman, in C. J. Gorter Ed., *Progress in Low Temperature Physics*, Vol. I, Interscience Publisher Inc., New York (1955).
- [48] N. N. Bogoliubov, Nuovo Cim. **6**, 794 (1958).
- [49] N. N. Bogoliubov, V. V. Tohmachev, and D. V. Shirkov, *A New Method in the Theory of Superconductivity*, Consultants Bureau, New York (1959).
- [50] R. P. Feynman and M. Cohen, Phys. Rev. **102**, 1189 (1956).
- [51] M. Cohen and R. P. Feynman, Phys. Rev. **107**, 13 (1957).
- [52] D. Pines and P. Nozieres, *Theory of Quantum Liquids*, Vol. II, Perseus Book, Cambridge, Massachusetts (1994).
- [53] J. M. Kosterlitz, J. Phys. C **7**, 1046 (1974).
- [54] V. Ambegaokar, B. I. Halperin, D. R. Nelson, and E. D. Siggia, Phys. Rev. Lett. **40**, 783 (1978).

- [55] V. Ambegaokar, B. i. Halperin, D. R. Nelson, and E. D. Siggia, Phys. Rev. B **21**, 1806 (1980).
- [56] B. I. Halperin and D. R. Nelson, J. Low Temp. Phys. **36**, 599 (1979).
- [57] L. D. Landau and E. M. Lifschitz, *Quantum Mechanics*, Pergamon Press, Oxford (1977).
- [58] A. Junod, M. Roulin, B. Revaz, A. Erb, and E. Walker, in *The Gap Symmetry and Fluctuations in High- $T_c$  Superconductors*, Edited by J. Bok, G. Deutscher, D. Pavuna, and S. A. Wolf, Plenum Press, New York (1998).
- [59] R. A. Fisher, J. E. Gordon, and N. E. Phillips, in Ref. [5].
- [60] M. K. Wu, *et al.*, Phys. Rev. Lett. **58**, 908 (1987).
- [61] J. Bardeen, Nuovo Cim. **5**, 1766 (1957).
- [62] P. W. Anderson, Phys. Rev. **112**, 1900 (1958).
- [63] G. Rickayzen, Phys. Rev. **115**, 795 (1959).
- [64] T. Takagi, *et al.*, Phys. Rev. B **40**, 2254 (1989).
- [65] J. B. Torrance, *et al.*, Phys. Rev. B **40**, 8872 (1989).
- [66] M. R. Presland, *et al.*, Physica C **176**, 95 (1991).
- [67] D. M. Broun, *et al.*, Phys. Rev. Lett. **99**, 237003-1 (2007).
- [68] F. James and M. Roos, Comput. Phys. Commun. **10**, 343 (1975).
- [69] W. N. Hardy, *et al.*, Phys. Rev. Lett. **70**, 3999 (1993).
- [70] W. N. Hardy, S. Kamal, D. A. Bonn, in *The Gap Symmetry and Fluctuations in High- $T_c$  Superconductors*, Edited by J. Bok, G. Deutscher, D. Pavuna, and S. A. Wolf, Plenum Press, New York (1998).
- [71] D. M. Broun, *et al.*, Phys. Rev. B **56**, R11443 (1997).
- [72] S.-F. Lee, *et al.*, Phys. Rev. Lett. **77**, 735 (1996).
- [73] G. Blatter, M. V. Feigel'man, V. B. Geshkenbein, A. I. Larkin, and V. M. Vinokur, Rev. Mod. Phys. **66**, 1125 (1994).
- [74] V. V. Schmidt, *The Physics of Superconductors*, Springer-Verlag, Berlin, Heidelberg (1997).
- [75] L. D. Landau and E. M. Lifschitz, *Electrodynamics of Continuous Media*, Pergamon Press, Oxford (1984).
- [76] L. Li, *et al.*, Nature Physics **3**, 311 (2007).
- [77] Y. Wang, L. Li, and N. P. Ong, Phys. Rev. B **73**, 024510 (2006).

- [78] G. Grissonnanche, *et al.*, Nature Commun. **5**, 3280 (2014).
- [79] D. Hang, *et al.*, New J. Phys. **12**, 105006 (2010).
- [80] F. Coneri, *et al.*, Phys. Rev. B **81**, 104507 (2010).
- [81] G. Drachuck, *et al.*, Nature Commun. **5**, 3390 (2014).
- [82] R. Liang, P. Dosanjh, D. A. Bonn, W. N. Hardy, and A. J. Berlinsky, Phys. Rev. B **50**, 4212 (1994).
- [83] R. Liang, D. A. Bonn, W. N. Hardy, and D. Broun, Phys. Rev. Lett. **94**, 117001 (2005).
- [84] Y. J. Uemura, *et al.*, Phys. Rev. Lett. **62**, 2317 (1989).
- [85] J. Corson, *et al.*, Nature **398**, 221 (1999).
- [86] G. Grissonnanche, *et al.*, Phys. Rev. B **93**, 064513 (2016).
- [87] M. Tinkham, *Introduction to Superconductivity*, Second Edition, McGraw-Hill Inc., New York (1996).
- [88] J.-F. Fagnard, *et al.*, Supercond. Sci. Technol. **23**, 095012 (2010).
- [89] M. Naamneh, J. C. Campuzano, and A. Konigel, Phys. Rev. B **90**, 224501 (2014).
- [90] D. W. Lynch and C. G. Olson, *Photoemission Studies of High-Temperature Superconductors*, Cambridge University Press, Cambridge, UK (1999).
- [91] A. Damascelli, Z. Hussain and Z. X. Shen, Rev. Mod. Phys. **75**, 473 (2003).
- [92] J. C. Campuzano, M. R. Norman, and M. Randeria, in K. H. Bennemann and J. B. Ketterson, Eds., *The Physics of Superconductors*, Vol. II, Springer-Verlag, Berlin, Heidelberg (2004).
- [93] S. E. Sebastian, N. Harrison, and G. G. Lonzarich, Trans. R. Soc. A **369**, 1687 (2011).
- [94] S. E. Sebastian, N. Harrison and G. G. Lonzarich, Rep. Prog. Phys. **75**, 102501 (2012).
- [95] B. Vignolle, D. Vignolles, M.-H. Julien, and C. Proust, Compt. Rend. Phys. **14**, 39 (2013).
- [96] S. E. Sebastian and C. Proust, Annu. Rev. Condens. Matter Phys. **6**, 411 (2015).
- [97] J. M. Luttinger, Phys. Rev. **119**, 1153 (1960).
- [98] L. Onsager, Phil. Mag. **43**, 1006 (1952).
- [99] I. M. Lifshitz and A. M. Kosevich, Sov. Phys. JETP **2**, 636 (1956).
- [100] A. A. Abrikosov, *Introduction to Theory of Normal Metal*, Academic Press, New York and London (1972).

- [101] N. W. Ashcroft and N. D. Mermin, *Solid State Physics*, Harcourt College Publishers, New York (1976).
- [102] D. Shoenberg, *Magnetic Oscillations in Metals*, Cambridge University Press, Cambridge (1984).
- [103] S. Sakai, *et al.*, Phys. Rev. Lett. **111**, 107001 (2013).
- [104] K. Tanaka, *et al.*, Science **314**, 1910 (2006).
- [105] R.-H. He, *et al.*, Nature Physics **5**, 119 (2009).
- [106] A. Pushp, *et al.*, Science **324**, 1689 (2009).
- [107] T. Yoshida, *et al.*, Phys. Rev. Lett. **103**, 037004 (2009).
- [108] M. Hashimoto, *et al.*, Nature Physics **6**, 414 (2010).
- [109] T. J. Reber, *et al.*, Nature Physics **8**, 606 (2012).
- [110] T. Yoshida, *et al.*, arXiv:1208.2903 (2012).
- [111] M. Hashimoto, *et al.*, Phys. Rev. B **86**, 094504 (2012).
- [112] M. Hashimoto, I. M. Vishik, R.-H. He, T. P. Devereaux, and Z.-X. Shen, Nature Physics **10**, 483 (2014).
- [113] M. Hashimoto, *et al.*, Nature Mater. **14**, 37 (2015).
- [114] E. M. Lifschitz and L. P. Pitaevskii, *Statistical Physics, Theory of the Condensed State*, Pergamon Press, Oxford (1980).
- [115] I. M. Vishik, *et al.*, Phys. Rev. Lett. **104**, 207002 (2010).
- [116] V. M. Svistunov, V. Yu. Tarenkov, A. I. Dyachenko, and E. Hatta, JETP Letters **71**, 289 (2000).
- [117] Ø. Fischer, H. Kugler, I. Maggio-Aprile and C. Berthod, Rev. Mod. Phys. **79**, 353 (2007).
- [118] G. Deutscher, Rev. Mod. Phys. **77**, 109 (2005).
- [119] W. S. Lee, *et al.*, Nature **450**, 81 (2007).
- [120] I. M. Vishik, *et al.*, New Journal of Physics **12**, 105008 (2010).
- [121] I.S. Gradshteyn and I.M. Ryzshik, Table of Integrals, Series and Products, 1980 (New York, Academic).
- [122] G. E. Volovik, JETP Lett. **58**, 457 (1993).
- [123] K. A. Moler, *et al.*, Phys. Rev. Lett. **73**, 2744 (1994).
- [124] K. A. Moler, *et al.*, Phys. Rev. B **55**, 3954 (1997).

- [125] B. Revaz, *et al.*, Phys. Rev. Lett. **80**, 3364 (1998).
- [126] D. A. Wright, *et al.*, Phys. Rev. Lett. **82**, 1550 (1999).
- [127] Y. Wang, B. Revaz, A. Erb, and A. Junod, Phys. Rev. B **63**, 094508 (2001).
- [128] S. H. Simon and P. A. Lee, Phys. Rev. Lett. **78**, 1548 (1997).
- [129] S. C. Riggs *et al.*, Nature Physics **7**, 332 (2011).
- [130] J. B. Kemper, *et al.*, Nature Physics **12**, 47 (2016).
- [131] R. Comin and A. Damascelli, Annu. Rev. Cond. Matter Phys. **7**, 369 (2016).
- [132] T. Wu, *et al.*, Nature **477**, 191 (2011).
- [133] A. M. Mounce, *et al.*, Phys. Rev. Lett **106**, 057003 (2011).
- [134] G. Ghiringhelli, *et al.*, Science **337**, 821 (2012).
- [135] J. Chang, *et al.*, Nature Physics **8**, 871 (2012).
- [136] A. J. Achkar, *et al.*, Phys. Rev. Lett. **109**, 167001 (2012).
- [137] T. Wu, *et al.*, Nature Commun. **4**, 2113 (2013).
- [138] D. LeBoeuf, *et al.*, Nature Physics **9**, 79 (2013).
- [139] S. Blanco Canosa, *et al.*, Phys. Rev. Lett. **110**, 187001 (2013).
- [140] T. P. Croft, C. Lester, M. S. Senn, A. Bombardi, and S. M. Hayden, Phys. Rev. B **89**, 224513 (2014).
- [141] S. Blanco Canosa, *et al.*, Phys. Rev. B **90**, 054513 (2014).
- [142] M. Hücker, *et al.*, Phys. Rev. B **90**, 054514 (2014).
- [143] K. Fujita, *et al.*, Proc. Natl. Acad. Sci. **111**, E3026 (2014).
- [144] M. Först *et al.*, Phys. Rev. B **90**, 184514 (2014).
- [145] W. Tabis, *et al.*, Nature Commun. **5**, 5875 (2014).
- [146] R. Comin, *et al.*, Science **343**, 390 (2014).
- [147] E. H. da Silva Neto, *et al.*, Science **343**, 393 (2014).
- [148] R. Comin, *et al.*, Nature Mater. **14**, 796 (2015).
- [149] T. Wu, *et al.*, Nature Commun. **6**, 1 (2015).
- [150] S. Gerber, *et al.*, Science **350**, 949 (2015).
- [151] E. M. Forgan, *et al.*, arXiv:1504.01585 (2015).
- [152] M. Hamidian, *et al.*, Nature Physics **12**, 150 (2016).



- [153] H. Fröhlich, Proc. Roy. Soc. London Ser. **A223**, 296 (1954).
- [154] R. E. Peierls, *Quantum Theory of Solids*, Oxford University Press, New York (1955).
- [155] G. Grüner, Rev. Mod. Phys. **60**, 1129 (1988).
- [156] G. Grüner, *Density Waves In Solids*, Addison-Wesley Publishing Company (1994).
- [157] W. Kohn, Phys. Rev. Lett. **2**, 393 (1959).
- [158] D. Reznik, Adv. Condens. Matter Phys. 2010, 523549 (2010).
- [159] D. Pines and P. Nozieres, *Theory of Quantum Liquids*, Vol. I, Perseus Book, Cambridge, Massachusetts (1994).
- [160] G. F. Giuliani and G. Vignale, *Quantum Theory of the Electron Liquid*, Cambridge University Press, New York, USA (2005).
- [161] M. J. Rice and S. Strässler, Solid State Commun. **13**, 125 (1973).
- [162] N. N. Bogoliubov, Nuovo Cim. **7**, 794 (1958).
- [163] J. G. Valatin, Nuovo Cim. **7**, 843 (1958).
- [164] C. G. Kuper, Proc. R. soc. A **227**, 214 (1955).
- [165] J. B. Nielsen and K. Carneiro, Solid State Commun. **33**, 1097 (1980).
- [166] R. Liang, D. A. Bonn, and W. N. Hardy, Phys. Rev. B **73**, 180505(R) (2006).
- [167] A. Shekhter, *et al*, Nature **498**, 75 (2013).
- [168] K. Maki and T. Tsuneto, Prog. Theor. Phys. **31**, 945 (1964).
- [169] W. D. Dieterich and P. Fulde, Z. Phys. **265**, 239 (1973).
- [170] T. Tiedje, J. F. Carolan, and A. J. Berlinsky, Can. J. Phys. **53**, 1593 (1975).
- [171] J. E. Hoffman, *et al.*, Science **295**, 467 (2002).
- [172] J. E. Graebner and M. Robbins, Phys. Rev. Lett. **36**, 422 (1976).
- [173] R. M. Fleming and R. V. Coleman, Phys. Rev. Lett. **36**, 1555 (1976).
- [174] J. A. Wilson, Adv. Phys. **24**, 117 (1975).
- [175] K. Rossnagel, J. Phys.: Condens. Matter **23**, 213001 (2011).
- [176] P. Schlottmann and L. M. Falicov, Phys. Rev. Lett. **38**, 855 (1977).
- [177] L. D. Landau and E. M. Lifschitz, *Quantum Mechanics*, 3rd Ed., Pergamon Press, Oxford (1991).
- [178] R. B. Dingle, Proc. R. Soc. A **211**, 500 (1952); Proc. R. Soc. A **211**, 517 (1952); Proc. R. Soc. A **212**, 38 (1952); Proc. R. Soc. A **212**, 47 (1952); Proc. R. Soc. A **216**, 118 (1953); Proc. R. Soc. A **219**, 463 (1953).

- [179] B. J. Ramshaw, *et al.*, Science **348**, 317 (2015).
- [180] K. Yamaji, J. Phys. Soc. Jpn **58**, 1520 (1989).
- [181] E. Suchitra, *et al.*, Proc. Natl. Acad. Sci. **107**, 6175 (2010).
- [182] D. LeBoeuf, *et al.*, Phys. Rev. B **83**, 054506 (2011).
- [183] S. -M. Baek, *et al.*, Phys. Rev. B **86**, 220504 (2012).
- [184] Y. Peng, *et al.*, Nature Commun. **4**, 2459 (2013).
- [185] S. Benhabib, *et al.*, Phys. Rev. Lett. **114**, 147001 (2015).
- [186] S. Badoux, *et al.*, Nature **531**, 210 (2016).
- [187] I. M. Lifshitz, Sov. Phys. J. Exp. Theor. Phys. **11**, 1130 (1959).
- [188] S. Sachdev, *Quantum Phase Transitions*, Cambridge University Press, Cambridge, UK (2011).
- [189] L. P. Gor'kov, Phys. Rev. B **88**, 041104 (2013).
- [190] S. I. Mirzali, *et al.*, Proc. Natl. Acad. Sci. **110**, 5774 (2013).
- [191] N. Barisic, *et al.*, Proc. Natl. Acad. Sci. **110**, 12235 (2013).
- [192] E. Gull and A. J. Millis, Nature Physics **11**, 808 (2015).
- [193] P. W. Anderson and P. Morel, Phys. Rev. **123**, 1911 (1961).
- [194] H. Won and K. Maki, Phys. Rev. B **49**, 1397 (1994).